Gerben Boer

Band 430

Polarization Interferometers using Liquid Crystal as Birefringent Elements

UFO Atelier für Gestaltung & Verlag

Université de Neuchâtel
Institut de Microtechnique

Polarization Interferometers using Liquid Crystal as Birefringent Elements

Thèse

Présentée à la faculté des sciences
Pour obtenir le grade de docteur ès sciences
par

Gerben Boer

Neuchâtel, juin 2003

UFO Dissertation Band 430

Die Deutsche Bibliothek – CIP-Einheitsaufnahme
Ein Titeldatensatz für diese Publikation ist bei
Der Deutschen Bibliothek erhältlich.

Dissertetion der Universität Neuchâtel
Datum der mündlichen Prüfung: 23.05.2003
Referenten: Prof. Dr. R. Dändliker
Prof. Dr. P. Seitz
Dr. J. Grupp
Prof. D. J. Broer

UFO Atelier für Gestaltung & Verlag GbR · D-78476 Allensbach
Internet: www.ufo-verlag.de

ISBN 3-935511-31-0

IMPRIMATUR POUR LA THESE

Polarization interferometers using liquid crystal as birefringent elements

de M. Gerben BOER

UNIVERSITE DE NEUCHATEL

FACULTE DES SCIENCES

Le Faculté des sciences de l'Université de Neuchâtel, sur le rapport des membres du jury

MM. R. Dändliker (directeur de thèse), P. Seitz, J. Grupp (Marin CH) et D.J. Broer (Eindhoven)

autorise l'impression de la présente thèse.

Neuchâtel, le 28 mai 2003

Le doyen:

François Zwahlen

Abstract

Polarization optics often uses expensive birefringent elements made of inorganic crystals. In recent years new birefringent materials such as polymer liquid crystals were developed. Replacing the inorganic crystals by these new types of liquid crystals would enable the fabrication of more affordable optical systems. This thesis presents the design and realization of several interferometric systems using birefringent elements made of liquid crystal (LC).

The main application that has been treated in this thesis is the realization of a hand-held Fourier transform spectrometer based on a modified LC Wollaston prism. For the design of the optical system we developed original polarization ray-trace models that are able to deal with complex birefringent structures such as twisted nematic LC. With these new design tools we were able to create compact configurations having high acceptance angles. We made important progress not only in the design but also in the fabrication of the LC elements. Since the conventional LCs are in the liquid phase and are therefore not temperature and shock resistant, we developed a completely new fabrication process based on liquid crystal polymers. With the help of these new materials, we were able to realize solid birefringent elements (up to 0.6mm thick) with good optical quality. It has been shown that the polymer elements are 50 times less temperature dependent than the elements made with the conventional LC. We have also investigated different alignment technologies and have shown that complex LC alignment pattern can be obtained by using high magnetic fields or photo alignment layers. By using these new designs and the polymer technology we realised and characterized a hand held spectrometer prototype specialized for colorimetry (low resolution), including LED illumination, background correction methods and an acquisition and data processing program. The advantages and limitations of the system are discussed.

We used the developed LC polymer technology to fabricate two other optical systems: the first one is a double-focus polarization interferometer based on a birefringent LC lens for surface topology measurements. We were able to perform first measurements and we have shown the aberrations and limitations of the system. The second application is a shearing interferometer for differential interference contrast microscopy that we installed in a conventional polarization microscope. We obtained good quality representations of the observed phase objects, which indicates that the expensive calcite or quartz elements used for such devices can throughout be replaced by LC polymer elements.

Contents

Chapter I

Introduction to polarization interferometry

This chapter gives an introduction to some basic concepts in the field of polarization interferometry and optics in birefringent media. The first section gives a brief overview of polarization interferometry. The second section explains how light propagates through anisotropic media and section three explains the interference mechanisms with polarized light.

1.1 Introduction

An interferometer is a device that divides a light beam into two (or more) beams, which follow different optical paths before being recombined to cause interference. In the particular case of a polarization interferometer, the entering light beam is divided by a polarization-division device into two beams having orthogonal polarizations. The first polarization interferometer was constructed by Jamin in 1868 [1]. The polarization interferometers can be classified in two categories: Interferometers with a small beam splitting angles (collinear) and systems with large splitting angles (non collinear). In the first category, the splitting angle between both beams is small and the optical phase or retardation shift is mainly created by the birefringence of the medium that is traversed by these beams. One of the main advantages of these interferometers is that the beams follow the same geometrical path. These interferometers are so-called "common-path interferometers". This makes them robust to vibrations and limits the geometrical extension of the device. In the second category with large beam splitting angles, the polarization-division is performed by a beamsplitter made of wire grids or by polarization beam splitter (PBS) cubes. These systems separate the incoming beam into two orthogonal polarized beams following two distinct geometrical paths. This kind of interferometers offer the possibility to induce larger phase shifts than the ones in the first category, but they cannot be considered as common-path anymore. Several examples of such systems, mainly used in astronomical spectroscopy, can be found in Polavarapu [2]. We will focus here on the first category, the common-path interferometers.
Polarization interferometers have many applications; most of them are presented in Françon and Mallick [3]. Widely used and most popular is the observation of phase objects in microscopy. Such an application will be presented in chapter 4. But there are also other applications such, as optical surface (or system) testing (chapter 4), spectrometry (chapter 3), optical thickness or retardation measurements [4] and many others.

1.2 Propagation of light through an anisotropic medium

1.2.1 Polarization

Polarization of light is determined by the temporal evolution of the direction of the electric field vector $\vec{E}(x,y,z,t)$. Since the propagation of light in an anisotropic media depends of his polarization state, we must define a convenient way to express it.

Generally, any light source can be decomposed in a sum of monochromatic electrical waves and each of these waves can be described as

$$\vec{E}(x,y,z,t) = \vec{A}(\vec{r})\cos(\vec{k}\cdot\vec{r} - \omega\cdot t + \delta), \tag{1.1}$$

where $\vec{A}(\vec{r})$ is the amplitude, $\vec{k}$ the propagation vector, $\vec{r}(x,y,z)$ the position, ω the angular frequency and δ a constant phase shift. By choosing Cartesian coordinates with the z-axis along the propagation direction of light, $\vec{E}$ can be decomposed into two orthogonal components $\vec{E}_x$ and $\vec{E}_y$ which are normal to the wave propagation

$$\vec{E}(\vec{r},t) = \vec{E}_x(z,t) + \vec{E}_y(z,t) = A_x(x,y)\vec{x}\cos(kz - \omega t + \delta_x) + A_y(x,y)\vec{y}\cos(kz - \omega t + \delta_y), \tag{1.2}$$

where $\vec{x}$, $\vec{y}$ are unity vectors and A_x, A_y are the amplitudes along the x and y axis. When considering a planar wave, the amplitudes are spatially constant and so independent of x and y.

Equation (1.2) can be rewritten in a complex representation, as:

$$\vec{E}(x,y,z,t) = \mathrm{Re}\left[A_x(x,y)\vec{x}e^{j(kz-\omega t+\delta_x)} + A_y(x,y)\vec{y}e^{j(kz-\omega t+\delta_x)} \right], \tag{1.3}$$

The polarization state is defined by the two amplitudes A_x, A_y and the phase difference $\delta = \delta_x - \delta_y$. The polarization can be described by the projection of the curve that is traced by the endpoint of the electric field on a plane perpendicular to the propagation direction. This curve is in general an ellipse. In this case the polarization is said to be elliptic. There are also some particular cases where the curve describes a circle (circular polarization) or a straight line (linear polarization).

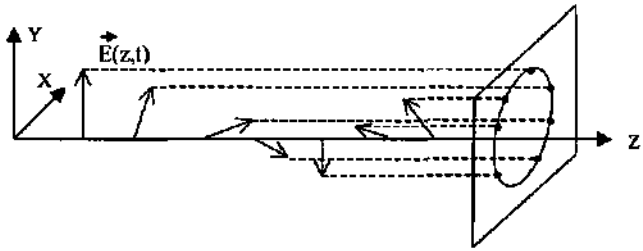

Fig. 1.1: Projection of the endpoints of the electric field vector E(z,t) on a plane perpendicular to the propagation direction. The projection points describe here an ellipse, which means that the planar wave is elliptically polarized.

Optical materials can change the state of polarization of incident polarized light. The primary mechanisms that change the state of polarization are:

1) Reflection: the reflected light from a dielectric interface has generally a different polarization state than the incident light especially for oblique incidence. The relation between the two polarization components for the reflected and transmitted light is given by the Fresnel equations [5].
2) Dichroism: Dichroic materials show anisotropic absorption properties. They absorb one of two polarization components of the incident light differently. The most common dichroic polarizers are thin sheet polarizers (essentially used in display applications and sunglasses). Nowadays, thin sheet polarizers show very high extinction and they are usually used to produce linearly polarized light in the visible region.
3) Birefringence: The state of polarization of the incident light can be modified by anisotropic materials because their optical properties (refractive index) change upon the direction of the electric field. Phase shifts between the polarization components can thus be induced in such materials. This subject is discussed in more detail in the next section.
4) Optical activity: Some materials, especially crystals and molecules in solution, can naturally rotate polarized light. The most common example is diluted water-sugar mixture. The rotation of polarization is used to quantify the amount of sugar, for instance in Wine. Other materials must be placed in a static magnetic field to show optical activity. This is known as the Faraday effect [6].
5) Scattering: Light is polarized by scattering when a material re-emits the incident light in a preferential direction [7]. Since molecules cannot radiate light perpendicular to the oscillation of its electrons (oscillating dipole). The re-emitted light will be partially polarized in the direction perpendicular to the incident light.

1.2.2 Anisotropic media

In anisotropic materials, the macroscopic optical properties are not the same in all directions. In such materials the atoms or molecules may be arranged in a certain order with symmetry. In addition binding forces on the electrons in molecules might be anisotropic. So, the oscillation characteristics of the electrons in such materials that

are exited by incident electrical fields will depend on the direction of this field. The anisotropy of the oscillation characteristics will induce an anisotropy in the dielectrical properties, which are expressed by the permitivity of the material.
The electric displacement vector $\vec{D}$ in Maxwell's equations is introduced to describe macroscopically the effect of the electrical field $\vec{E}$ on matter. The relation between $\vec{E}$ and $\vec{D}$ is defined as:

$$\vec{D} = \varepsilon \vec{E}\,, \tag{1.4}$$

where ε is the permitivity tensor (3x3). Since the ε tensor is symmetric, it can be transformed into the diagonal form

$$\varepsilon = \begin{pmatrix} \varepsilon_1 & 0 & 0 \\ 0 & \varepsilon_2 & 0 \\ 0 & 0 & \varepsilon_3 \end{pmatrix} \tag{1.5}$$

by judicious choice of the coordinate system (eigenvectors of the matrix).
In this particular case the coordinate axes x,y,z are parallel to the principal axis of the crystal. A vector $\vec{E}$ parallel to one of these principal axes will generate a vector $\vec{D}$ that is also parallel to this axis. The principal refractive indices n_i corresponding to ε_1, ε_2 and ε_3 are given by

$$n_i^2 = \varepsilon_i / \varepsilon_0\,, \tag{1.6}$$

where ε_0 is the permittivity of free space. Here, we can distinguish three different cases:

1) All the three indices are equal. In this case the material is isotropic.
2) Two of the principal indices are equal. In this case the material is called uniaxial. One distinguishes two different indices, the ordinary index $n_o = n_1 = n_2$ and the extraordinary index $n_e = n_3$.
3) All the three indices are different and the material is said to be biaxial.

Since we will mainly encounter uniaxial optical systems, as represented by nematic liquid crystals, we will treat this particular case in more detail.
The symmetry of uniaxial crystals has only one axes of rotational symmetry that is called the optical axes. When the crystal is rotated around this axis, its optical properties stay unaltered. The refractive indices of the normal modes are dependent of the propagation direction of the light. This dependency can be represented in an ellipsoid that carries all the information about the matrix presented in Eq. (1.5). This ellipsoid is called the index ellipsoid and its axes have half-lengths n_i given by Eq. (1.6). In Fig. 1.2 we represented the case of an uniaxial crystal, here the length of first two axes are equal to n_o and the length of third axis is equal to n_e.

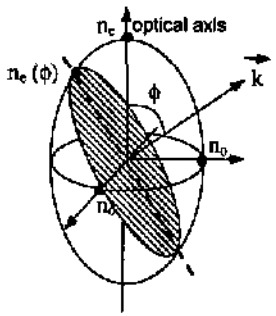

Fig. 1.2: Index ellipsoid of an uniaxial crystal with positive birefringence. The ellipsoid has a rotational symmetry with respect to the optical axis. The Indice $n_e(\phi)$ is given here by the half-length of the major axis.

The index ellipse (hatched area) is given by the intersection between the ellipsoid and the plane that passes through the origin and that is perpendicular to $\vec{k}$. The half-lengths of the minor and major axes of this ellipse gives n_o and $n_e(\phi)$, respectively, with [8]

$$\frac{1}{n_e(\phi)^2} = \frac{\cos^2\phi}{n_o^2} + \frac{\sin^2\phi}{n_e^2}. \tag{1.7}$$

We see here that $n_e(\phi)$ can vary from n_o ($\phi = 0°$) to n_e ($\phi = 90°$). Figure 1.3 illustrates the double refraction (one incident ray and two refracted rays) of a non-polarized plane wave that arrives at an isotropic-anisotropic boundary. A ray splitting in two polarization components occurs due to two refractive indices associate with the anisotropic medium. Applying Snell's law for both polarizations separately, we obtain for the ordinary refraction angle

$$n\sin\phi = n_o \sin\phi_o, \tag{1.8}$$

and for the extraordinary refraction angle

$$n\sin\phi = n_e(\phi_e)\sin\phi_e, \tag{1.9}$$

where $n_e(\phi)$ is given by Eq. (1.7).

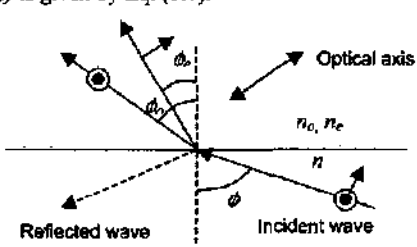

Fig.1.3: Double refraction at an isotropic-anisotropic interface. The incident wave is refracted into two waves: the ordinary and the extraordinary.

Double refraction is of course a interesting property for many optical applications. However, the fabrication of birefringent elements is laborious and expensive. The choice of material can be optimized in function of the wavelength, required birefringence and environmental conditions. The characteristics of the most commonly used natural-occurring materials which show birefringence are listed in Tab. 1.1 [9].

Name	Chemical formula	Characteristic	Spectral band	n_o, n_e	Birefringence (n_e-n_o)
Quartz	SiO_2	hard	0.2-2.6μm	1.544, 1.553	0.009
Calcite	$CaCO_3$	Soft	0.2-3 μm	1.49, 1.66	0.17
Rutile	TiO_2	large birefringence	0.6-5μm	2.6, 2.9	0.27

Tab. 1.1: The most commonly used inorganic uniaxial crystals.

One of the crystals mentioned above, calcite, is widely used in polarization optics because of the wide spectral range, the large birefringence and the availability in reasonably sized rhombs. Another important family of uniaxial materials are the nematic liquid crystals. These materials will be discussed in chapter 2.

1.2.3 Jones formalism

An elegant and convenient way to express a polarization state mathematically is the Jones vector [10]. The Jones vector

$$\bar{J} = \begin{pmatrix} A_x e^{j\delta_x} \\ A_y e^{j\delta_y} \end{pmatrix}, \tag{1.10}$$

is derived from the complex notation that is shown in Eq. (1.3). The two orthogonal components E_x and E_y are recast as a column vector and the temporal dependency is not taken into account. In the particular case where $A_x = A_y$ and $\delta_x - \delta_y = \pm\pi/2 + m\pi$ ($m = 0, \pm1, \pm2, \ldots$), the polarization is circular. The sign of the phase shift give the rotation direction of the electrical field vector. The light is linearly polarized when $\delta_x - \delta_y = \pm m\pi$.
The Jones formalism permits to calculate polarization modifications of the light by multiplying the input Jones vector with appropriate Jones matrices. There are mainly three types of Jones matrices: the linear polarizer matrix

$$L = \begin{bmatrix} 1 & 0 \\ 0 & 0 \end{bmatrix}, \tag{1.11}$$

the wave retarder matrix T

$$T = \begin{bmatrix} 1 & 0 \\ 0 & e^{-j\Gamma} \end{bmatrix}, \tag{1.12}$$

and the polarization rotator matrix

$$R(\theta)=\begin{bmatrix}\cos\theta & -\sin\theta\\ \sin\theta & \cos\theta\end{bmatrix}, \tag{1.13}$$

where Γ is the induced phase shift between the two components and θ is the rotation angle of the polarization. Linear systems that alter the polarization can be decomposed in a set of retarders, rotators and linear polarizers. Depending of the orientation of these elements relatively to the x-y coordinate system of the Jones vector, we must apply a coordinate transformation to express the Jones vector in the new coordinate x'-y' of the element. If x' makes an angle θ with the x direction then the Jones vector in the new coordinates is given by

$$J' = R(\theta)J\,. \tag{1.14}$$

After been transformed by a Jones matrix, J' can then be transformed back in the x-y coordinates by applying the inverse rotation matrix $R^{-1}(\theta) = R(-\theta)$. $R(\theta)$ and $R^{-1}(\theta)$ can be directly combined with L or T. For example, a retardation plate rotated by θ in the x-y plane gives

$$T_\theta = R(-\theta)TR(\theta)\,. \tag{1.15}$$

The resulting matrix that describes the complete system is given by the multiplication of the corresponding T, R and L matrices:

$$\vec{J}_{out} = M_n \ldots M_2 M_1 \cdot \vec{J}_{in}, \tag{1.16}$$

where M_i is a T, R or L matrix, $\vec{J}_{out}$ is the output Jones vector and $\vec{J}_{in}$ is the Jones input vector. Note that the matrices have to be multiplied in the correct order (M_1 is the first element) because they are not commutative.

1.2.4 Extended Jones formalism

The conventional Jones matrix method is very powerful for studying the transmission characteristics of birefringent systems. However, this method is limited to normally incident light. Fresnel reflection and refraction for off-axis light at an isotropic-birefringent interface are not taken into account. The extended Jones matrix method [11], is a technique that can trest off-axis light more accurately than the conventional Jones matrix method. It takes into account Fresnel refraction and single reflections at the interface. Still, it neglects multiple reflections between plane interfaces (which is treated by the 4x4 Berremann matrix method [12]). But in most practical applications these effects are relatively small and can be neglected.
In the extended Jones matrix method, the light propagates through a stratified medium, consisting of a stack of N birefringent layers. N is assumed to be sufficiently large so that the optical axis can be regarded as constant within the layer (or plate). For simplification, we also consider that the birefringence is small $|n_e - n_o| << n_e, n_o$, which is the case for most uniaxial crystals. By assuming small birefringence,

calculations are greatly simplified because we can consider that the refraction angles ϕ_o of the ordinary ray and ϕ_e of the extraordinary ray (Fig. 1.3) are almost equal. So, the wave vectors $\vec{k}_o$ and $\vec{k}_e$ of the two rays can be considered almost equal. The local polarization vectors of the ordinary ray $\vec{o}_i$ and the extraordinary ray $\vec{e}_i$ can be given approximately by:

$$\vec{o}_i = \frac{\vec{k}_o \times \vec{n}_i}{\left|\vec{k}_o \times \vec{n}_i\right|}, \tag{1.17}$$

$$\vec{e}_i = \frac{\vec{o} \times \vec{k}_o}{\left|\vec{o} \times \vec{k}_o\right|}, \tag{1.18}$$

where $\vec{n}_i$ is the local director of the optical axis. So the polarizations $\vec{o}_i$ and $\vec{e}_i$ are mutually orthogonal and propagate in the same direction given by $\vec{k}_o (\approx \vec{k}_e)$.

In order to treat mathematically only an isotropic-uniaxial boundaries (which is easier than treating uniaxial-uniaxial boundaries), we introduce an imaginary isotropic medium (with index n_o) between the birefringent layers with a thickness that tends to zero.

When propagating through the stack of birefringent and isotropic layers, we may distinguish four different cases:

a) Isotropic layer to first birefringent layer described by the input dynamic matrix D_{in}.
b) Last birefringent layer to isotropic layer described by the output dynamic matrix D_{out}.
c) Propagation inside the birefringent layers described by the propagation matrix P_i.
d) Transition from layer i to layer $i+1$ described by the dynamic matrix $D_{i,i+1}$.

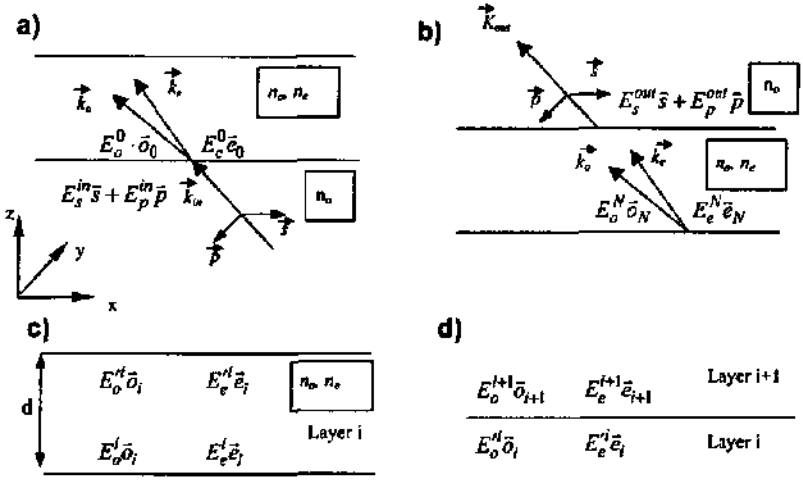

Fig. 1.4: Schematic representation (a) of the input dynamic matrix, (b) the output dynamic matrix, (c) propagation matrix, (d) dynamic matrix between two layers.

As depicted in Fig. 1.4a, the input dynamic matrix D_{in} projects the incoming polarization vectors onto the polarization vectors of the first layer (dependent of the optical axis) and multiplies them with the Fresnel input transmission coefficients t_s, t_p of the input polarisation components (s and p):

$$\begin{pmatrix} E_e^0 \\ E_o^0 \end{pmatrix} = D_{in} \cdot \begin{pmatrix} E_s^{in} \\ E_p^{in} \end{pmatrix} = \begin{pmatrix} \vec{s} \cdot \vec{e}_0 t_s & \vec{p} \cdot \vec{e}_0 t_p \\ \vec{s} \cdot \vec{o}_0 t_s & \vec{p} \cdot \vec{o}_0 t_p \end{pmatrix} \cdot \begin{pmatrix} E_s^{in} \\ E_p^{in} \end{pmatrix}, \tag{1.19}$$

The output dynamic matrix D_{out} (Fig. 1.4b) projects the polarization vectors of the last layer onto the output reference axes s and p and multiplies them with the Fresnel output transmission coefficients t'_s, t'_p:

$$\begin{pmatrix} E_s^{out} \\ E_p^{out} \end{pmatrix} = D_{out} \cdot \begin{pmatrix} E_s^N \\ E_p^N \end{pmatrix} = \begin{pmatrix} \vec{e}_N \cdot \vec{s} t'_s & \vec{e}_N \cdot \vec{p} \cdot t'_p \\ \vec{o}_N \cdot \vec{s} t'_s & \vec{o}_N \cdot \vec{p} t'_p \end{pmatrix} \cdot \begin{pmatrix} E_s^N \\ E_p^N \end{pmatrix}. \tag{1.20}$$

The propagation matrix (Fig. 1.4c) adds the phase shifts cumulated by the two polarization components when traversing a homogeneous uniaxial layer:

$$\begin{pmatrix} E_e^{ri} \\ E_o^{ri} \end{pmatrix} = P_i \cdot \begin{pmatrix} E_e^i \\ E_0^i \end{pmatrix} = \begin{pmatrix} e^{-jk_{ez}} & 0 \\ 0 & e^{-jk_{oz}} \end{pmatrix} \cdot \begin{pmatrix} E_e^i \\ E_0^i \end{pmatrix}. \tag{1.21}$$

The dynamic matrix (Fig. 1.4d) projects the polarization vectors of one layer onto the polarization vectors of the next layer (without transmission loss):

$$\begin{pmatrix} E_e^{i+1} \\ E_o^{i+1} \end{pmatrix} = D_{i,i+1} \cdot \begin{pmatrix} E_e^{i} \\ E_o^{i} \end{pmatrix} = \begin{pmatrix} \vec{e}_i \cdot \vec{e}_{i+1} & \vec{o}_i \cdot \vec{e}_{i+1} \\ \vec{e}_i \cdot \vec{o}_{i+1} & \vec{o}_i \cdot \vec{o}_{i+1} \end{pmatrix} \cdot \begin{pmatrix} E_e^{i} \\ E_o^{i} \end{pmatrix}. \tag{1.22}$$

If we want the transformation matrix M of the whole stack, we must multiply the matrixes of the different layers in the correct order :

$$M = D_{out} P_N D_{N-1,N} P_{N-1} D_{N-2,N-1} \cdots D_{1,2} P_1 D_{0,1} P_0 D_{in}. \tag{1.23}$$

One common application of this method is to calculate the angular dependency of twisted liquid crystal structures (TN cells or STN cells) used for displays. In this case each layer has an optical axis that is slightly rotated with respect to the next one. Examples of such calculations can be found in [13].

1.2.5 Stokes Vector

Natural light is said to be completely non-polarized. This means that the electric vector has no preferred oscillation direction over time. Mostly, light is partially polarized; this means that a significant part of the light is randomly polarized but the electric field shows a certain preferred direction on average.
The Jones formalism is only applicable to completely polarized light. Another formalism, which can deal with partially polarized light, are the Stokes vectors and the Müller matrixes [14]. In polarization interferometry the incoming light is always polarized and interference effects are essential. The Müller matrix formalism is thus not well suited for our subject. However, it may be interesting to briefly explain here the significance of the Stokes vector. The Stokes vector is defined as

$$\vec{S} = \begin{pmatrix} \langle A_x^2 + A_y^2 \rangle \\ \langle A_x^2 - A_y^2 \rangle \\ \langle 2 A_x A_y \cos\delta \rangle \\ \langle 2 A_x A_y \sin\delta \rangle \end{pmatrix}, \tag{1.24}$$

where A_x and A_y are the amplitudes of two polarization components and δ is the relative phase shift between these two components. These parameters are time dependent and the brackets denote averages performed over the detection time interval. S_0 represents the total intensity, S_1 represent the excess of parallel to perpendicular polarized light, S_2 the excess of +45° to -45° polarized light and S_3 the excess of right circularly to circularly polarized light. These parameters can be measured by using different circular and linear polarization filters.

1.3 Interference with polarized light

1.3.1 Introduction

The observed light at a certain time and a certain point in space may be given by the superposition given by several electric fields $\vec{E}_i$ originating from various sources. So we can write the electric field as

$$\vec{E} = \sum_i \vec{E}_i = \sum_i \vec{A}_i \cos(\vec{k}_i \cdot \vec{r} - \omega_i t + \delta_i). \tag{1.25}$$

To be able to observe interference phenomena, we need waves with similar frequencies and constant phase relations. For simplicity, we will consider here the superposition of two monochromatic plane waves

$$\vec{E} = \vec{E}_1 + \vec{E}_2 = \vec{A}_1 \cos(\vec{k} \cdot \vec{r} - \omega t) + \vec{A}_2 \cos(\vec{k} \cdot \vec{r} - \omega t + \delta), \tag{1.26}$$

with equal frequency and different directions at a certain point defined by $\vec{r}$. The intensity is then given by

$$I = \left\langle \vec{E}^2 \right\rangle_T = \left\langle A_1^2 \cos^2(\vec{k}_1 \cdot \vec{r} - \omega t) \right\rangle_T + \left\langle A_2^2 \cos^2(\vec{k}_2 \cdot \vec{r} - \omega t + \delta) \right\rangle_T$$
$$+2\left\langle \vec{A}_1 \cos(\vec{k}_1 \cdot \vec{r} - \omega t) \cdot \vec{A}_2 \cos(\vec{k}_2 \cdot \vec{r} - \omega t + \delta) \right\rangle_T \tag{1.27}$$

Using the fact that $\left\langle \cos^2(\vec{k} \cdot \vec{r} - \omega t + \delta) \right\rangle_T = 1/2$ and $\left\langle \cos(\vec{k}_1 \cdot \vec{r} - \omega t) \sin(\vec{k}_2 \cdot \vec{r} - \omega t) \right\rangle_T = 0$, we finally find

$$I = \frac{1}{2} A_1^2 + \frac{1}{2} A_2^2 + 2\vec{A}_1 \cdot \vec{A}_2 \cos((\vec{k}_1 - \vec{k}_2) \cdot \vec{r} - \delta). \tag{1.28}$$

The resulting intensity is the sum of two constant terms and a term that varies with the position $\vec{r}$ and the phase difference δ. This last term is called the interference term. If we consider now the particular case where the propagation vectors are both in the y-z plane and $\vec{A}_1$ and $\vec{A}_2$ are parallel, we can write

$$I = I_1 + I_2 + 2\sqrt{I_1 I_2} \cos(k \cdot \sin\theta \cdot y - \delta), \tag{1.29}$$

where I_1, I_2 are the intensities corresponding to the two optical fields. Fig. 1.5 shows the spatial intensity distribution of Eq. (1.29).

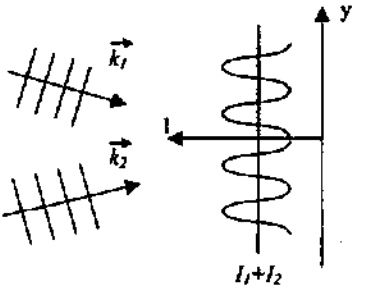

Fig 1.5: Sinusoidal interference pattern obtained with two coherent plane waves.

The contrast of the signal or the visibility V of the fringes is defined by the normalized difference between the maximum signal I_{max} and the minimum signal I_{min}

$$V = \frac{I_{max} - I_{min}}{I_{max} + I_{min}}. \tag{1.30}$$

The interference term will be maximal (for constant total intensity) if the intensities of both waves are equal ($I_1 = I_2$). The visibility (given by Eq. (1.30)) is in this case equal to 1.

In the particular case of a polarization interferometer as shown in Fig. 1.6, the interference pattern is produced by two mutually orthogonal electric fields $E_1 = E_x$ (parallel to the x-axis) and $E_2 = E_y$ (parallel to the y-axis) that follows different optical paths. As it will be explained further, to be able to see an interference phenomena E_x and E_y must have a defined phase relation (coherent), so practically they must emanate from a single source. Then the light has to be polarized with a polarizer to avoid averaging of all the polarization states at the output (which would make the interference pattern to disappear). The two polarization components of the polarized light will then accumulate a certain phase shift when traversing a birefringent object.

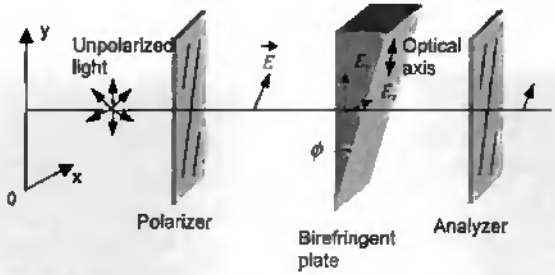

Fig 1.6:shema of a typical polarization interferometer based on a birefringent element.

The general expression for an interference pattern generated by a polarization interferometer is given by [Born and Wolf]:

$$I_{out} = I_0\left(\cos^2\chi - \sin 2\varphi \sin 2(\varphi-\chi)\sin^2\frac{\delta}{2}\right), \tag{1.31}$$

where φ is the angle of the first polarizer with respect to the x-axis, χ is the angle between the two polarizers, I_0 is the maximum intensity and δ is the spatially varying phase shift between the two polarization components. The interference contrast (or visibility) is maximized when $\chi = 0°$ and with a polarizer angle of $\varphi = 45°$ and Eq. (1.31) becomes then

$$I_{out} = I_0 \cos^2(\delta/2), \tag{1.32}$$

In the case of the interferometer of Fig. 1.6, the phase shift δ depends on the local thickness of the birefringent prism d, the wavelength λ and the two refractive indices n_1 and n_2 associated to the two polarization components and it is given by

$$\delta = \frac{2\pi}{\lambda}(n_2 - n_1)d, \tag{1.33}$$

In the case of the polarization interferometer of Fig. 1.6, the thickness d depends linearly on the y position of the ray and if the uniaxial plate is cut parallel to its optical axis. The phase shift relation of Eq. (1.33) becomes:

$$\delta = \frac{2\pi}{\lambda}(n_e - n_o)(D/2 + y\tan(\phi)), \tag{1.34}$$

where D is the maximal thickness of the prism and ϕ is the wedge angle. At the output of the birefringent prism, the polarization of the two beams have to be made to interfere with an analyzer set at 45°. When substituting Eq. (1.34) in Eq. (1.32), we finally obtain

$$I_{out}(y)=\frac{I_0}{2}(1+\cos(\delta))=\frac{I_0}{2}\left(1+\cos\left(\frac{2\pi}{\lambda}(n_e-n_o)(D/2+y\tan(\phi))\right)\right). \tag{1.35}$$

1.3.2 Temporal coherence

In general light sources are not coherent and the sum of all the electric fields at a certain point in space varies very rapidly in time (~10^{14} Hz). Practically this variation cannot be detected. Therefore, integrated over a certain period of time, the measured intensity I might be seen as statistically constant (assuming that the amplitude of different sources are also constant) and there will be no interference phenomena observed.
It is convenient to decouple here two types of coherence: the spatial coherence and the temporal coherence. The temporal coherence is expressed for a point source as the degree of correlation between electric waves observed with a time delay of τ. A quantitative measure of this correlation is given by the normalized autocorrelation function $\gamma(\tau)$. Considering that all the light has the same polarization state we can use the scalar representation. That is the case at the output of the interferometer shown in Fig. 1.6. so that $\gamma_{11}(\tau)$ is given by

$$\gamma_{11}(\tau)=\frac{\left\langle E_1(t)E_1^*(t+\tau)\right\rangle}{\sqrt{I_1}\sqrt{I_1}}. \tag{1.36}$$

$\gamma_{11}(\tau)$ have values between 0 and 1. $\gamma_{11}(\tau)$ is equal to one if the source is completely coherent (maximal correlation) and $\gamma_{11}(\tau)$ becomes zero when the source is completely incoherent (minimal correlation).
All natural (real) light sources have a limited temporal coherence. This means that $\gamma_{11}(\tau)$ decreases with increasing time intervals. The coherence time τ_c gives a quantitative measure of the decrease of $\gamma_{11}(\tau)$ and it can be defined as

$$\tau_c=\int_{-\infty}^{\infty}\left|\gamma_{11}(\tau)\right|^2 d\tau. \tag{1.37}$$

Sometimes τ_c is also defined as the time interval above which $\gamma_{11}(\tau)$ drops below a certain arbitrary value. Supposing that $\gamma_{11}(\tau)$ is varying more slowly over $\bar{r}$ than $\cos(\delta)$, Eq. (1.32) can be written for partially coherent light source as [15]

$$I_{out}(\bar{r},t)=I_0/2\left(1+\left|\gamma_{11}(\tau)\right|\cos(\delta(\bar{r},t)+\phi_{11})\right), \tag{1.38}$$

where ϕ_{11} is the phase of $\gamma_{11}(\tau)$. For the case of the interferometer described in Fig. 1.6, $\bar{r}$ and τ are related by Eq. (1.34) and $\tau=\delta\lambda/2\pi c$ (c = speed of light). For the same interferometer the local visibility of fringes of I_{out} is directly given by the autocorrelation function

$$V = \frac{I_{out}(\delta = 0) - I_{out}(\delta = \pi)}{I_{out}(\delta = 0) + I_{out}(\delta = \pi)} = \left|\gamma_{11}(\tau)\right|, \tag{1.39}$$

The complex degree of temporal coherence quantified by $\gamma(\tau)$ is related to the power spectral density of the light source $S(\nu)$ by an inverse Fourier transform

$$\gamma(\tau) = \frac{\int_0^\infty S(\nu)\exp(j2\pi\nu\tau)d\nu}{\int_0^\infty S(\nu)d\nu}. \tag{1.40}$$

This relation is known as the Wiener-Khinchin theorem [16]. The denominator is introduced for normalization and gives the total averaged intensity emitted by the light source. Light sources with a narrow spectral range have high temporal coherence (a large τ_c). In contrary, sources with a broad spectrum have a small temporal coherence (a small τ_c). Practical illustrations of this theorem will be given in chapter 3.

1.3.3 Spatial coherence

In order to decouple the spatial coherence from the temporal coherence, we will consider here that the effects of the limited temporal coherence (coherence time) of the source can be neglected compared to the effects produced by the limited spatial coherence (on the observed interference pattern). A spatial partial coherent source can be described as a collection of mutually incoherent point sources that are separated in space. From each of these point sources emits a spherical wave that is divided into the two arms of the interferometer (or two polarization components) and gives rise to an interference pattern. Ideally, if all the interference patterns (produced by the different point sources) are in phase (perfectly correlated) there is no reduction of the contrast. But in general the interference pattern produced by the different point sources are shifted to each other and the sum of these patterns will have a reduced visibility compared to the ideal case. The visibility of this interference pattern depends not only on the source but also on the plane (or surface) of observation. The plane where the visibility of the interference fringes is maximal (for a given source position and size) is called plane of localization.

Similarly to Eq. (1.36), the complex degree of spatial coherence μ_{12} is given by the normalized time-average of the product between the electric fields E_1 coming from the first arm (ordinary ray) of the interferometer and E_2 coming from second arm (extraordinary ray). E_1 and E_2 are sampled at the same time t and the same position of observation $\vec{r}(x', y', z')$:

$$\mu_{12}(\vec{r}) = \frac{\left\langle E_1(t,\vec{r})E_2^*(t,\vec{r})\right\rangle}{\sqrt{I_1}\sqrt{I_2}}. \tag{1.41}$$

E_1 and E_2 are the sums $E_1 = \sum_m E_{1m}$, $E_2 = \sum_m E_{2m}$ of all the contributions E_{km} coming from the point sources of the extended source. Hence,

$$\left\langle E_1(t,\vec{r})E_2^*(t,\vec{r})\right\rangle = \sum_m \left\langle E_{m1}E_{m2}\right\rangle + \sum_{m\neq n}\sum_n \left\langle E_{m1}E_{n2}\right\rangle. \tag{1.42}$$

But since E_{m1} and E_{n2} are statistically independent point sources, the average $\left\langle E_{m1}E_{n2}\right\rangle = 0$ when $m \neq n$. The product $\left\langle E_{m1}E_{m2}^*\right\rangle$ can be rewritten as

$$\left\langle E_{m1}E_{m2}^*\right\rangle = \left\langle A_{m1}(t)A_{m2}^*(t)\right\rangle \exp(-jk(L_{m1}-L_{m2})), \tag{1.43}$$

where Lm_1 and Lm_2 are the optical path lengths accumulated by the two beams. The intensity of a point source k placed at (x,y) is $\left\langle A_k(t)A_k^*(t)\right\rangle = I(x,y)dxdy$ and the total emitted intensity is I_{tot}. Considering the case where $I_1 = I_2$, introducing Eq. (1.42) and Eq. (1.43) in Eq. (1.41) and replacing the sum by the surface integral over the whole source S, we finally obtain

$$\mu_{12}(\vec{r}) = \frac{\iint_S I(x,y)\exp(-jk(L_1(\vec{r},x,y)-L_2(\vec{r},x,y)))dxdy}{I_{tot}}. \tag{1.44}$$

We note here that this expression is similar to the van Cittert-Zernike theorem [17] that gives the complex coherence degree between two points in a homogenous medium illuminated by an extended source. As already seen for the temporal coherence (Eq. (1.38)), the intensity $I_{out}(\vec{r})$ for a certain point of the observation plane at the output of the interferometric system is given by

$$I_{out} = I_0/2\left(1+\mathrm{Re}\left\{\mu_{12}(\vec{r})\right\}\cos(\delta(\vec{r}))\right) = \frac{I_0}{2}\left(1+\left|\mu_{12}(\vec{r})\right|\cos(\delta(\vec{r})+\phi_{12})\right), \tag{1.45}$$

where ϕ_{12} is the phase of μ_{12}. We assume here that the light is quasi monochromatic and that the modulation of $\cos(\delta)$ over $\vec{r}$ is slower than the modulation of μ_{12}. The local visibility of the fringes is given by the degree of the complex spatial coherence μ_{12}, as in Eq. (1.39).

1.3.4 Field of view

In interferometry, one is interested in maximizing the visibility of the fringes (as defined in Eq. (1.30)) in order to increase the signal to noise ratio (SNR). As seen previously, the visibility is essentially given by the complex degree of spatial coherence. That is given in Eq. (1.45) and considers the temporal coherence as a given parameter. So, the parameter that has to be optimized is the optical path difference (OPD) between the two arms of the interferometer given by $\Delta L(\vec{r},x,y) = L_1 - L_2$. Ideally, to get maximum visibility, the OPD should be constant

between every point of the source and a given point $\vec{r}'$ in the interference pattern. But practically this is rarely the case and there will be a certain variations of the OPD. The angular dependence of this variation for a polarization interferometers similar to that shown in Fig. 1.6 can be evaluated with a conoscopic method [19-20] in the polarizing microscope. As shown in Fig. 1.7, this method illuminates the interferometer with a coherent light source (with large aperture). The light is focused at the center of the system and the obtained interference pattern is analyzed in the far field. The central fringe of the interference pattern gives the angular range over which the DPD does not vary more than $\lambda/2$. This angular range gives the so-called field of view.

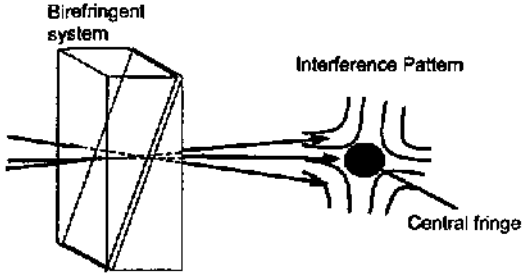

Fig. 1.7: Schematic representation of the conoscopic method that permits to analyze the angular dependency of the interferometric system.

This method is particularly interesting for analyzing polarization interferometers based on birefringent plates. In this case, the angular variation of the OPD may become important because of the angular dependency of the birefringence. A detailed study of such systems will be presented in chapter 3.

1.3.5 Localization of the fringes

As already mentioned in the paragraph dedicated to the spatial coherence, when illuminating the interferometer with a spatial incoherent source the visibility of fringes depends on the plane of observation. The plane where the visibility is maximal is called the plane of localization or the plane of maximal contrast. It can be shown [21, 22] that this plane is located at the intersection of the two rays that come from the two arms of the interferometer and that originated from the source point or ray S of the source. This is illustrated in Fig. 1.8 for a polarization interferometer where the two rays are the ordinary and the extraordinary rays O and E, respectively.

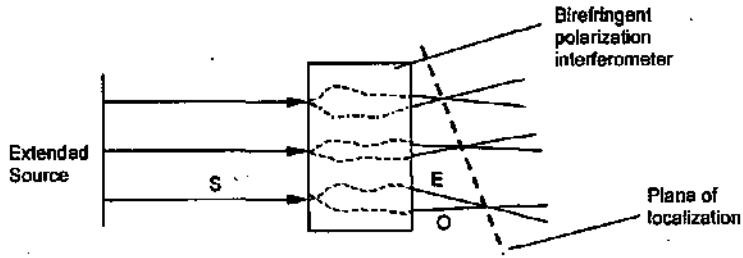

Fig. 1.8: Schematic representation of the plane of localization situated at the intersection of the ordinary and extraordinary ray

The plane of localization can be outside the interferometric system, as it is the case in Fig. 1.8, or inside. When the plane of localization is situated inside the system, the rays do not converge and optics is needed to image the fringes onto the detector.

1.4 References

[1] M.J Jamin, "Sur un réfracteur pour la lumière polarisée", *comptes rendus Acad. Sc.*, Paris, **67**, p. 814, 1868.

[2] P.L Polavarapu, *Principles and applications of polarization-division interferometry*. Wiley, New York, 1998.

[3] M. Françon and S.Mallick, *Polarization Intreferometers*, Wiley, New-York, 1971.

[4] M. Françon and S.Mallick, *Polarization Intreferometers*, Chap. 7. Wiley, New-York, 1971.

[5] M. Born and E. Wolf, *Principles of Optics*, fifth edition, pp.38-41. Pergamon Press, 1975.

[6] B.E.A Saleh, M. C. Teich, *Fundamentals of Photonics*, p. 225. Wiley-Interscience, 1991.

[7] E. Hecht, *Optics*, Addison Wesley (1998).

[8] B.E.A Saleh, M. C. Teich, *Fundamentals of Photonics*, p. 218. Wiley-Interscience, 1991.

[9] Hanbook of Chemistery and Physics, 79th edition. CRC Press, 1998-1999.

[10] R. Clark Jones, "A new calculus for the treatment of optical systems", *J. opt. Soc. Am*, **31**, 488-503, 1941.

[11] P. Yeh and C. Gu, *Optics of Liquid Crystal Displays*, p.306. Wiley Interscience, New York, 1999.

[12] D. W. Berreman, *J. opt. Soc. Am.* **62**, 502, 1972.

[13] F. H. Yu and H. S. Kwok, "Comparison of extended Jones matrices for twisted nematic liquid-crystal displays at oblique angles of incidence", *J. Opt. Soc. Am.* A **16**, p.2772, 1999.

[14] Christian Brosseau, *Fundamentals of Polarized Light: a statistical optics approach*, pp. 210-231. Wiley, New York, 1998.

[15] M. Born and E. Wolf, *Principles of Optics*, fifth edition, p.502. Pergamon Press, 1975.

[16] M. Born and E. Wolf, *Principles of Optics*, fifth edition, p.504. Pergamon Press, 1975).

[17] M. Born and E. Wolf, *Principles of Optics*, fifth edition, p.508. Pergamon Press, 1975.

[19] A. F. Hallimond, *The polarizing Microscope*. Vickers Instruments, York, UK, 1970.

[20] F. Rinne and M. Berek, *Anleitung zur allgemeinen und Polarizationsmikroscopie der Festkörper im Durlicht*. Schweizer-bart'sche Verlagsbuchhandlung, Stuttgart, 1973.

[21] P. Hariharan, *Optical interferometry*, p.18, Academic Press, Sydney, 1985.

[22] J.C Wyant, "Fringe localization", *Appl. Optics*, **17**, 1853, 1978.

Chapter 2

Passive liquid crystal elements

Since the early 1970's, liquid crystals (LC) are widely used especially for applications in the field of flat panel displays. The majority of these applications use the electro-optical properties of LC (reorientation in the electric field). Very few investigations have been done so far to use LC as static birefringent elements for optical applications. In this chapter, we will focus on the fabrication and the optical properties of such elements. The results will be used in the interferometric applications presented in chapters 3 and 4.
After an introduction to liquid crystals, we will discuss the optical quality and defects of static LC birefringent elements that have been obtained by using different materials and different alignment methods.

2.1 Introduction

In this section we will give an introduction to the field of thermotropic liquid crystals. We will discuss their principal properties such as phase behavior and birefringence. We will also give a brief review of the principal alignment methods and discuss more specifically the properties of liquid crystal polymers.

2.1.1 Liquid crystal materials

A liquid crystal (LC) is a liquid material that is generally made of elongated rod-shaped organic molecules. In a particular region of the liquid, these molecules (mesogens) tend to arrange themselves along a certain direction called the director. This ordering of the molecules gives the liquid some crystal-like properties such as strong birefringence.
The LC molecules (or mesogenic groups) must have sufficient anisotropy in both attractive and repulsive forces to contribute strongly to the mesogenic phase. Some examples of typical LC molecules [1] are given in Fig. 2.1.

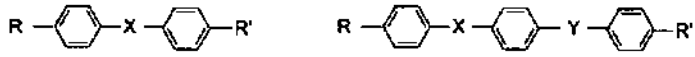

X and Y are covalent bonds or linking units such as:

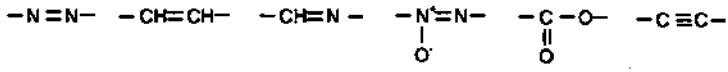

Fig. 2.1: Examples of mesogenic groups composed of aromatic rings joined by linking groups X and Y.

2.1.2 Liquid-crystalline phases

When studying LC, it is important to distinguish the different phases of these materials.

For thermotropic LCs, which are studied in the present chapter, the phase transitions are initiated by changing the temperature. All descriptions are made for conventional materials containing rod like molecules. The most common phases are [1]:

- Isotropic phase: as shown in Fig. 2.2a, in this phase the molecules are oriented randomly without order and the material shows no crystal-like properties. The phase appears as a clear liquid .
- Nematic phase: as shown in Fig. 2.2b, in this phase rod like molecules are aligned along a certain direction (called the director $\vec{n}$) but the center of mass of the molecules is not ordered. The nematic phase is optically uniaxial.
- Smectic phase: as shown in Fig. 2.2c, in this phase rod like molecules are aligned along a certain direction as in the nematic phase and additionally they stay also within a layer. So this phase forms a layered structure. There are a lot of different smectic phases. The most common are: The smectic A (SmA) phase, where the molecules are aligned perpendicular to the layers and the smectic C (SmC) phase, where the molecules are tilted with respect to the layer normal. While the smectic A phase appears optically uniaxial the Smectic C phases is biaxial.
- Cholesteric phase: In this phase the director (local main direction of rod like molecules) has a helicoidal structure. This phase is obtained with chiral molecules or by doping a nematic host with chiral guest molecules in which the local director processes around a single axis. The director is periodic along this axis with a pitch of the helical structure equal to the turn of the local director by 2π.

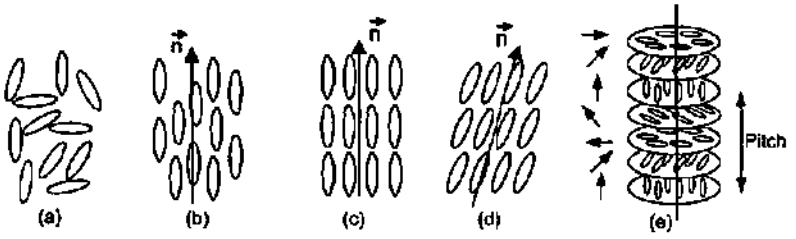

Fig 2.2: Orientation of the molecules (represented by the director $\vec{n}$) when the LC is in (a) isotropic phase, (b) nematic phase, (c) Smectic A phase, (d) smectic C phase, (e) cholesteric phase.

Typically, when decreasing the temperature the order is increased. A typical phase sequence is isotropic phase, nematic phase, smectic phase and finally higher order phases. When decreasing the temperature sufficiently the LC becomes crystalline. We mainly have worked in the nematic phase, which has the wanted uniaxial birefringent properties. Inversely to the smectic phase, the nematic phase is also stable over a broad temperature range and shows generally no major alignment defects when the cell walls are properly treated.

2.1.3 Alignment

Liquid crystals are generally used in combination with a confinement that is a cell that holds the material. The inner surfaces of such a cell are generally treated in some manner to give a particular orientation of the molecules in contact with the substrate surface. Because of elastic interactions in the liquid crystal, this will affect the alignment of the whole volume contained in the cell and ideally will give a large region with a single director. Such a uniform aligned region is called a monodomain. Fig. 2.3 illustrates three different basic alignments that can be obtained by using different surface treatments (or aligning methods). These alignments are:

1) Planar alignment: molecular alignment in which the director is parallel to the substrate. In Fig. 2.3a, the alignment is not completely parallel to the substrate but it is tilted by an angle θ. This angle is called the pretilt angle.
2) Homeotropic alignment: molecular alignment in which the director is perpendicular to the surface substrate (Fig. 2.3b).
3) Twisted alignment: molecular alignment for which the director rotates in a helical fashion when passing between two surfaces having molecules in uniform planar alignment (Fig. 2.3c). The orientation of the directors on the upper and the lower substrate are usually mutually orthogonal, and hence the directors undergo a 90° twist.

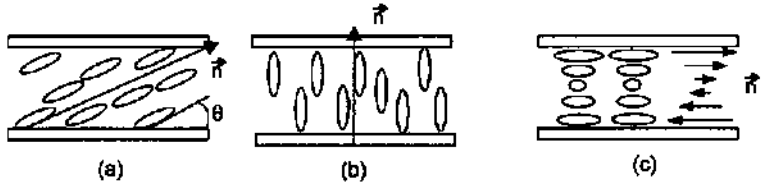

Fig. 2.3: The three different types of alignments obtained between adequate treated surfaces: (a) planar alignment, (b) homeotropic alignment, (c) twist alignment.

The different alignment methods can be divided into two categories: surface alignment produced by adequate treated cell walls and bulk alignment produced by an external electrical or magnetic field.

Surface alignment:
Via an anisotropic surface-LC interaction, the surface defines a well-defined orientation onto the bulk. These interactions can be chemical or due to the topology of the surface. To obtain a planar stable surface alignment, the substrates can be treated with the following methods:

- Rubbed polyimide: the substrate is coated with an adequate polyimide layer and rubbed with a cloth. This is the standard alignment method used in display fabrication. Both, chemical and topological interactions play here a role [2]. The alignment is usually strong and planar with a certain pretilt smaller than 10°.
- Photo-alignment: the substrate is coated with a photosensitive-organic film (constituted of side chain polymers) and the surface anisotropy is obtained by illumination with polarized UV light. Here, the alignment is induced by

chemical interactions [3, 4]. The alignment can be locally structured and the pretilt angle can be chosen in a wide range.

- SiOx deposition: oblique evaporation of silicone oxide on the substrate produces a columnar oblique structure. The alignment is essentially induced by the surface topology. This oblique structure can produce planar alignment with high pretilt angles [5] and different anchoring strength.
- Grooved surface: any substrate with a anisotropic topology (gratings, rubbed substrates...) on the surface can induce a certain alignment of the LC [6].

Homeotropic alignment can be achieved by using amphiphilic materials (surfactants). The polar part of these molecules bonds to the glass and the non-polar part extend into the LC material [5]. A second method is to use coupling agents such as silanes with long alkyl chains and third method is to evaporate SiOx to form columnar structures. In addition, there are special polyimides that allow to implement tilted homeotropic alignments.

Bulk alignment

LC molecules can be aligned with an electric or magnetic field because of their magnetic or electric anisotropy. Uniform textures can be obtained. The applied field produces a certain torque on the molecules and they tend to align them in the same direction depended on the field and the sign of the permittivity.

- Electric Field: For nematic liquid crystals an induced and permanent dipole moment creates a torque to align the molecule parallel or perpendicular to the field $\vec{E}$. The constant of proportionality between the dipole momem per unit volume and the electric field is given by the electric susceptibility χ_e. The anisotropy of χ_e $\Delta\chi_e = \chi_{\parallel} - \chi_{\perp}$ ($\parallel$ and $\perp$ denotes the electric susceptibilities parallel and perpendicular to the director), which is usually positive, will produce the alignment of the LC molecules along the direction of the field. The interaction energy density E_e connected with the reorientation in an electric field is given by [7]

$$E_e = -\frac{1}{2}\varepsilon_0 \Delta\chi_e (\vec{n}\cdot\vec{E})^2, \tag{2.1}$$

where ε_0 is the permittivity of free space. The LC will tend to adopt the configuration where E_e is minimal, which correspond to the situation where $\vec{E}$ and the alignment director $\vec{n}$ are parallel if $\Delta\chi_e > 0$.

- Magnetic field: A magnetic field influences the orbital motion of the electrons, leading to an induced magnetic moment, which in its turn interacts with the applied magnetic field. Due to this mechanism, every molecule subjected to a magnetic field $\vec{B}$ acquires an extra interaction energy is given by [7]

$$E_B = -\frac{1}{2}\frac{\Delta\chi_m}{\mu_0}\left(\vec{n}\cdot\vec{B}\right)^2, \tag{2.2}$$

where μ_0 the magnetic permeability of vacuum. This energy is also related to the anisotropy of the magnetic susceptibility $\Delta\chi_m = \chi_{\parallel} - \chi_{\perp}$ (similar as for the

electric field) which gives rise to an orientation dependence. Most of the LC molecules are diamagnetic, which means that their magnetic susceptibility is negative. In order to minimize the perturbation of the electron motion and so the interaction energy, the rod molecules (and especially the aromatic rings) align themselves rather parallel to the magnetic field.

With bulk alignment only uniform planar or homeotropic alignment can be achieved. More complex textures such as hybrid textures (homeotropic and planar alignment in the same cell) or twisted structures cannot be obtained.

Order parameter:
The morphology of LC between untreated substrates consists of microscopic domains (a few microns) that are strongly ordered locally but their domain directors are randomly distributed to each other. So, we must distinguish two types of order: the local order Q_N (inside one domain) and the domain order Q_D (between domains). The quality of the nematic or local order (alignment) can be defined with the order parameter Q, which is given by [8]

$$Q_{N,D} = \frac{1}{2}\left(\left\langle 3\cos^2(\theta) - 1 \right\rangle\right). \tag{2.3}$$

The brackets denote an averaging over many molecules at the same time or the average over time for the same molecule. As shown in Fig. 2.4, for the local order θ is the deviation angle of the molecule axis from the director. For the domain order, θ represents the angle between the directors of the different domains (ϕ_i in the Fig. 2.4). When the deviation of all the molecules is zero, the LC is perfectly aligned and $Q = 1$. If the molecules are aligned randomly, as it is the case in the isotropic phase, $Q = 0$.

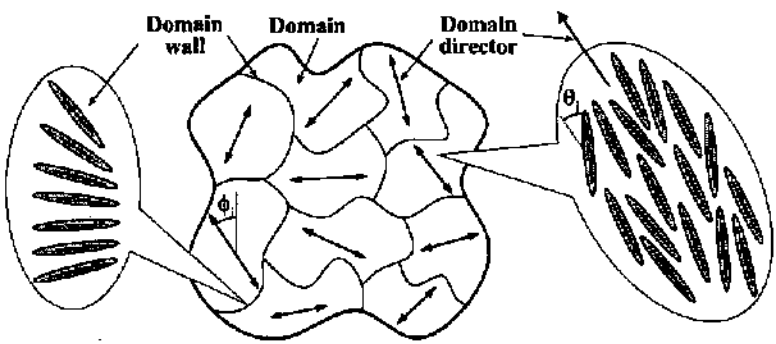

Fig. 2.4: Schematic representation of the LC morphology. On the right-hand the order inside a domain and on the left-hand the boundary between two domains (domain walls).

2.1.4 Liquid crystal polymers

Liquid crystals polymer (LCP) or polymerisable liquid crystals combine the properties of liquid crystals and polymers. LCP can be described as a normal flexible polymer with mesogenic groups (Fig. 2.1) incorporated into their chains. The mesogenic groups give the LC characteristics to the LCP and the flexible spacers (chain) link these groups together to give the polymeric properties.
As illustrated in Fig. 2.5, the placement of the mesogens plays a important role in determining the type of LCP that is formed. Main-chain polymer liquid crystals (MCLCPs) are formed when the mesogens are themselves part of the main chain of a polymer. Conversely, side chain polymer liquid crystals (SCLCPs) are formed when the mesogens are connected as side chains to the polymer backbone by a flexible "bridge" (called the spacer). These spacers decouple the mesogens from the backbone and allow them to move independently. By changing the nature of the mesogenic group and the spacers or by modifying their geometry, length or position and regularity a large variety of LCPs with tailored properties can be obtained. A more detailed discussion of these materials and their properties can be found in [9].

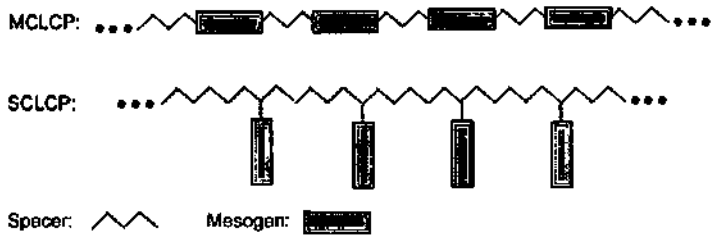

Fig. 2.5: Schematic representation of Main-chain liquid crystal polymers (MCLCP) and side-chain liquid crystal polymers (SCLCP) in terms of spacers and mesogens.

LCPs exhibit the same phases than conventional LC (low molar mass mesogens) that are described in section 2.1.2. However the melting point of LCP is usually much higher (100°-300°C) than for low molar mass mesogens. Many LCPs exhibit a glass transition. The glass transition temperature is defined as the temperature where the material has a certain viscosity and it is for the interesting material classes below 100°C. LCP can be aligned with the same methods as used for conventional LCs (section 2.1.3).
LCP components can be prepared by filling a prepared cell with liquid crystal monomer (LC with polymerizable groups) or polymer. The cell is then heated to the nematic phase. After reorientation of the liquid crystal, there are two methods to freeze the nematic phase: via in-situ polymerization or via vitrification.
All the LCP cells presented in this thesis where fabricated with the in-situ polymerization method. In this method, the aligned monomer is irradiated with UV light for polymerization. The curing process can be controlled by adding adequate quantities of photo-initiator or inhibitor in the monomer LC and by adjusting the UV intensity. One of the advantages of this method is that the material and the cell have not to be heated at too high temperatures (LC monomers has a lower melting temperature then LC polymers). Also once the LC monomer is polymerized, it is very stable and the orientation cannot be disturbed anymore.

In the vitrification method, LCP with a high molar mass that exhibits a glass transition are used. In this method the aligned LC is simply cooled down below the glass temperature transition. Of course, for practical use this glass transition must be significantly above ambient temperature. The main problem is the high viscosity of those materials. They must be heated at a very high temperature to get a chance to align them in a uniform texture.
LCPs (main-chain) are mainly used for high strength plastics because of their chemical stability, poor solubility, high melting point and specially for their excellent mechanical properties. Of course LCPs are in principle not suited for electro-optical applications since the molecules are linked together and consequently cannot be switched by applying any electric or magnetic field, as it is the case in LC displays. But the fabrication of thermally stable birefringent optical (static) components can lead to promising applications of those materials.

2.1.5 Birefringence of liquid crystals

Since LC is an anisotropic material, it is also birefringent. A planar oriented LC nematic cell has similar optical behavior as a uniaxial crystal plate (as discussed in section 1.2.2). The birefringence of LC is relatively high compared to conventional crystals (Tab. 1.1). It can be more then 0.4 [10]. The birefringence ($\Delta n = n_e - n_o$) of liquid crystals is strongly temperature dependent. Fig. 2.6 shows a typical variation of the two ordinary and extraordinary indices n_o and n_e as a function of the temperature.

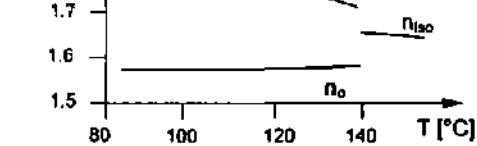

Fig.2.6: typical curves of the refractive indices as a function of temperature.

We see that the birefringence decrease strongly when approaching the isotropic phase and falls to zero when passing the nematic/isotropic transition. This can be easily understood when taking into account that the birefringence is directly related to the order parameter Q (Eq. (2.3)).

2.2 Liquid crystal cell fabrication

To make thick LC components, we need a cell that holds the LC material. To produce the uniform alignment, the LC must be in contact with some treated layer to produce a surface alignment as described in section 2.1.3. We produced essentially three types of cells: wedge shaped cells, planar cells and lenses. Before assembling the substrate surfaces have to be carefully treated. The glass substrates were cleaned in an ultrasonic bath, rinsed with DI water, dried and coated with an alignment layer on a

spin coater. The layers were than adequately treated (rubbed, photo-aligned...). As shown in Fig. 2.7, the wedge shaped and the planar cells were obtained by placing foil spacers between two glass substrates (usually 0.55 mm thick). The cells were filled with LC by capillarity through the inlets and finally sealed with a two component (Araldit) or an UV glue (Norland).

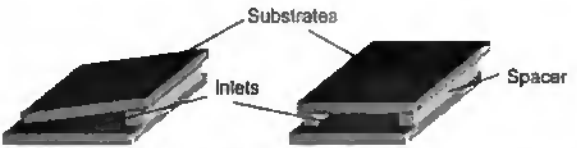

Fig. 2.7: The cells are composed of two treated glass substrates separated by plastic spacers.

The wedge shaped cells are very useful to study the alignment quality as a function of the LC layer thickness. The wedge cells are placed in the setup described in Fig. 1.6. The deformation of the fringes that we get at the output gives a good indication of the homogeneity of the alignment.
Liquid crystal lenses were made of a glass substrate and a plano-concave glass lens. They were prepared as described before for the planar and wedge cells. Since we cannot fill the lenses by capillarity, we filled the glass lens slightly over the edge of the cavity as it is shown in Fig. 2.8a. The glass cover is smoothly posed on the lens and the LC surplus is evacuated on the sides as illustrate in Fig. 2.8b. The difficulty results here by avoiding air bubbles being trapped between the cover and the LC. The lens and the cover are finally sealed together with UV glue.

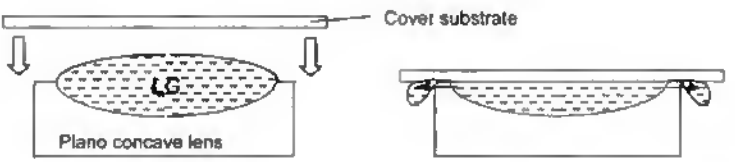

Fig. 2.8: Side view of a plano-concave glass lens filled with LC. (a)The cover is smoothly deposed on the lens, (b) the surplus of LC is evacuated.

The depth of the plano-convex lenses that can be used is limited because of the rubbing process. Since the rubbing cylinder cannot "penetrate" inside the lens; the depth is than approximately limited by the pile length of the rubbing cloth. However, deeper lenses can be used when rubbing manually.

2.3 Nematic LC materials

For static optical components, we are mainly interested in high birefringence and good optical quality i.e. transmission and uniformity of the LC material. It is also important that the LC has a nematic phase over a large temperature range if the final device is used in different ambient conditions. Since the LC is not switched, the

elastic properties, viscosity and electric properties are less relevant. However, the viscosity of the LC should not be too high to be able to fill the cells and the elastic properties should behave normal to speed up the texture relaxation and avoid sensitivity to mechanical disturbances. Of course the materials should also be commercially available.
We have selected a list of 6 different materials from the data delivered by the supplier (Merck). The materials have either high birefringence or good transmission, and large temperature ranges of the nematic phase. The relevant parameters of these materials are summarized in Tab. 2.1.

Designation	Birefringence (Δn) at 20°C and 589 nm	Nematic temperature range [°C]	Cut-off wavelength [nm] (transmission below 20%)
BL006	0.28	<-20 to 113	370
E7 (BL001)	0.22	-10 to 61	350
BL045	0.21	74	350
ZLI-1132 (ML1002)	0.14	-6 to 71	<350
ZLI-1695	0.06	13 to 72	<350
Smectic (Vilnius)	0.18	<20° to 62° (smectic)	400

Tab. 2.1: Characteristics of several LC data from Merck KG.

The investigated LC cells were produced by the procedure outlined in section 2.2. The alignment was made by rubbed polyimide layer (PI 2545 Nissan) for cells with a thickness up to 300 μm. Well-aligned nematic monodomains on surfaces of 20x20 mm^2 are obtained independent of the selected nematic liquid crystal. However, for thick cells (above 100 μm) it takes time until the domain walls are disappeared. The time needed for relaxation was more than 1 hour in some cases. For such thick cells, the alignment becomes very sensitive to dust particles or any other impurities present in the cell.

2.3.1 Absorption

For comparison, we measured the transmission curves of the materials described in Tab. 2.1. The measurements were performed with a Perkin-Elmer lamda900 spectrometer. Since the LC cells were placed in front of an integration sphere, the transmitted light includes also the scattered light. The measurement losses are only due to reflection and absorption. The results are plotted in Fig. 2.9.

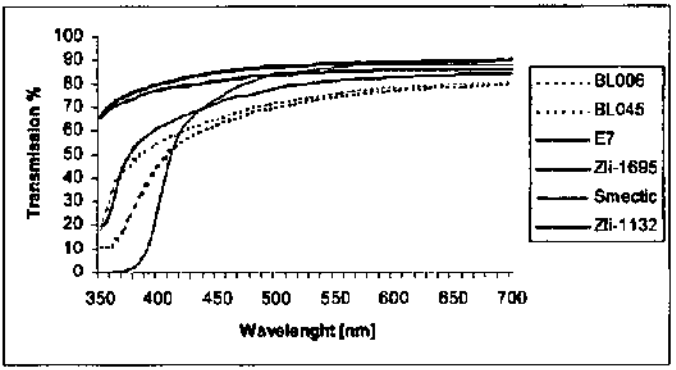

Fig. 2.9: transmission curves of 0.3mm thick glass cells containing

Unfortunately, because of the strong absorption of the glass substrate below this wavelength, it was not possible to measure the transmission values below 350 nm. To exactly determine the cut-off wavelength for ZLI-1132 and ZLI-1695, substrates with a better transmission in the near UV have to be used. However, we can clearly distinguish two groups of LCs. The first group (BL006, E7, BL045) has high birefringence but poor transmission for the blue and in the near UV region. The second group (Zli-1695, Zli-1132) of has lower birefringence but better transmission. Compounds containing highly conjugated electron systems (many delocalized or π electrons) have to be used to obtain high birefringent LC [11]. In such systems the electronic transitions energies are lower. As a consequence, the UV absorption of these compounds extends to wavelength in the near UV [12].
Although we focused on the absorption properties in the visible region of the spectrum, we may add here that we measured good transmission coefficients (~80%) for all the above mentioned LCs in the near infrared region (700-2000 nm).

2.3.2 Scattering

The nematic LC samples look generally milky; this indicates that light is being scattered. The scattering is due to thermal fluctuations, causing a random variation of the director at different points in the cell. The scattered intensity σ is approximately given by [13]

$$\sigma \propto \frac{\varepsilon_a^{\,2} D}{\lambda^4}, \tag{2.4}$$

where D is the thickness of the cell, ε_a the dielectric anisotropy and λ the wavelength. Since ε_a is strongly related to the birefringence, we may expect increasing scattering losses for higher birefringent materials.
We measured for the samples described above the ratio between the scattered light and the total transmitted light with a Perkin-Elmer lamda900 spectrometer. The scattered light was measured by placing a light trap in the integration sphere that

removes the light within a cone of angle 10° around the direct transmitted light beam. The results are summarized in Fig. 2.10.

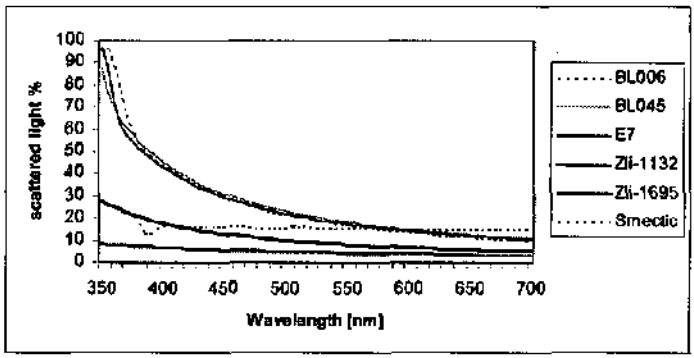

Fig. 2.10: Ratio of the scattered to the total transmitted light for 0.3 mm thick glass cells containing different LCs.

We can distinguish here three categories of LCs. The first two groups are the same ones as already defined for the transmission measurements: the high birefringent ones (BL006, BL045 and E7) and the low birefringent ones (Zli-1132 and Zli-1695). As expected, the first group of LCs scatters much more than the second group. It also interesting to observe that although BL006 has a 30% higher birefringence than BL045, they have both almost identical scattering curves. The third category that contains only the smectic LC shows almost wavelength independent scattering losses. Also, for shorter wavelengths these losses are significantly smaller than for the high birefringent nematic LCs. This is due to the additional order in the smectic LC that restrains some fluctuation modes [14]. The large offset of this curve is probably caused by the numerous defects present in the cell (see Fig. 2.12.). Note that the scattering measurements could not be performed below 375 nm because of the strong absorption of this material.
The scattering losses for the wavelength in the near infrared region (700-2000 nm) are below 20% for all the measured LCs .

2.3.3 Temperature dependence

The temperature dependence of the birefringence of liquid crystals may be critical for applications that need precise phase shifts. By derivation of Eq. (1.33) we obtain the temperature dependence of the phase shift as

$$\frac{d\delta}{dT} = \frac{d\delta}{d\Delta n}\frac{d\Delta n}{dT} = \frac{2\pi \cdot t}{\lambda}\frac{d\Delta n}{dT}, \tag{2.5}$$

We neglected here the influence of thermal expansion of the material on the phase shift. This approximation is certainly valid for the conventional LCs described in this section, but for more stable LCs such as LCPs, thermal expansion may become an important parameter. In this case, we calculate what we will call here "the effective

temperature dependence" which includes eventual influences of thermal expansion of the material on the phase shift.
Experimentally, the temperature dependence of the birefringence can be obtained by observing the fringes produced by a wedge shaped cell in a polarization microscope. The wedge shaped cell is placed in a temperature-controlled chamber provided with a window for up-light observation and illuminated by polarized quasi-monochromatic light. When increasing the temperature of the cell, the fringes are shifted because of the change of the OPD between the two polarization components. The three pictures in Fig. 2.11 show the gradual shift of the fringes (here a quarter fringe) with increasing temperature. This shift can be evaluated quantitatively with a graduated ocular. With the known thickness t (that can be locally considered as constant), wavelength and temperature change ΔT, $\mathrm{d}\Delta n/\mathrm{d}T$ can be determined using Eq. (2.5)

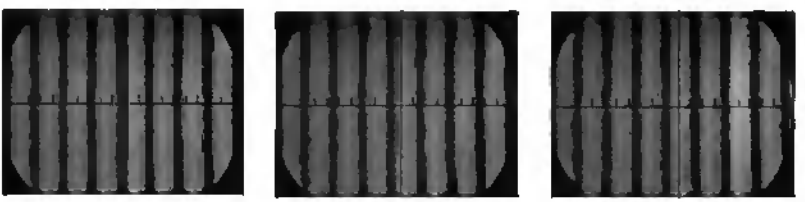

Fig. 2.11: Observation of the fringe pattern produced by a wedge shaped cell in a polarization microscope. The gradual fringe shift (from left to right) of about $\pi/2$ is induced by the change of the temperature.

From the observed phase shift we could deduce a temperature dependence for the BL006 around room temperature of about $\mathrm{d}\Delta n/\mathrm{d}T = 10^{-3}\,\mathrm{K}^{-1}$.

2.4 Smectic LC materials

As seen in the previous section, the major advantage of the smectic A phase are the reduced scattering losses [14]. This is even more important since we are dealing with high birefringent thick optical components.
On the other hand, the problem of smectic materials is that the available materials have only a small stable temperature range and it is difficult to prepare large mono-domain samples. We used a LC smectic A phase mixture that has been prepared by the University of Vilnius and a commercial mixture S7 from Merck. This LC is interesting because it has a smectic A phase over a large temperature range from 60°C to < 20°C (lower temperatures have not been investigated). Because of its high viscosity at ambient temperature, we filled the wedge shaped (0 to 200µm thickness) cell at 100°C by capillarity. We slowly cooled down the cell (0.1°C/min.) through the nematic-smectic transition ($T_{N\text{-}Sm}$=62.5°C). Fig. 2.12a shows the fringe pattern observed in a polarization microscope when placing the obtained cell between crossed polarizers oriented at 45°(as in Fig. 1.6). The LC shows an inhomogeneous alignment with many defects. Fig. 2.12b shows focal-conic defects obtained in a 0.3 mm thick cell (identical processed as the wedge-cell). These defects are typical for smectic phases and a special effort has to be made to avoid them.

Fig.2.12: (a) disturbed fringe pattern of the wedge shaped cell. (b) typical conic-focal defects often present in smectic phases.

We did not succeed to obtain with smectic materials reliable thick birefringent components for optical purposes. It has been found [15] that some special blend of smectic LCs show fewer defects and special alignment procedures like shearing may improve the texture quality. However, the temperature stability and the fabrication difficulties still remain major issues.

2.5 LC polymer materials

Liquid crystal polymers (LCP) are good candidates for the fabrication of passive components. The highly cross-linkable materials are much more robust and less temperature dependent than the conventional LCs. Moreover, these materials can be used in combination with mould replication techniques for mass production or for fabrication of elements with complex geometry. By using the phase sequence and tuning the birefringence due to their temperature dependence the optical properties can be varied. Usually the structures have been frozen in multiple polymerization steps and at different temperatures which allows to obtain a large variety of optical elements [16].
We have investigated the fabrications of optical components with some commercially available low molar main-chain monomers (RM from Merck) and a cross-linkable LC-silicone.

2.5.1 Cross-linkable LC-silicones

For our experiments, we used a mixture (provided by Wacker-Chemie GmbH) of high weight molecules that are constituted of a silicone backbone (siloxane) with in average 5 mesogenic side-chains containing methacryl groups attached to it via a flexible spacer. The material can be cross-linked via their methacryl groups by UV illumination. The cells were assembled as described in section 2.1.3. We used rubbed polyimides from Nissan as alignment layers. The cells had to be filled at approximately 100°C because of the high viscosity of the LC-silicone at room temperature. After filling, the cells must stay in the nematic phase for a certain time for relaxation (15 to 60 min at 100°C). The cells were then cooled down to room temperature (or at the limit of crystallization temperature). Finally, the cells were polymerized with UVA light at 365 nm.

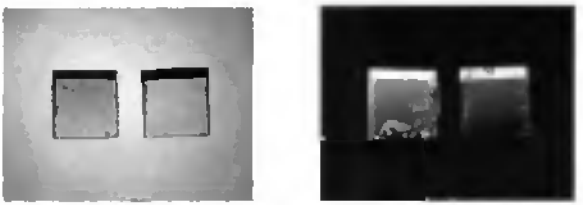

(a) (b)

Fig.2.13: On the left SCLCP wedge shaped cell with 1% of photo-initiator, on the right without photo-initiator. (a) shows the transparency, (b) shows the homogeneity of the alignment between crossed polarizers.

They main problem of thick cell fabrication is the deformation and the resulting stress birefringence due to inhomogeneous shrinkage of the material. They appear during the polymerization process, when intermolecular distances decrease due to the cross-linking of the monomers. The thermal shrinkage that occurs during cooling down of the material can also induce stress birefringence. Figure 2.13. shows, for each picture, on the left hand a 25 mm square wedge-cell with 1% photo-initiator (Irgareure 907, Ciba) and on the right hand an identical wedge-cell without photo-initiator. Both cells have been fabricated as described above. The small quantity of photo-initiator is added to the LC monomer material in order accelerate the polymerization process. Figure 2.13b that shows the two cells between crossed polarizers clearly demonstrates that the cell containing the photo-initiator (left) shows inhomogenities due to stress birefringence. The photo-initiator (activated by UV light) creates monomeric radicals, which initiates the chain polymerization [17]. This means that polymerization velocity increases significantly with the initiator concentration. Apparently, the polymerization process was too fast for the cell containing the high concentration of photo-initiator and the rapid shrinkage of the material caused some distortions of the alignment and stress birefringence. Similar behavior has been observed when illuminating the LC monomers with high UV intensities. This also increases the polymerization rate and consequently causes distortions due to shrinkage.
Similar observations can be made when cooling down the cells too rapidly (more than 5 K/min). In this case the stress birefringence is due to thermal shrinkage. In summary, good cell quality can be obtained by slowly cooling down the LCP to room temperature and by reducing the polymerization velocity (reduce photo-initiator concentration and UV intensity). The drawback of this method may be a lower cross-linkage of the material because of the reduced mobility of the molecules during polymerization.
Another problem that may occur is unwanted absorption of the material. It is visible from Fig. 2.13a that the cell with the photo-initiator becomes yellowish (not visible on the grayscale version of the photo) and absorbs in the blue. This is confirmed by the transmission spectrum shown in Fig. 2.14 obtained with a lamda9 Perkin-Elmer spectrometer. The first curve describe the transmission of a Wollaston prism made of two wedge-cells with 1% photo-initiator and the second curve is related to an identical Wollaston prism without photo-initiator.

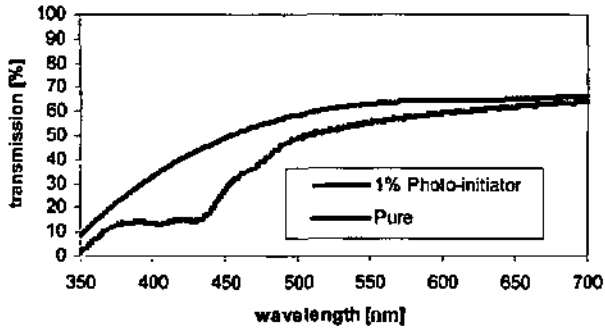

Fig. 2.14: Transmission curve of a Wollaston prism containing 1% of photo-initiator and a wollaston prism containing only the pure LC material.

The difference between the two curves is due to the light absorption of the photo-initiator and his side products created during polymerization. Note that the cells without photo-initiator can hardly be polymerized and it depends on the impurity concentration present in the material which degree of cross-linking one obtains. So, the cells that contain reduce concentrations of photo-initiator have better transmission and show less stress birefringence.
Other, more local defects can also reduce the cell quality considerably. Fig. 2.15 summarizes all these defects. Fig. 2.15a shows air bubbles that may enter the cell during the filling process. These bubbles strongly influence their neighborhood because the trapped oxygen inhibits the polymerization process and produce important deformations around them. Of course, air bubbles can be avoided by using vacuum filling. Fig. 2.15b shows a defect due to crystallization. Actually, when the LC reaches a certain temperature it starts to crystallize but very slowly. In our case visible crystallization started after about 30 minutes at room temperature (when cooling down from nematic phase). Such defects can be avoided by curing the LCP above the crystallization temperature. The last type of defect presented in Fig. 2.15c shows contamination that is already present in the original LCP materials or that is created afterwards. It can be partially removed by dissolving the LCP and filtering methods before application. However, it has been observed so far that there is always some contamination present in the material. The exact reasons for this have not been found.

Fig. 2.15: Different types of local defects encountered in LCP cells (40X magnification). (a) air bubbles, (b) crystallization, (c) material pollution.

Finally, by choosing adequate concentration of photo-initiator (i.e. 0.1% of Irgarcure 907), by curing with adapted UVA intensity (~1-10mW/cm^2) at low temperatures (22°C) and by carefully processing (avoiding air bubbles, crystallization and contamination), we realized cells with good optical quality. Fig. 2.16 shows two 25mm square wedge shaped cells with a maximum thickness of 200 µm: one with a 90° twisted alignment and one with a planar alignment. Rubbed polyimide (PI-2545) is used as alignment layers. The cells show high contrast and good homogeneity.

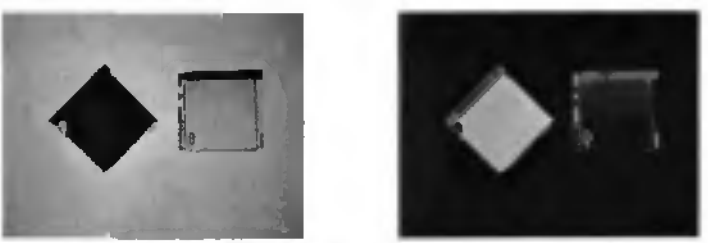

Fig. 2.16: A twisted and a planar cell made of Silicone-LC between parallel and crossed polarizers. The twist cell was rubbed at 45°. The cells show good uniformity and high contrast.

We determined the temperature dependence of the birefringenee assuming a constant volume of the polymerized material with the method described in section 2.3.3. We found that around room temperature and for a wavelength of 550 nm the temperature dependence of the birefringence is situated between $10 \cdot 10^{-5}$ and $5 \cdot 10^{-5}$ K^{-1}, depending on the polymerization degree of the sample. By using a post-polymerization method (polymerization at 80°C for several days), we could reduce this dependence by a factor 5 to $1 \pm 0.5 \cdot 10^{-5}$ K^{-1}. Note that these results represent an average temperature variation over a temperature range from 20°C to 60°C. Eventual non-linear behavior could not be measured with this method. More accurate results are presented in chapter 3.

2.5.2 Cross-linkable liquid crystal mesogens

For our experiments we used two slightly different materials. The chemical structures of these LCP are given in Fig.2.17. The molecules are constituted of a mesogenic unity with acrylate groups on both sides. The acrylate groups are separated from the central aromatic core by flexible methyl spacers of variable size. Some photo-initiator (Irgacure 819) was added to the LC monomer in order to start the free-radical chain polymerization when illuminating with UV light. Alignment, photo-polymerization kinetics, birefringence, temperature dependence and phase transitions of such materials has already been reported [18-24] and [28]. RM-82 is nematic from 86° to 116° (when heating) and RM-257 from 70° to 125°. During cooling the crystallization temperatures occurs at lower temperatures: it starts about 35° for RM-257 and about 63° for RM-82; for lower temperatures the material begins rapidly to crystallize. Mixtures of mesogenes show generally an extended nematic range [25]. So, to decrease the crystallization temperature we mixed both LC monomers (50% of each). In this way, we were able to decrease the crystallization temperature (that was determined by microscope observation) of the material close to room temperature (25°C). Note that this mixture has not been optimized and it does not necessarily correspond to the eutectic point.

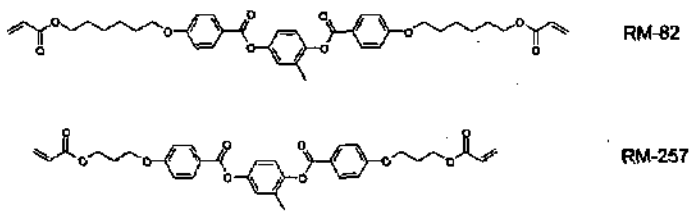

Fig. 2.17: Chemical structure of two liquid-crystalline acrylates having side groups of different lengths (6-carbon spacers for RM-82 and 3-carbon spacers for RM-257).

After polymerization in the nematic phase the molecules form an ordered crosslinked network. Since the mesogenic units are uniaxially oriented along the rubbing direction in the nematic phase, the material shows the same optical properties as conventional LCs.

As for the SC-LCP we used wedge shaped cells with rubbed polyimide as alignment layer. Since the material is solid at room temperature, we filled the cells by capillarity at 110°C. After 15 min relaxation time (until the domain walls disappeared), the cells were cooled down at room temperature (3°C/min.) and polymerized by UV illumination (~1mW/cm^2). As already observed for the SC-LCP, the cells show important alignment inhomogenities due to shrinkage during polymerization [23] and due to thermal shrinkage, which has been studied for polymerized films in [24]. Best results were obtained when decreasing the polymerization temperature and polymerization rate. The latter can be realized by polymerizing at lower UV intensity or lower temperature and by using very low concentration of photo-initiator.

We determined the effective temperature dependence at assumed constant volume of the birefringence of the polymerized material as described in section 2.3.3. Because of the very high stability of the material, we could not observe any phase shift by

varying the temperature. A more accurate measurement method is necessary. Nevertheless, we can state that the effective temperature dependence of the birefringence is lower than 10^{-5} K^{-1}. Also Broer et al. [20] did not find any birefringence variation for temperatures below 90°C for similar materials.

2.5.3 Absorption and scattering losses of the polymer materials

We present here the measured absorption and scattering losses of thick planar aligned cells made of LCP. We prepared two 300 μm thick cells (with 0.55 mm glass substrates) filled with RM-257 and LC-silicone. A small amount ($1^0/_{00}$ of the total weight) of photo-initiator was added to the LCs to initiate the polymerization. The measurements were performed exactly as described in section 2.3.1 and 2.3.2. The results are reported in Fig. 2.18.

a)

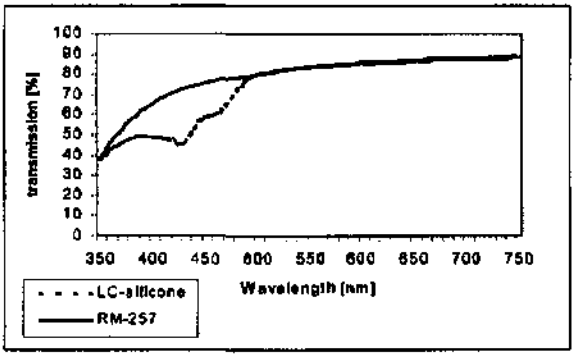

b)

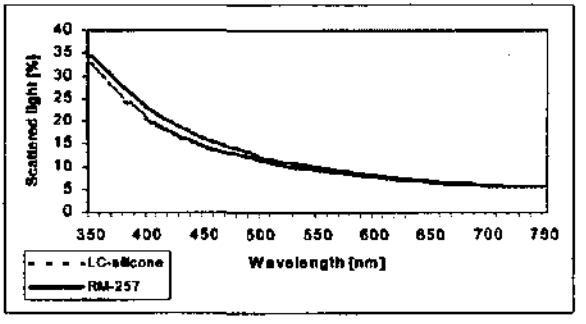

Fig. 2.18: Measured absorption and scattering losses for 300 μm thick cells filled with polymerized RM-257 and LC-silicone. (a) Total transmitted light, (b), ratio of the scattered light to the total transmitted.

When comparing graph (a) with the transmission curves of Fig. 2.9, we see that the curves a relatively similar. The transmission of the LCPs is situated somewhere in between the low and the high birefringent conventional LCs. The transmission dip of the LC-silicon between 380 and 500nm is probably due to the presence of photo-initiator in the LC. Similar behavior has been already observed in Fig. 2.14.
When comparing Fig. 2.10 with graph (b), we note that the LCPs apparently do not scatter as much as the conventional LCs. For example, E7 shows scattering losses of 45% at 400 nm. The LC-silicone that has a birefringence ($\Delta n = 0.2$) comparable to the LC-silicone shows only 20% losses for the same wavelength.

2.6 Alternative alignment methods

In the previous sections the alignment of the LC has been obtained with rubbed polyimide. This alignment method is very common and gives good results nearly independent from the liquid crystal mixture. However, pretilt angles of more than 10° are difficult to obtain and even for lower pretilt angles it is not obvious to obtain reproducible results. So, the optical axis orientation is limited to planar. This of course is a serious constrain for the optical design. Another disadvantage of this alignment method is the rubbing process step. It is not suited for processing non-planar elements such as prisms or lenses. Dust particles might be produced by detaching some polyimide from the substrate and will contaminate the system. The alignment layer is also very sensitive to contact, and scratches destroy the alignment completely. In this section, we will present two alternative alignment methods, which do not need rubbing.

2.6.1 Magnetic alignment

As already presented in section 2.1.3, this method is based on the alignment of mesogenes that show anisotropic magnetic susceptibility in a magnetic field.
This alignment method offers many advantages. The magnetic field aligns over much greater distance than rubbed substrates because the forces act on all the molecules of the bulk, therefore we may expect even for thick components good alignment and uniform mono-domains. In addition, the internal walls of the glass substrates need no particular treatment.
As described in section 2.1.3, the mesogenes align with respect to the magnetic field in such a way that the free energy (given by Eq. (2.2)) is minimized.
Due to the thermal fluctuations, the actual orientation of the molecules in the magnetic field will have a certain orientation distribution function

$$f(\theta) = \exp\left(-\frac{|\Delta\chi|\cdot B^2}{\mu_0}\cdot\frac{1}{2kT}\cdot\sin^2\theta\right), \text{ for } \Delta\chi > 0, \tag{2.6}$$

which is given by the Boltzman statistics [26]. Typical values of $\Delta\chi$ ($\sim 10^{-7}$) indicate that the magnetic field induced alignment of individual molecules is a very small effect compared to kT. However in the case of collective molecular behavior, such as in the liquid crystalline mesophase, the magnetic field energy gain may become comparable with thermal fluctuations, allowing an important degree of orientation to be achieved. In this case the orientation distribution is given by [27]

$$f(\theta) = \exp\left(-N_\xi \cdot Q \cdot \frac{|\Delta\chi| \cdot B^2}{\mu_0} \cdot \frac{1}{2kT} \cdot \sin^2\theta\right), \text{ for } \Delta\chi > 0, \tag{2.7}$$

where N_ξ is the number of molecules acting collectively and Q describes the strength of the collective behavior, $0 \le Q \le 1$. In the case of LC, Q_N is the local order parameter given by Eq. (2.3), which describes the mesophase.

A number of experiments, which had as purpose to produce well-aligned LC polymer elements, have been performed at the high magnetic field laboratory of the University of Nijmegen. The experimental setup consists essentially of a 20 Tesla Bitter magnet, a temperature controlled chamber and an optical setup. For the alignment experiments, the sample is placed in the chamber and introduced in the core of the magnet. Via a mirror system and a window placed in the sample holder, a HeNe laser beam passed trough the sample, which enables real time (in-situ) transmission and birefringence measurements. The phase retardation between the two polarization components can be measured in-situ with an optical setup employing a photoelastic modulator that modulates the input polarization state. When placing a second polarizer at the output of the system the detected intensity will also modulate. The change of the phase retardation can be retrieved from the modulation variation of the output signal. A more detailed description of the setup and the measuring method can be found in [27]. Note that this measuring method gives only the relative phase shift with respect to the initial phase shift. Absolute values can only be found when starting the measurements with a zero or known birefringence value.
In the following experiments we compared the alignment of three identical 50 μm thick planar samples (10x20 mm) filled with side-chain LC monomers (described in section 2.5.1) for various applied magnetic fields. The samples were hold at 105°C (20° below isotropic transition temperature) during the whole experiment. The graph in Fig. 2.19 shows the phase retardation variation as a function of the alignment time for three different magnetic field strengths (5 T, 10 T and 15 T). Since the birefringence and hence the phase retardation is proportional to the order parameter of the LC, we can say that the curves represent the order of alignment as described in Eq. (2.3). As already discussed in Eq. (2.7), the magnetic field effects are small at the level of individual molecules and thus should not affect the local order Q_N. In domains, the molecules act collectively and the magnetic filed is susceptible to orient the different domains and so increasing Q_D. Since the cross section of the beam is larger than one domain, the measured birefringence is proportional to the increase of Q_D that is produced by the rotations of the domains.

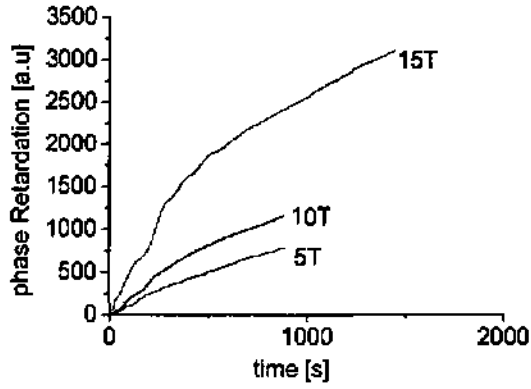

Fig. 2.19: phase retardation as a function of time for three similar samples aligned in a magnetic field of 5 T, 10 T and 15 T, respectively, at 105°C.

As expected, higher applied fields induce faster alignment processes. Although we made measurements for only three different field strengths, the differences between the curves suggest some non-linear dependence between the field strength and the alignment time. We see also that the curves do not reach saturation. This indicates that the LC was only partially oriented when switching off the field. Unfortunately, exposition times were limited because of the high electrical power consumption of the magnet. When observing the 15 T curve, we can clearly distinguish two different rates of retardation changes. These two alignment stages are less pronounced for the 10T and the 5T curves. A possible explanation would be that in the first phase the domains rotate relatively freely and the birefringence increases quickly. In the second phase, the domain walls have to move and to disappear in order to create monodomains. This last phase, which is a sort of polydomain-monodomain jump, may be a slower alignment step than the fist phase.

In some other alignment experiments with the same material we have tried to cool down the samples from isotropic phase to almost room temperature in a constant magnetic field from 5 T to 15 T. Once the samples reached room temperature, we polymerized them in-situ. After polymerization, the samples where inspected between crossed polarizers under the microscope. Almost all the samples show a global alignment but with many domain walls and contamination. Unfortunately, samples with an acceptable optical quality could not be obtained in a reproducible way.

The following set of experiments illustrates the non-reproducibility of alignment quality. We used three identical cells made of cleaned but untreated glass substrates filled with LC monomers (RM-82, Fig. 2.17). However, we must note here that the three sample cells had slightly different inhibitor (HQME) concentrations. The samples were (as far as possible) identically processed. They were placed inside the magnet and heated up to 140°C for 10 minutes. After cooling down at 3 K/min to 100°C in a magnetic field of 5 T, the cells were polymerized at 100°C for 15 minutes with a UV intensity of approximately 10 mW/cm^2 leaving the magnetic field switched on. Figure 2.20 shows a 3x3 mm area of the obtained samples placed between crossed polarizers.

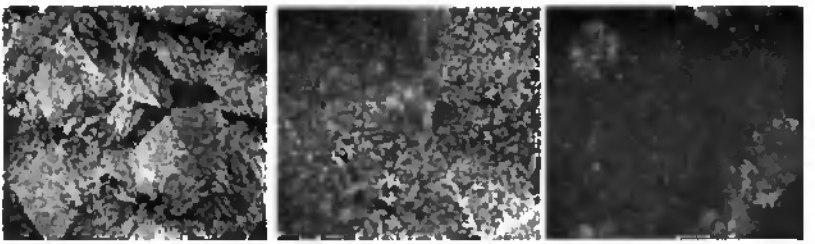

(a) (b) (c)

Fig. 2.20: Three almost identical prepared RM-82 samples (50μm thickness) observed between crossed polarizers (4X magnification).

The pictures demonstrate clearly an increasing quality of the alignment from (a) to (c). Convincing explanations for these results could not be found. First, it can be due to slight variations of the curing process. We can imagine that slower polymerization rates induce less deformation of the alignment. However, such (very local) deformations were not observed when polymerizing samples that were aligned with the help of rubbed polyimide surfaces. Also, real time measurement (made with another setup using a weaker magnet of 1.5 T) of the alignment during the polymerization process did not show any perceptible alignment deformations apart from some stress birefringence. An additional explanation could be that impurities due to some thermal polymerization occur during the experiment that hinders the LC monomers from aligning correctly. Similar observations have been reported in [28]. However, the experiments were made over a short time interval (~4 hours) and no thermal polymerization has been observed so far when working with this material in combination with inhibitor over such a short time. It may also be possible that the microscopic surface structure of the glass surface as well as the filling procedure, which gives the initial alignment (and domain structure) of the LC (and which can vary from cell to cell), plays a role. Such effects have important influence on the alignment quality for polymer liquid crystals. In other words, the alignment forces due to the magnetic field might be not strong enough to completely overcome the surface anchoring forces or to break down the domain walls [29].

In a second experiment made with a weaker continuous magnet of 1.3 T in the laboratories of ASULAB (Marin, Switzerland). We compared the alignment of two different LCPs. We aligned two wedge shaped cells: the first cell was 200μm thick and was filled with RM-82 (see Fig. 2.17), the second cell was only 50μm thick (because of the limited available quantity) and was filled with a slightly different LCP call here 3d. We could monitor in real time the alignment produced by the magnetic field by observing with a CCD camera the interference fringes produced by the setup of Fig. 1.6. The measured interference fringes which are shown in Fig. 2.21 were obtained by heating the LCP into the isotropic phase and by cooling it down into the nematic phase (about 100°C) in a 1.3 T magnetic field. The alignment is mainly produced during the first seconds after entering the nematic phase. After this time no significant changes in the alignment has been observed. We found that passing the isotropic-nematic transition with applied magnetic field is necessary to obtain good alignment.

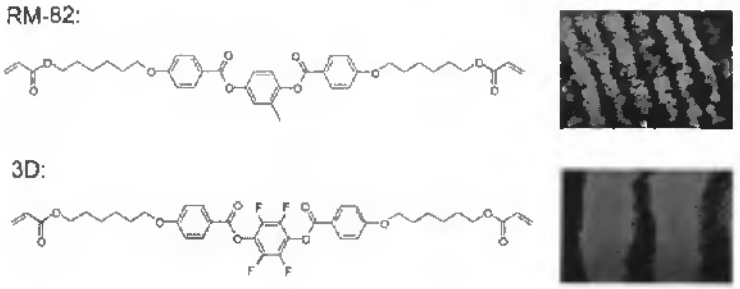

Fig. 2.21: Chemical structure of the liquid crystal polymers and the corresponding interference fringes measured with the magnetic aligned wedge cells.

The images of fringes show an area of about 3x4 mm. For RM-82, the gray zones between the black and white strips indicate local distortions of the alignment. For 3D, the strips are more separate because of the thinner wedge cell. Here, we do not see such gray zones and the contrast is higher which indicates a better alignment. These results were confirmed by microscope observations of the polymerized cells. The better results obtained for the 3D LCP may be explained by the lower viscosity of the material. So, by choosing the adequate material the alignment can also be induced with lower magnetic fields.
These two experiments show that many parameters, such as boundary conditions, material properties and magnetic field intensity, seem to influence the alignment of the liquid crystal. But all the mechanisms are still not fully understood and further investigations are necessary before making any final statements.

2.6.2 Photo-alignment

In the photo-alignment method, the anisotropy of the alignment layer is created by illuminating the substrate coated with linearly photo-polymerizable polymer with polarized UV light. The main advantage of this method is that it has no rubbing process and contamination can be prevented. It offers the possibility to fabricate structured optical elements (for instance twisted-planar alignment patterns) by masking surface areas. However, interactions causing the alignment are mainly chemical and the photo-alignment material is not "universal". Only some specific photo-alignment - LC combinations give good results and one has to make careful investigations to obtain stable and reproducible results for each new liquid crystal mixture.
Several combinations have been tested. We found that a good alignment can be obtained by using a photo-alignment layer from Cheil (Korea) in combination with the LC ZLI-1132 from Merck. We produced a 0.2 mm wedge shaped cell with this alignment method. First, the substrates were ultrasonic cleaned and spin-coated with the photo-alignment material. Then, they were shortly baked at 100°C for 10 minutes to evaporate the solvent. As shown in Fig. 2.22, the substrates were illuminated with collimated and polarized UV light (Oriel lamp 1mW, exposure time 30 min.). The

light was polarized with a sheet-polarizer (HNP-B from Polaroid) with a transmission in the UVA region.

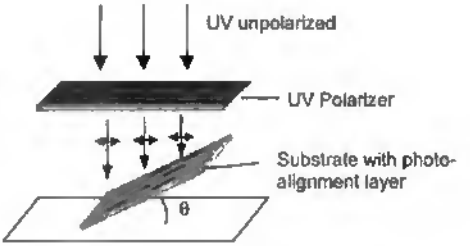

Fig. 2.22: UV illumination system for photo-alignment of the surface layer. The Collimated UV light is polarized with a UV polarizer before arriving on the photo-alignment layer of the substrate.

A picture of the assembled wedge-cell is shown between crossed polarizers in Fig. 2.23a. Apart from a few scratches, the LC shows a homogenous alignment without defects over the whole cell (20x23 mm). Fig. 2.23b shows the fringe pattern at an area of 2x3 mm obtained in the setup described in Fig. 1.6. and illuminated with green light at 550 nm.

Fig. 2.23: alignment quality of a 200μm wedge-cell obtained with a photo-alignment layer. (a) Between 0° and 90° oriented polarizers (left). (b) regular fringe pattern obtained when placed between 45°oriented polarizers (right).

The high contrast and constant spaced fringes indicate that there are no unwanted birefringence variations and deformations of the texture. In principle (according to the fabricant specifications), it should be possible to produce high pretilt angle (>10°) by controlling the tilt angle θ of the substrate during the exposure. However, we could not measure any change of pretilt angle for different values of θ.
This technology offers the possibility to produce cells with various alignment patterns by using photo-masks and varying the polarization direction of the UV-light. Figure 2.24 shows a flexible polymerized liquid crystal film of 0.13 mm thickness between crossed polarizers.

Fig. 2.24: Flexible structured film with three different alignment zones hold between crossed polarizers.

It has been produced by filling a cell with a reactive mesogene (RM-257 form Merck) that has a structured photo-aligned substrate and a rubbed counter substrate. Two illumination steps were necessary to structure the photo-alignment:

1) A printed transparent foil is used as mask and the substrate is illuminated with 0° polarized light. This produces three zones: a non-illuminated zone (CSEM), a zone that has been illuminated through the birefringent foil (oriented at 45°) and a zone that is directly illuminated (below CSEM).
2) The foil is removed and the substrate is illuminated with 90° polarized light. This only affects the non-illuminated zone (CSEM) from the previous step.

After these two polymerization steps, the cell is opened (separate the substrates) and the polymerized film is removed manually from the substrates. So finally we end up with a flexible film having three different aligned zones that correspond to the gray levels of the image: planar, 90°twisted and -45° twisted alignment.

2.7 Conlusion

In this chapter, it has been shown that birefringent optical component can be made of liquid crystals. However, we found also many limitations. Due to absorption and scattering losses LC components are not suited for near-UV applications, especially when important phase shifts are required. In the visible region, apart from the transition region around 430 nm (400-450 nm), absorption and scattering becomes less critical. The optical properties of the LCs are particularly well suited for NIR applications. Generally, cell thickness is limited at about 300-500 µm, depending of the LC that is used. Above this limit domain walls become frequent. These restrictions set the maximum obtainable phase shift to about 150µm (0.3x 500 µm). Another disadvantage is the limited pretilt angle (max. 10°) that can be obtained with the present alignment technologies. This may in some cases restrict the optical design.
For many applications, temperature stability and robustness are important advantages. Contrary to conventional nematic LCs, liquid crystal polymers have these properties. It has been shown that optical components with good optical quality can be produced with such materials. This opens of course many interesting perspectives for applications where the use of crystals would be too expensive. Some examples will be treated in the next chapters. However, LCPs suffer from the same optical limitations (scattering and absorption) as the conventional LCs.
With alternative alignment methods, such as the photo-alignment combined with LCPs, it is possible to fabricate thin structured birefringent elements. This technology offers new and interesting design perspectives.
In principle, bulk alignment with magnetic fields should be possible. Such an alignment method would overcome the problem of the limited cell thickness are

obtainable with surface anchoring. However, we did not succeed to produce such cells in a reproducible way.
Finally, we can summarize the obtained performance of the investigated LCs in Tab. 2.2.

Material family	Birefringence	Cut-off wavelength (for 0.3mm thick cells)	Alignment uniformity	Effective temperature dependence of birefringence [1/K]
Conventional LCs	0.14 - 0.28	<350nm (380nm)	Very good	10^{-3} K^{-1}
SCLCP (Silicone polymers)	0.2	400nm	Acceptable	10^{-3} K^{-1}
MCLCP (diacrylate monomers)	0.14	400nm	good	$<10^{-3}$ K^{-1}

Tab. 2.2: Summary of the performances of the different LC families. The temperature dependence is given here as defined in section 2.3.3.

Of course, the above-mentioned performances apply only to the materials that have been investigated in the present work.

2.8 References

[1] M. Barón, "Definitions of basic terms relating to low-molar-mass and polymer liquid crystals", Pure Appl. Chem., 73 (5), pp.845-895, 2001.

[2] P. Chatelain, "Sur l'orientation des cristaux liquides par les surfaces frotées," *Bull. Soc. Fr. Min.* **66**, 105, 1943.

[3] M. Schadt and H. Seiberle, "Optical Patterning of Multidomain Liquid Crystal Displays", SID 1997.

[4] M. Schadt, K. Schmitt, V. Kozinkov and V. Chigrinov, "Surface-Induced Parallel Alignment of Liquid Crystals by Linearly Polymerized Photopolymers.", *Jpn. J. Appl. Phys.* **31**, 2155-2164, 1992.

[5] M. G. Tomilin, "interaction of liquid crystals with solid surface", *J. Opt. Technol.* **64** (5), p.452, 1997.

[6] D. W. Berreman, "Solid Surface and the Alignment of an Adjacent Nematic Liquid Crystal", *Physical Review Letters* **28** (26), 1972.

[7] P. J. Collings and M.Hird, *introduction to liquid crystals*, pp.195-202. Taylor & Francis, 1997.

[8] P.J. Collings and M.Hird, *introduction to liquid crystals*, p.1. Taylor & Francis, 1997.

[9] A. M. Donald, A.H. Windle, *Liquid Crystalline Polymers*. Cambridge University. Press, 1992.

[10] C. Khoo, S.T. Wu, *optics and nonlinear optics of liquid crystals*, p.96, World Scientific, 1993.

[11] C. Khoo, S.T. Wu, *optics and nonlinear optics of liquid crystals*, pp. 22-49. World Scientific, 1993.

[12] H. Stegemeyer, *Liquid Crystals*, Topics in physical chemistery Vol. 3; Steinkopff, Darmstadt; Springer, New-York, 1994.

[13] P. G. de Gennes, J. Prost, *The physics of liquid crystals*, 2nd ed., p.146. Oxford university. Press, New York, 1993.

[14] P. G. de Gennes, J. Prost, *The physics of liquid crystals*, 2nd ed., p.371. Oxford University. Press, New York, 1993.

[15] C. Titus, P. J. Bos and O. D. Lavrentovich, "Efficient, accurate liquid crystal digital light deflector", Proc. SPIE **3633**, 244-253, 1999.

[16] D. J. Broer, "Creation of supramolecular thin film architectures with liquid-crystallines networks", Mol. Cryst. Liq. Cryst. **261**, pp. 513-523, 1995.

[17] P. w. Atkins, *Physical Chemistry*, fifth edition. Oxford University Press.

[18] D. J. Broer, H. Finkelmann and K. Kondo, "in-situ photopolymerization of oriented liquid-crystalline acrylates,1.-Preservation of molecular order during photopolymerization", *Makromol. Chem.* **190**, 19, 1989.

[19] D. J. Broer, G.N. Moll, G. Challa, "in-situ photopolymerization of oriented liquid-crystalline acrylates,2.-Kinetic aspects of photopolymerization in the mesophase", *Makromol. Chem.* **190**, 19, 1989.

[20] D. J. Broer, J. Boven, G.N. Moll, G. Challa, "In-situ photopolymerization of oriented liquid-crystalline acrylates,3.-Oriented polymer networks from mesogenic diacrylate", *Makromol. Chem.* **190**, 2255-2268, 1989.

[21] D. J. Broer, R.A.M Hikmet, G. Challa, "In-situ photopolymerization of oriented liquid-crystalline acrylates,4 –Influences of a lateral methyl substituent on monomer and oriented network properties of a mesogenic diacrylate", *Makromol. Chem.* **190**, 3201, 1989.

[22] D. J. Broer, G.N. Moll, G. Challa, "In-situ photopolymerization of oriented liquid-crystalline acrylates,5.-Influence of the alkylene spacer on the properties of the mesogenic monomers and the formation and properties of oriented polymer networks", *Makromol. Chem.* 192, 59, 1991.

[23] R. A. M. Hikmet, B. H. Zwerver, "Anisotropic shrinkage behaviour of liquid-crystalline diacrylates", *Polymer* 33, 89, 1992.

[24] D.J. Broer and G.N. Mol, "Anisotropic Thermal Expansion of Densely Cross-Linked Oriented Polymer Networks", *Polymer Engineering and Science*, 1991, 31, p. 625-631.

[25] P.G. de Gennes, J. Prost, *The physics of liquid crystals*, 2nd ed., p.91. Oxford Univ. Press, New York, 1993.

[26] G. Maret, K. Dransfeld, *Topics in Applied Physics*, 57, 143-204. Ed. F. Herlach, Springer, Berlin, 1985.

[27] M. I. Boamfa, "Manipulation of molecular structures with magnetic fields", PhD Thesis, University of Nijmegen, The Netherlands, April 2003.

[28] J.W. Schultz, and R.P. Chartoff, "Photopolymerization of nematic liquid crystal monomers for structural applications", *Polymer* 39, p.319, 1998.

[29] P.G. de Gennes, J. Prost, *The physics of liquid crystals*, 2nd ed., p.91. Oxford Univ. Press, New York, 1993.

Chapter 3

Hand-held Fourier spectrometer

In this chapter, we present the optical design and realization of a LC Fourier transform spectrometer (FTS). This FTS is based on a polarization interferometer that has a Wollaston prism made of LC material as key component. After a brief introduction into Fourier spectrometry, we will show original optical designing methods and new spectrometer configurations. Then we will show a practical realization (with conventional LC and polymer LC) of the most suitable design in a hand-held version of a FTS for measurements in reflection. The performances of the different designs and materials such as compactness, angular dependence (field of view), resolution, stray light and temperature dependence will be discussed.

3.1 Introduction

In comparison to other types of spectrometers such, as diffraction gratings or Fabry-Perot resonators, the Fourier Transform Spectrometer (FTS) has well-known throughput and multiplex advantages. This can give the FTS with a better signal-to-noise ratio. This also allows to have very high resolution, even for low intensity sources. The actual commercially available FT spectrometers are mainly used for application in near and far infrared region for chemical analysis or astronomical observations. They contain highly precise moving parts and are consequently large, expensive, fragile and can only be used in protected environments. So, they are obviously not suited for applications needing compact and robust spectrometers, such as for example portable devices. Mostly grating spectrometers are used for such applications. They are fabricated with well-established technologies and consequently they are relatively inexpensive. They have also the advantage to be robust and generally they do not need important signal processing power.
The aim of the present work is to fabricate a spectrometer that overcomes the drawbacks of the common FT spectrometers and keeps as much as possible the benefits of it. For this purpose, we need a compact monolithic FTS that can be fabricated with low cost technologies. To achieve this goal, one approach presented by Manzardo [1] is to miniaturize a static Michelson interferometer with a tilted mirror. Another approach by the same author [2] is the fabrication of a time scanning Michelson interferometer by using silicone micromachining technology. A similar approach is presented in [3] were a 10 cm large scanning Michelson has been microfabricated.
In the next sections we will present a monolithic low-resolution static FT spectrometer that is based on a polarization interferometer using a Wollaston prism as phase shifter. Since the fabrication of this device uses inexpensive liquid crystal technology and needs no particularly sensible adjusting or assembling procedures, it may become an interesting candidate for applications in the VIS or NIR region.

Applications such as colorimetry in the graphic industry, quality inspection or environment monitoring might be envisaged. We will discuss later on miniaturizing possibilities via alternative optical designs and present the performances of this spectrometer.

3.2 Optical principle

All Fourier transform spectrometers are based on the relation between the temporal coherence of the source and the spectrum of the incident light, which is given by the Wiener-Kintchine theorem (Eq. (1.40)). As already mentioned, the present FTS is a static common path polarization interferometer. The optical principle is very similar to the single prism setup presented in chapter 1 (Fig. 1.6). The only difference here is that the birefringent system is composed of two prisms (Wollaston prism) in order to shift the zero path difference to the center. An enlarged version (with lenses) of this FTS is schematically shown in Fig. 3.1. The principle is shortly explained here below:

1) The divergent incident light is collimated with a collimation optics.
2) The light is linear polarized at 45° with a dichroic sheet polarizer.
3) The light is decomposed into two linear polarization components x and y by the Wollaston prism. Due to the birefringence and the perpendicular (*x*- and *y*-) orientation of the optical axes, the two wedge-shaped prisms produce a spatially varying phase shift in y direction between the two perpendicular (*x*- and *y*-) polarization components. Similarly to Eq. (1.33), the phase shift at the output of the Wollaston is given by

$$\delta = \frac{2\pi}{\lambda} 2\left(n_e - n_o\right)\tan(\phi) y, \tag{3.1}$$

4) The two polarization components are recombined at the second polarizer (or analyzer), which is oriented at ±45° to obtain maximal contrast.
5) With the help of the imaging optics the interference pattern, which is virtually localized inside the Wollaston prism, is imaged onto a photodetectorarray (PDA).
6) Finally, a numerical Fourier transformation of the spatial intensity distribution gives the spectral intensity.

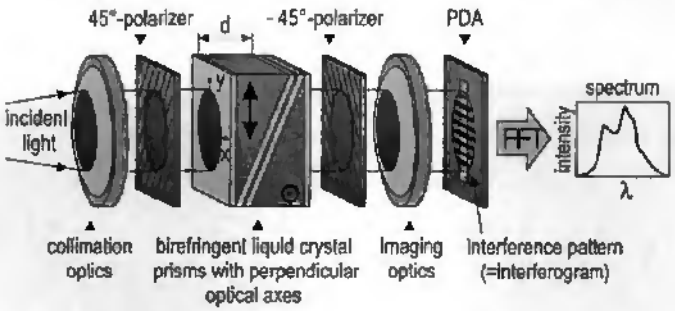

Fig. 3.1: Optical principle of the Fourier transform spectrometer based on a Wollaston prism

From Eq. (1.45), the measured intensity (interference) pattern I_{out} is given by:

$$I_{out}(\vec{r}) = \int_{\nu} \frac{1}{4} \cdot I(\sigma) D(\sigma) T(\sigma) K \cdot (1 + |\mu_{12}(\vec{r}, \sigma)| \cos(\delta(\vec{r}, \sigma))) d\sigma , \tag{3.2}$$

where μ_{12} is the spatial coherence given by Eq. (1.44), δ the phase shift given by Eq. (3.1), $T(\sigma)$ the transmittance of the optical system, $D(\sigma)$ the spectral sensitivity of the detector, K the fill factor (and size) of pixels of the detector and $I(\sigma)$ the input intensity from the homogenous polychromatic extended light source. The above formula does not take into account possible contrast reduction due to scattering or to not ideal polarizers. It also supposes that the spectrometer has no defects (phase distortions) and infinite length (no truncation). We will not determine the influence of each parameter (D, A, K, μ) individually. We suppose here that all these parameters are independent of the incoming intensity (if the saturation level of the detector is not reached). The measured spectra from various samples will be divided by a "white spectrum". This normalization spectrum can be obtained from a special white reference for reflection measurements or directly from the source (without sample) for transmission measurements. So, at the end we will have a normalized spectrum with respect to a defined white spectrum.

For simplification reasons, we will discuss the theory by expressing the interferograms as function of the phase shift $\delta(y)$ and the spectra as function of spatial Fourier frequencies.

If we suppose that μ_{12} is constant over the spatially extended interferogram (along the y axis), we can rewrite Eq. (3.2) as

$$I(\delta(y)) = \int_{0}^{\infty} B'(\sigma) \cdot (1 + \cos(2\pi\sigma\delta(y))) d\sigma , \tag{3.3}$$

where B' is the spectrum as seen by the spectrometer. It can be retrieved by applying a Fourier transform

$$B'(\sigma) = FT\{I(\delta)\} = \int_{-\infty}^{\infty} I(\delta)\cos(2\pi\sigma\delta)d\delta . \tag{3.4}$$

We supposed here that $I(\delta)$ is even. The real normalized spectrum $S(\sigma)$ is then given by

$$S(\sigma) = \frac{B'(\sigma)}{B_W(\sigma)}, \tag{3.5}$$

where B_W is the white reference spectrum. The spectrum as a function of the wavelength $S(\lambda)$ can be recovered with the help of a calibration table (or function) that relates the spatial frequency of the interference pattern to the corresponding wavelength.

3.3 Elements of Fourier transform spectroscopy

Fourier transform spectroscopy has become a wide field since the discovery of the fast Fourier transform (FFT) method by J.W. Cooley and J.W. Turkey in 1965 and the explosive growth of computational power during the past decades. Since this time, the principles of the FT spectroscopy has been extensively discussed in literature [4,5]. So, we will limit us here to introduce briefly some essential concepts that will be applied to our FTS.

3.3.1 Instrumental function

The instrumental function corresponds to the power spectral density that is obtained at the output of the instrument when illuminating with rigorously monochromatic light. This may also be regarded as the impulse response of the (linear) system. It contains any influence of the instrument over the spectrum. The true spectrum of the measured sample $B(\sigma)$ and the spectrum $B'(\sigma)$ obtained by the spectrometer are related by the convolution

$$B'(\sigma) = B(\sigma) \circ h(\sigma), \tag{3.6}$$

with the spectral impulse response $h(\sigma)$ of the instrument (spectrometer). With the convolution theorem, we can rewrite this equation in the spatial domain as

$$I(\delta) = H(\delta) \cdot F(\delta), \tag{3.7}$$

where $F(\delta) = \mathrm{FT}\{B(\sigma)\}$ is the true interferogram, $H(\delta) = \mathrm{FT}\{h(\sigma)\}$ the transfer function and $I(\delta) = \mathrm{FT}\{B'(\sigma)\}$ the measured interferogram.

Truncation:
$h(\sigma)$ is mainly influenced by the truncation of the interferogram. Actually, the measured interferogram has never an infinite length. It is limited by the path difference range (or maximal path difference δ_{max}) of the spectrometer. For a two-

sided interferogram, this range is defined as - $\delta_{max} \leq \delta \leq \delta_{max}$. If this is the only influence of the instrument (no phase error or distortions), the measured interferogram is given by

$$I(\delta) = \mathrm{rect}(\delta / 2\delta_{max}) \cdot F(\delta), \tag{3.8}$$

which corresponds to the multiplication of the true infinite interferogram $F(\delta)$ with a rectangular function *rect* that is equal to one over the range $-\delta_{max} \leq \delta \leq \delta_{max}$ and zero otherwise. As illustrated in Fig. 3.2a, the impulse response will be in this case the Fourier transform of the rect function, which is a sinc function. So, from Eq. (3.6) we get

$$\begin{aligned} B'(\sigma) &= B(\sigma) \circ \mathrm{sinc}\left(2\delta_{max}(\sigma - \sigma_0)\right) = \\ & B(\sigma) \circ \sin(\pi(\sigma - \sigma_0)2\delta_{max}) / (\pi(\sigma - \sigma_0)2\delta_{max}) \end{aligned} \tag{3.9}$$

So the instrumental response for strictly monochromatic light ($B(\sigma)$ = Dirac peak centred at σ_0) is a sinc function centred at σ_0 with the first zero at $1/(2\delta_{max})$. The resolution of the spectrometer can be defined as the full width at half maximum (FWHM) of the impulse response. As shown by Fig. 3.2b, it is given by the central peak of the sinc function and is equal to $0.6/\delta_{max}$.

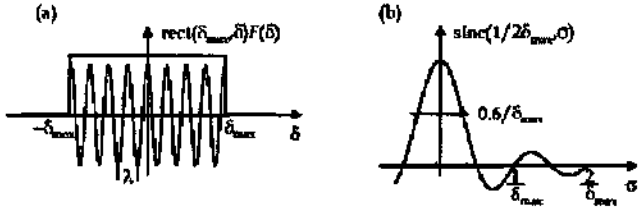

Fig 3.2 : (a) multiplication of the true interferogram with a rectangular function, (b) the true spectrum (Dirac peak) becomes a sinc function (FT(rect)) with a first zero at $1/(2\ \delta_{max})$ and a FWHM of $0.6/\delta_{max}$.

Using $\Delta\sigma = \Delta\lambda/\lambda^2$ we get for the FWHM expressed in wavelength

$$\Delta\lambda_{FWHM} = 0.6\frac{\lambda^2}{\delta_{max}} \approx \frac{\lambda^2}{\delta_{max}}. \tag{3.10}$$

This shows that the resolution decreases with the square of the wavelength. Thus, for the visible spectrum (380 nm to 750 nm) this means that the resolution of the FT spectrometer varies by a factor 4.

Apodization:

Apodization is obtained by the multiplication of a well-defined function $A(\delta)$ with the interferogram. From the convolution theorem, we get

$$I(\delta(y)) = A(\delta) \cdot F(\delta) \overset{FT}{\Rightarrow} B'(\sigma) = \hat{A}(\sigma) \circ B(\sigma), \tag{3.11}$$

which is convolution of the Fourier transform of the apodization function $\hat{A}(\sigma)$ with the spectrum $B(\sigma)$. As seen from Eqs. (3.9) and (3.10), the truncation of the spectrum can also been regarded as an apodization of the interferogram with a rectangular function.

The apodization is used for two different purposes, depending on the type of spectrum:

1) For small-band spectra it reduces the side-lobes (Fig. 3.2b) that are produced by truncation. The smoother the apodization function the better the side-lobes reduction.
2) For smooth broadband spectra it helps to reduce the effects caused by poor signal-to-noise ratio at the borders of the interferogram. The effects on the side-lobes is not relevant here.

Nevertheless, in both cases information is removed from the interferogram and consequently the resolution is reduced. A trade-off between loss of resolution and noise or side-lobe reduction has to be found for each application individually. A list of apodizing functions and their effects is given in [6].

The apodization can be preformed "mathematically" on the measured interferogram. But in some particular configurations where the aperture size is smaller than the spatial extension of the spectrometer and the sample has a Lambert scattering function, we get a predefined intensity distribution for the interferogram and a sort of natural apodization is produced.

Large aperture:

For most of the interferometers, the optical path difference (OPD) depends on the incidence angle of the incoming rays. So, if the source is spatially extended, which is practically always the case, we will have light that experience different OPDs at the output of the interferometer. This phenomenon has already been explained in section 1.3.4. In this section, we define the *field of view* as the maximal angle for which these OPD differences are acceptable. Figure 3.3 illustrates the influence of the angular dependence of the spectrometer. For different incidence angles the light will undergo different OPDs and consequently transforms itself into interferograms with different spatial frequencies. When performing the Fourier transform of the measured interferogram, we get therefore a broader peak than what would be obtained with an instrument which is independent of the angle of incidence.

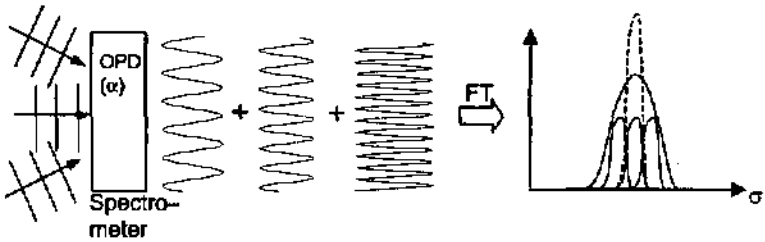

Fig.3.3: Angular dependence of a FT spectrometer. Due to the angular dependent OPD of the spectrometer, light with different incidence angles will induce signals with different spatial frequencies. When performing the FT, these signals become peaks which are slightly shifted with respect to each other. Added up, they give a broader peak (continuous line) as it would be the case for an angle independent spectrometer (dashed line).

We considered here the case of planar waves with different incidence angles (extended source), but we could also consider a non-collimated point source. In this case, we would observe a signal with a phase distortion (or local varying frequency), because the light that contributes to the extremes of the interferogram has a larger incidence angle than at the center. The FT of such a signal gives also a broader (or distorted) peak.
Angle dependence is an important point because it imposes a limit the aperture of the optical system and therefore the throughput. Since the throughput is a main advantage of our FTS-spectrometer compared to grating spectrometers, this is a crucial parameter and has to be discussed in detail.

Phase distortion:
Due to fabrication defects such as nonlinear thickness variations Δt (imperfect cell fabrication or polymer shrinkage) or stress birefringence $\Delta\Delta n$, it is possible that the phase shift (as given by Eq. (3.1)) between the polarization components is not linear anymore and the interferogram will be distorted. The phase shift error $\Delta\delta$ is given by

$$\Delta\delta(\delta,\sigma) = t(\delta)\cdot\Delta\left(\Delta n(\delta,\sigma)\right) + \Delta n(\delta,\sigma)\cdot\Delta t(\delta), \tag{3.12}$$

Where $t(\delta)$ is the local thickness of the prism. The measured interferogram is given by:

$$I(\delta(y)) = F(\delta(y) + \Delta\delta(y)), \tag{3.13}$$

where $F(\delta)$ is the true interferogram and $\Delta\delta(y)$ is the phase error as a function of the position y in the observation plane. When $\Delta\delta(y)$ is known, we can retrieve the true spectrum by modifying the Fourier transform

$$B(\sigma)=\int_0^{\infty}F(\delta)\cos(2\pi\sigma\delta)d\delta=\int_0^{\infty}I(\delta')\cos(2\pi\sigma(\delta'-\Delta\delta))d\delta', \tag{3.14}$$

We made here the variable change: $\delta' = \delta + \Delta\delta$. We suppose that the derivative of $\Delta\delta$ is small so that

$$d\delta'=d\delta\cdot\left(1+\frac{d\Delta\delta(\delta)}{d\delta}\right)\cong d\delta. \tag{3.15}$$

We can note that the phase shift error as defined in Eq. (3.12) is also depends also on the wavenumber σ. We will show later how to measure $\Delta\delta$ and to perform in practice the above described phase correction.

Detector non-linearity:
If the detector response is non-linear, the measured interferogram will be distorted. Every detector (or analogue/digital converter) shows some non-linearity, especially when approaching the saturation level or the detection limit of the detector. However, if detectors with very good linearity, such as high performance CCD are used, the distortions are negligible.

3.3.2 Throughput

In the field of spectroscopy, the throughput (or étendue) expresses the ability of a spectrometer to collect light for a given resolution. It is an important characteristic of a spectrometer, especially when working with low intensity sources or when short integration times are required.
The limiting aperture of the system defines the energy that reaches the detector. It can be the input aperture (source side) or the output aperture (detector side), but practically it is often the detector size that limits the collected energy. So, the spectral throughput

$$G(\lambda)=T(\lambda)\cdot S\cdot\Omega, \tag{3.16}$$

is given here by the detector surface S multiplied by the solid angle Ω of the cone of collected rays (by the detector) and the transmission of the system $T(\lambda)$. Note that for a circular symmetry of the optics we get

$$G(\lambda)=T(\lambda)\cdot S\cdot\pi\cdot\alpha^2, \tag{3.17}$$

where α is the divergence angle of the cone (or field of view angle). Here, we do not take into account parameters such as the spectral sensitivity of detector and the fill factor of the pixels (as in Eq. (3.2)) because they are not relevant for the optimisation of the optical design.

3.3.3 Sampling

For evident reasons, the interferogram is only measured at a finite number of points called sampling points. Of course, by sampling the interferogram information between the sampling points is lost. But if we are interested only in a particular spectral range, which is always the case, we can retrieve by adequate sampling the whole relevant spectrum. The well-known sampling theorem states that the highest frequency ω that can be resolved is given by

$$\omega = \frac{1}{2b}, \tag{3.18}$$

where b is the sampling interval. This means that we need always at least two sampling points to sample the smallest modulation. In our case, the sampling interval is given by the pixel pitch of the detector. So, for a given maximal wavelength λ_{max}, a minimal wavelength λ_{min} and a resolution of $\Delta\lambda$ at λ_{max}, we need at least a maximal path length difference of

$$\delta_{max} = \frac{\lambda_{max}^{\ 2}}{\Delta\lambda}. \tag{3.19}$$

To be able to resolve λ_{min}, we need a minimum number of sampling points or pixels N that is given by:

$$N = 2\frac{\delta_{max}}{\lambda_{min}}. \tag{3.20}$$

If, for instance, we aim a resolution of 10 nm over the visible range from 380 to 730 nm, we need a maximal OPD of $\delta_{max} = 53$ µm. If we suppose that the birefringence Δn is equal to 0.2, this corresponds to a minimal wedge thickness of $D =$ 265 µm ($\delta_{max} = \Delta n \cdot D$). The required number of pixels would be $N = 280$.

3.3.4 Noise

One has to distinguish two categories of noise: the noise due to optical defects or to the sensitivity variations between pixels, which affects directly the measured interferogram (fix pattern noise) and the statistical noises, which includes the noise due to the detection system and the photon noise.
We distinguish between two types of noise: the additive noise and the multiplicative noise. The first one is independent of the light intensity and is just added to the signal, the second one varies with the signal level.

Additive noise:
As already mentioned, additive noise is independent of the intensity and is mainly related to the detection system. The main sources are:

- Thermal noise (or Johnson noise) due to the thermal agitation of electrons in resistive electrical material of the read-out circuit.
- Dark-current noise: Is due to thermally generated electron-holes pairs in the photodiode. This noise is present even if the detector is not illuminated. The

offset created by the dark-current can easily be measured and subtracted from the original signal. The noise itself is due to the shot-noise of the dark-current and is proportional to the square root of this current.

The FT-spectrometers have the advantage that this type of noise is smaller than in grating spectrometers. This is due to the Felgett or multiplex advantage [7], which says that the SNR for a measurement of M spectral channels (sampling points) may be improved by a factor of $\sqrt{M}$ relative to grating spectrometers.
However, in the visible and NIR region, where the detectors are less sensible to thermal radiation, this advantage is not so significant.

Multiplicative noise:
The multiplicative noise is essentially due to the photon noise that is produced by the statistical arrival of photons. This noise is related to the random nature of the spontaneous emission process and is therefore unavoidable. The fluctuations are proportional to the square root of the number of photons. When the detection is photon-noise limited (photon noise larger than the additive noise), the multiplex advantage is not relevant anymore.

3.4 Design and simulation

There are mainly three parameters that characterize the spectrometer presented in section 3.2:

1. the angular dependence or field of view,
2. the localization of the plane of maximal contrast (see section 1.3.5),
3. the resolution.

The ideal spectrometer should have a large angular acceptance, a high resolution and the plane of maximal contrast localized outside the system to permit miniaturization. Other parameters that are related to the LC material such as birefringence, temperature dependence, scattering losses and absorption losses have also to be taken into account.
Many designs have already been presented in literature [8, 9, 10, 11, 12, 13, 14, 15, 16,17, 18]. All these designs are based on inorganic crystals, such as calcite or quartz except [11]. Some of them present rather compact designs by replacing the imaging optics by a second Wollaston prism [10]. An even more compact design can be obtained by inclining the optical axis of the first prism of the Wollaston [13, 18]. Another design [12], containing a compensation plate and a second Wollaston prism, permits an increased field of view and to keep a relatively compact design. In addition to inorganic crystals, liquid crystals offer the possibility to produce birefringent elements with twisted optical axis. This permits designs with a variety of new configurations. FTS designs with enhanced field of view using twisted LC cells were reported for the first time by Stalder et al. [19]. The LC technology has also the advantage to be less expensive.
Fundamentally, by using two or three cells with various twist and orientation of the optical axis many configurations can be obtained. Figure 3.4 shows the different possibilities when the number of cells is limited to three. For simplicity reasons we limit our investigations to a maximum of two wedge cells.

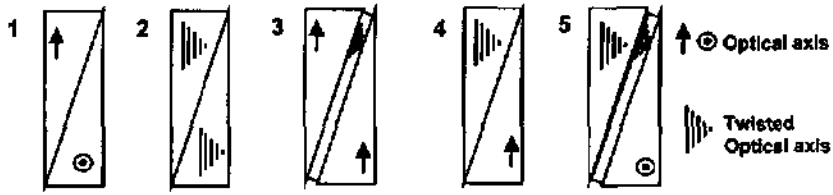

Fig. 3.4: Possible configurations that can be obtained with two or three cells. Other configurations can be obtained by rotating the system by 180° or by choosing various combinations of twist directions.

3.4.1 Resolution

To be able to use the spectrometer in the visible region and for colorimetry, it is required to have a resolution of at least 20 nm [30]. By introducing $\lambda = 700$ nm and $\Delta\lambda = 20$ nm into Eq. (3.19), we find that we need a minimal path difference of $\delta_{max} =$ 24.5 µm. In Tab. 3.1 are listed the maximal phase shifts and corresponding resolution for some LCs that we have used. We considered here a Wollaston with a fixed thickness of $D = 200$µm.

Liquid crystal designation	Birefringence (Δn at 547 nm)	Maximal phase shift (δ_{max}) [µm]	Theoretical resolution (Δλ) [nm] at 700 nm
BL006	0.28	56	9
E7	0.22	44	11
ZLI-1132	0.14	28	18
Wacker (LCP)	0.19	38	13
RM-257 (LCP)	0.14	28	18

Tab. 3.1: List of the resolutions that can be obtained for different LCs and for a fixed Wollaston thickness of 200 µm.

The number of required sampling points N is given by Eq. (3.20). If we introduce the values $\lambda_{min} = 400$ nm and $\delta_{max} = 34$ µm, we obtain $N = 170$ pixels. So we need a linear detector with at least 170 pixels which is not a large number. If we consider a "high resolution" version with the highest birefringence ($\Delta n = 0.3$) and the largest thickness ($D = 300$µm) obtainable with the LC technology, we get a maximal resolution of 6 nm at 700nm and we need 450 pixels. This can be considered as a low resolution spectrometer when compared to laboratory FTS. However, it may be sufficient for applications that need only a modest resolution, such as colorimetry for example. Note that the resolution decreases with the square of the wavelength, this means that in the near infrared region we have only a resolution of about 60 nm (at 1.5 µm).

3.4.2 Field of view and throughput

As explained in section 1.3.4, the field of view gives the angular range over which the OPD variations are acceptable. When measuring a low intensity sources or using short integration times, it is preferable to have a spectrometer with a high throughput (or étendue) and so a large field of view.
A detailed investigation including simulations and measurements of the field of view of configurations 1, 2, 3 in Fig. 3.4. is presented in the article [20] that can be found in Annex 1. In this article, it is shown that the configurations 2 and 3 have a reduced angular dependence compared to the classical configuration 1. They are almost angular independent for zero OPD, but show increasing angular dependence for higher OPDs. These configurations contain twisted structures and can therefore only be fabricated with LC technology. Unfortunately, the plane of maximal contrast of these configurations is localized inside the system and they cannot be miniaturized. As we will see in the next section, by tilting the optical axis, the plane can be pulled out of the system. This can be achieved for configuration 3. For configuration 2, we did not find a way to extract the plane of maximal contrast.
Table 3.2 givea the field of view and the corresponding throughput as defined in Eq .(3.16) for the different configurations. For the calculation of the throughput, we considered a Hamamatsu detector (S5463-512Q) that has a total size of 6.4 mm^2. The transmission coefficient T is given by the transmission of the optical elements (60% at 630 nm) multiplied by the transmission of the two polarizers (25%), which gives a total transmission of about 15%.

Configuration	Field of view	Throughput [mm^2 sr]
1	±10°	0.36
2 (same twist direction)	>±35°	4.3
3	>±35°	4.3

Tab. 3.2: Field of view and throughput of the different configurations.

When tilting the optical axis the rays follow different paths and we may expect the field of view to be altered. We simulated with ASAP [21] for a realistic design (Δn = 0.2, D = 200 µm, ϕ = 0.54°) the modification of field of view when changing the tilt angle of the optical axis. Fig. 3.5b shows the field of view of configuration 1 for a tilt angle of 0° and Fig. 3.5a for a tilt angle of 8° of the first wedge. Such angles are typical pretilt angle for LCD display technology. We see that the field of view stays almost unaltered by tilting the optical axis of the first wedge. Figure 3.5c shows the field of view that is obtained by tilting the optical axis of the second wedge by 2° (and 0° in the first wedge). Here, we see that the interference pattern is shifted towards the right, which indicates that the angular dependence is asymmetric in the direction perpendicular to the linear detector. Simulations showed similar behavior for configuration 4.

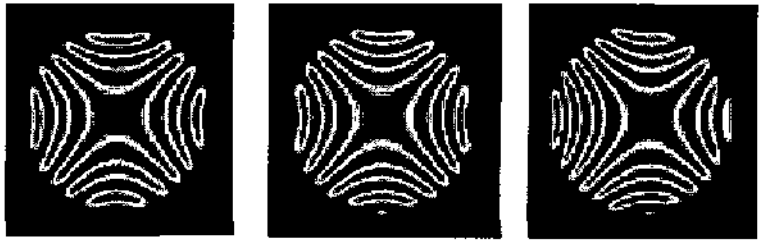

Fig. 3.5: Field of view in the plane of maximal contrast of a classical Wollaston prism with tilted optical axis, (a) 8° tilt for the first prism and 0° for the second, (b) 0° for both prism, (c) 0° for the first and 2° for the second.

So, only tilt angles that are perpendicular to the axis of detector seem to alter the field of view in the plane of maximal contrast. Fortunately, as we will see in the next section, only tilt angles parallel to the detector axis are needed to extract the fringes out of the system.

3.4.3 Plane of maximal contrast

For miniaturization, one important aspect is the localization of the plane of maximal contrast. If this plane is localized inside the system, additional optics is needed to image it onto the detector. This makes the system bulky and it needs additional alignment. Also, the imaging optic may introduce some unwanted distortions.
By tilting adequately the optical axis the plane of maximal contrast can be pulled out of the system. This is illustrated for the classical configuration in Fig. 3.6. In the first variant, the LC molecules (and so the optical axis) are parallel to the surface; the plane of maximal contrast is localized inside the system where the two rays (corresponding to the two polarization components) intersect virtually (see section 1.3.5). In the second variant, the molecules are tilted and the plane is situated outside the system.

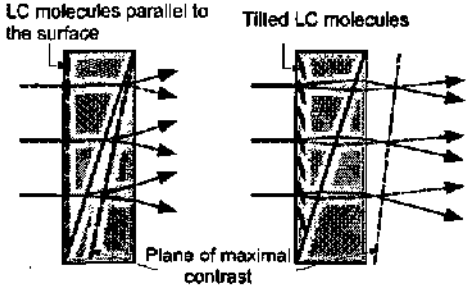

Fig. 3.6: Localization of the plane of maximal contrast for the classical Wollaston configuration. On the left, the LC molecules are parallel to the surface and the plane is localized inside the system. On the right, the LC molecules are tilted and the plane is localized outside the system.

The localization of the plane can be found analytically by geometrical considerations for the classical configurations [18]. For the configuration containing twisted structures, simulations that are based on ray tracing become necessary. For the simulations, we used the same ray trace program (*ASAP*) as for the field of view calculations presented in the previous section. This program is able to split the light in an ordinary and extraordinary ray when entering a uniaxial medium and so to track modification of the polarization state. Moreover, each ray (constituted of several elementary rays) models a Gaussian beam (including phase shift tracking) of a certain spatial extension [22, 23]. A quasi plane wave (limited in space) can be modeled by a superposition of such beams. So, coherent propagation and polarization effects can be treated with this program, which is absolutely necessary for simulation of polarization interferometer properties. Figure 3.7 illustrates the ray trace trough a spectrometer illuminated with an extended source having two wavelengths (632nm and 800nm). The simulation gives the output interferogram and its Fourier transform containing the two peaks corresponding to the two wavelengths.

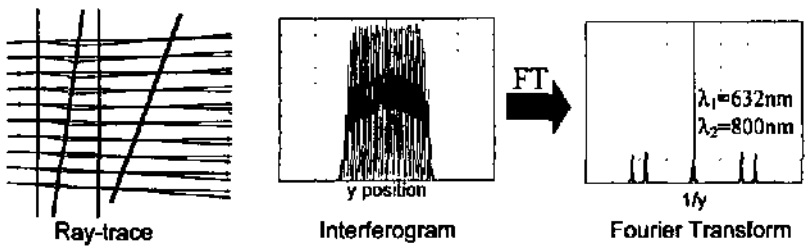

Fig. 3.7: Polarization ray trace through the spectrometer with the resulting interferogram and its Fourier transform.

Three different methods can be used to localize the plane of maximal contrast of the simulated system:

1) The system is illuminated with a spatially extended light source and the points of intersection of two rays that represent the two polarization components give the localization of the plane (as shown in Fig. 3.6).
2) An extended coherent source is focused iteratively in successive points (in the z direction) producing different interference patterns in the far field. The focus point that gives the interference pattern with the largest field of view lies in the plane of maximal contrast.
3) The system is illuminated with a monochromatic spatially incoherent source and the detector is iteratively placed at different locations. The location for which the observed fringes have the maximal contrast correspond to the plane of interest. Figure 3.8 shows an example where the detector has been placed at three different positions. These simulations show that the plane of maximal contrast is situated here at 1.5 mm.

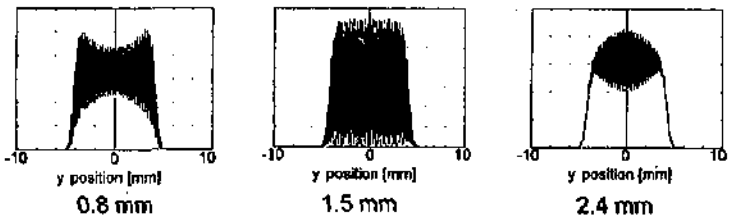

Fig. 3.8: Simulated interferograms for different localizations from the exit surface.

For simplicity we modeled the planar TN cells (as for example in configuration B shown Fig. 3.9) with a simple polarization rotator of 90° (Jones matrix of Eq. (1.13)) and we neglect the additional phase shift introduced by this cell. This approximation can be done when the TN cell is thin (<20 μm) compared with the thick wedge cells (200 μm) and produce, in the case of configuration B, only a slight shift of the zero OPD. In this particular situation, the first method can still be used to determine the plane of maximal contrast.

However, for systems containing thick twisted cells, such as in configuration 2 shown Fig. 3.4, we must calculate precisely the angle dependent phase retardation of the two polarization components. The calculation of the transmission of twisted cells is usually done with Jones matrices (section 1.2.3 and 1.2.4) or by Berreman's method. Unfortunately, these methods can hardly be implemented in ray tracing programs like ASAP. For this reason, we developed two new calculation methods that have been implemented in ASAP. We give here only a brief summary of these methods; a detailed description and the obtained results can be found in the article [24] enclosed in Annex 2. In the first method, called the multiple ray splitting method, the TN cell is divided in N layers with a homogenous uniaxial medium. At each layer interface every incoming ray is divided in a new ordinary and extraordinary ray and is propagated further. At the output of the cell we end up with 2^N rays. The drawback of this method is the high number of rays that are produced when having many layers. In the second method, called the one splitting ray method, the TN cell is divided in N layers of homogenous uniaxial plates combined with a polarizator rotator (Jones matrix in Eq. (1.13)). The rotator rotates the polarization state by an amount equal to the angle between the optical axis of the previous and the next layer. The ordinary and extraordinary rays have not to be split as in the first method, because their corresponding polarization directions are respectively parallel and perpendicular to the optical axis of the next layer and can be traced further. Finally, we end up with much less rays than in the first method and the simulation is faster. Note that this method is very similar to the extended Jones calculation method presented in section 1.2.4.

It has been found that both methods give fairly accurate results for the simulation of our Wollaston prisms [24] (Annex 2). However, the incoming light (or rays) has to be limited to maximal incidence angle of ±35°, because of the paraxial limitations of the Gaussian beam ray tracing.

We studied the localization of the plane of maximal contrast for the three different configurations described in Fig. 3.9.

The maximum tilt angle α is given by the technology constraints. The alignment of the liquid crystal is the same for all the configurations and $\alpha \approx 7°$. For the simulations,

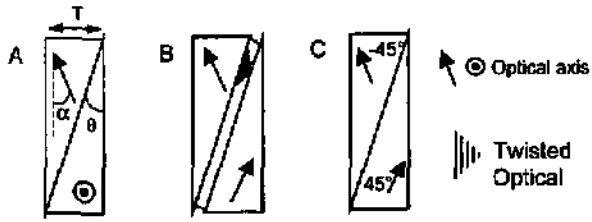

Fig.3.9: Configurations with tilted optical axis that show different localizations of the plane of maximal contrast. (A) Classical modified Wollaston (or Normarski) prism with the optical axis of the first prism tilted by an angle α. (B) Two wedges with opposite tilted axis and a TN cell in between. (C) The Optical axis of both wedges are oriented by ±45° in respect of the detector direction and have opposite tilts.

we used T =230 µm, ϕ = 0.6° and Δn = 0.2 (n_o = 1.51 and n_e = 1.71) which correspond approximately to the parameters of the fabricated systems. To determine theoretically the localization of the plane of maximal contrast, we used the first method of intersecting rays as described above. The measured values have been obtained by directly observing the localization of the fringes in a polarization microscope. The results are summarized in Tab. 3.2.

Configuration	A	B	C
Simulated values Localization of fringes	1.0mm	2.4mm	1.7mm
Measured values	1.2±0.2mm	2.2±0.2mm	-

Tab. 3.2: Measured and simulated position the fringes for the different configurations.

There is a good agreement between measured and simulated values. The most sensible parameter is the pretilt angle (or the tilt angle of the optical axis). A variation of one degree can shift the localization of the fringes by a few hundred microns. Since we could estimate the pretilt angle of the fabricated cells only within a precision of ±1°, the obtained differences are understandable.
From the results above, we see that the position of maximal contrast of the interference fringes varies strongly with the configuration. The maximum distance from the exit face of the system that can be obtained is 2.2 mm. These distances depend of course also on the refractive index and the wedge angle of the system.
For miniaturization, we need at least a distance of 0.5 mm from the exit face (imposed by the bonding of the electrical contacts of the detector) to be able to place the detector exactly where the fringes are localized. In our case, due to the packaging of the detector, a distance of more than 1.3 mm was necessary. This distance can obviously be attained with the present configurations.

3.4.4 Summary of the different system designs

For the complele design of the system, we have to take into account the topics discussed in three previous sections: resolution, field of view and localization of the plane of maximal contrast. Another important element for the design that is not considered here is the detector (size, number of pixels). But since we suppose here that all the configurations have the same dimensions and birefringence, they need also the same detector. So, this element is not relevant for our discussion.
In order to get an overview of the different possible system configurations, we summarize their main performance in Tab.3.3.

Configuration	Design	Nb. of cells	Theoretical resolution at 700 nm [nm]	Loc. of the fringes from the exit surface [mm]	Field of view at zero OPD
A		2	14	1.2	±10°
B		3	14	2.2	>±35°
C		2	14	1.7	±10°
D		2	14	Inside the system	>±35°

Tab. 3.3: Overview of the different configurations and their charteristics.

A high performance system should have a large field of view for a large separation of the plane of maximal contrast to the exit surface. We see that the configuration B is the best one. However, it is also the most complex because of the additional TN cell. For applications where the throughput of the system is not so important, configurations A and C may be interesting variants. Configuration D has only two cells and has a good field of view but since fringes are located inside the system it needs undesired imaging optics.

3.5 Noise reduction and signal processing

The fabricated spectrometers show always defects and are never perfect. There are many sources of defects: dust particles, stress birefringence, wedge deformations, LC impurities, polarizers imperfections, nonlinearity of the detector, scratches, etc., An exhaustive list for FTS spectrometers can be found in [25]. These error sources are often constant over time and are part of the instrumental response. In this case, they can be measured and corrected. In this section we will present several methods to perform such corrections.

3.5.1 Wavelength calibration

To each wavelength of the incoming light λ corresponds a sinusoidal intensity distribution with a certain spatial frequency $p = 1/\Lambda$ at the output of the spectrometer. The relation of the output frequency as a function of the wavelength is not straight forward because it depends on the dispersion relation of the birefringent material. From Eq. (3.1) we get

$$\Lambda = \frac{\lambda}{2\Delta n(\lambda,T)\tan\phi}, \tag{3.21}$$

where ϕ is the wedge angle of the Wollaston prism and $\Delta n(\lambda,T)$ is the birefringence of the LC which depends on the wavelength λ and the temperature T. In most circumstances, $\Lambda(\lambda,\phi,\Delta n,T)$ cannot be calculated in a simple way. It is much easier to measure it precisely and to calibrate the system.
To perform this wavelength calibration we used the set-up as shown in Fig. 3.10. It consists of a monochromator with a bandwidth of 5 nm that illuminates a diffuser placed in front of the spectrometer. This diffuser is necessary for spread the light in order to illuminate the whole Wollaston prism. We obtain so inside the housing a similar illumination as for a reflection measurement.

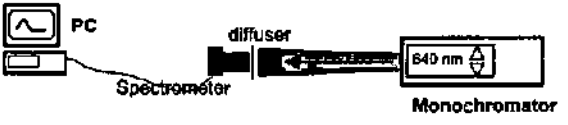

Fig. 3.10: Set up for the wavelength calibration of the spectrometer

The measurements were performed every 10 nm from 400 nm to 750 nm. The peak position of the Fourier transform of the measurement gives p. The following graph shows p as a function of λ for the polymerized LC-silicone (Wacker) prototype at room temperature.

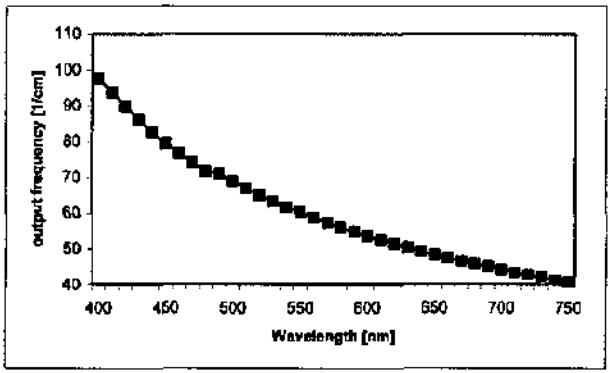

Fig. 3.11: Wavelength calibration measurement.

From this measurement and the wedge angle ($\phi = 0.5°$) we can deduce the dispersion curve of the birefringence by applying Eq. (3.21). The results are shown in Fig. 3.12.

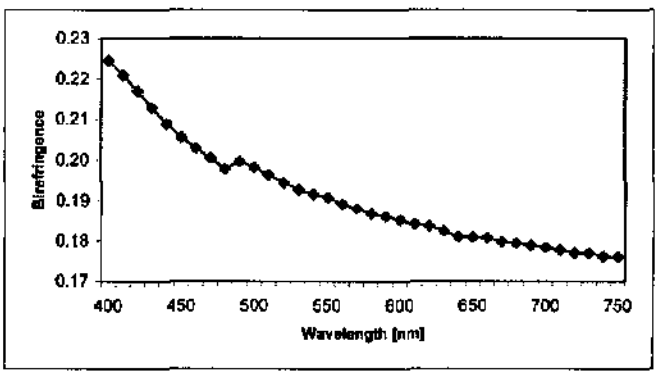

Fig. 3.12: dispersion curve of the birefringence of the LC-Silicone.

The displacement of the curve at 480 nm can be due to a small rotation of the spectrometer during the experiment. A complete calibration curve is obtained by linear interpolation between the measured points. With help of this curve, the real spectrum can be retrieved from the Fourier transform of the output interferogram. For absolute measurements, a rescaling of the spectral intensity due a change of variables should be taken into account. By derivation of Eq. (3.21) we obtain

$$\frac{\lambda^2}{2 \cdot \Delta n(\lambda, T) \cdot \tan\phi} \cdot dp = d\lambda \,, \tag{3.22}$$

So, when performing the variable change from p to λ the intensity should be multiplied by a rescaling factor given by the equation above. However, this factor is not relevant when making relative spectral measurements.

3.5.2 Phase correction

As already mentioned in section 3.3.1, fabrication errors such as thickness variations or stress birefringence cause undesired phase distortions, which are described by Eq. (3.12).
We present here a method already used by Manzardo [26], which permits to determine phase distortions and to correct the measured interferogram.
If we suppose that the phase distortion $\Delta\delta$ is only (or mainly) due to a thickness variation Δt, we have only the first term

$$\Delta\delta = \Delta n \cdot \Delta t\,, \tag{3.23}$$

of Eq. (3.12). As shown in Fig. 3.13 for a simple birefringent wedge, the thickness variation Δt in the z direction can be translated into a shift Δy in the y direction.
In this case the phase error can be written as

Fig. 3.13: deformation of a wedge shaped cell. The thickness variation can be transposed into a shift of the interferogram in the y direction.

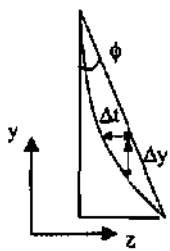

In this case the phase error can be written as

$$\Delta\delta(y) = \frac{2\pi}{\lambda}\Delta y(y)\Delta n(\lambda)\tan\phi\,. \tag{3.24}$$

The corresponding y shifts are given by

$$\Delta y(y) = \frac{\lambda}{2\pi}\frac{\Delta\delta(y)}{\Delta n(\lambda)\tan\phi}\,. \tag{3.25}$$

When introducing this phase error in a perfect interferogram given by

$$I(y) = \sum_j a_j(\lambda_j)\exp\left(i\frac{2\pi}{\lambda_j}\cdot y\Delta n(\lambda_j)\tan\phi\right) \tag{3.26}$$

we obtain

$$I'(y) = \sum_j a_j(\lambda_j) exp\left(i\frac{2\pi}{\lambda_j} \cdot \left(y\Delta n(\lambda_j) tan\phi + \Delta y \Delta n(\lambda_j) tan\phi \right) \right). \tag{3.27}$$

This equation can be rewritten as

$$I'(y) = \sum_j a_j(\lambda_j) exp\left(i\frac{2\pi}{\lambda_j} \Delta n(\lambda_j) tan\phi (y + \Delta y) \right). \tag{3.28}$$

With the help of Eq. (3.21), we can re-express Eq. (3.28) in terms of spatial frequencies

$$I'(y) = \sum_j a_j(k_j) exp\left(i2\pi p_j (y + \Delta y) \right). \tag{3.29}$$

Note here that Δy is independent of the wavelength. We can apply now the Fourier transform

$$B(p_i) = \sum_{p_i} \sum_{y_i} a_j(p_j) exp\left(i2\pi p_j (y_i + \Delta y_i) \right) \cdot exp\left(i2\pi p_i (y_i + \Delta y_i) \right), \tag{3.30}$$

including the rescaling of the y axis $\Delta y(y)$ as described in Eq. (3.25), where $B(p_i)$ are the Fourier components of the undistorted interferogram as a function of the spatial frequencies p_i. By applying the wavelength calibration as described in section 3.5.1, the corrected spectrum as a function of wavelength $B(\lambda_i)$ can be found.
Note that the phase correction can also be performed by simply re-sampling the interferogram, $I'(y_i) \rightarrow I'(y_i - \Delta y_i)$, and then applying the normal Fourier transform.
$\Delta y(y)$ can be found by comparing the measured and the ideal interferogram produced by a monochromatic light source. The ideal interferogram is a perfect theoretical sinusoidal signal with equidistant zeros. The measured interferogram will show some deviations from this perfect signal. The difference between the ideal zero positions and real zero positions gives the values of $\Delta y(y)$ for the zero points of the interferogram. The measured interferogram is obtained by illuminating the spectrometer with diffused monochromatic light as shown in Fig. 3.10.
The effects of the correction are particularly spectacular when it is applied to narrow band spectra. Figure 3.14c shows the spectra obtained from the interferogram shown in Fig. 3.14b. The dotted line shows the uncorrected spectrum and the solid line represents the spectrum obtained from the same interferogram but corrected with the method described above. The phase correction function Δy is shown in Fig. 3.14a. Since this correction is wavelength independent (if we suppose that only thickness variations cause the phase distortion), we can apply the same correction Δy to all wavelengths.

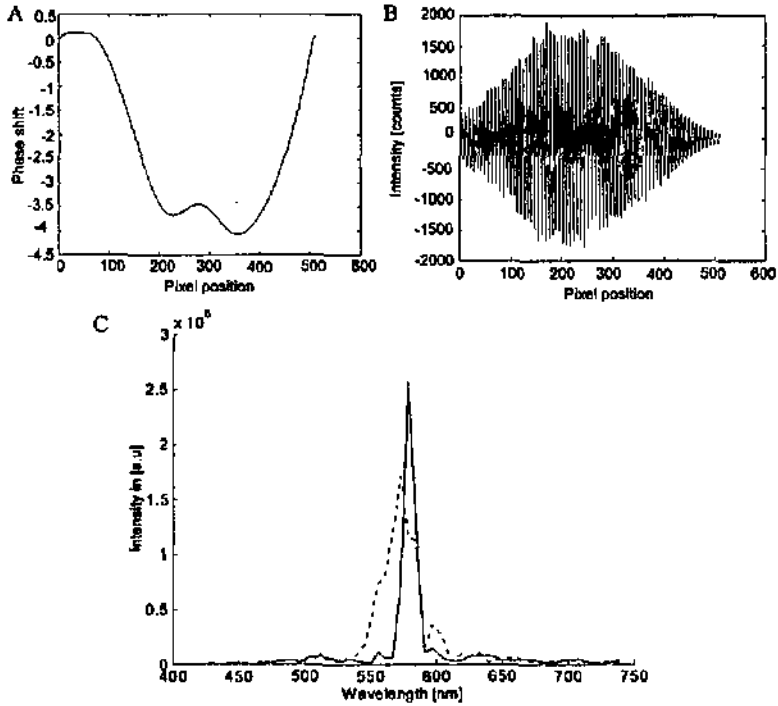

Fig. 3.14: (a) Phase correction applied to each pixel of the interferogram. (b) Uncorrected interferogram obtained with monochromatic light at 570 nm. (c) Uncorrected (dotted) and phase corrected spectrum (solid) of monochromatic light at 570 nm.

Here, the corrected spectrum (solid line) still shows some significant "stray light" (about 1-2 %). This is mainly due to distortions caused by local defects in the LC wedges. The correction of these defects is discussed in the next section.

3.5.3 Fix-pattern noise correction

The interferogram and its Fourier transform are very sensitive to what is called here "fix-pattern noise" (which should not be confused with the noise caused by the detection). This noise is mainly caused by local defects. These defects can be impurities or trapped air bubbles that are present in the LC material, inhomogeneities of certain sheet polarizers, dust particles or scratches present on the substrates surfaces.

In order to suppress this fix-pattern noise, we apply a method already used by Hashimoto [27]. In this method a first interferogram. I_1 is recorded where the polarizer and analyser are oriented perpendicularly as shown in Fig. 3.15 A. Then, a second interferogram I_2 is recorded where the polarization axis of the polarizer and the analyzer are now parallel as shown in Fig. 3.15 B.

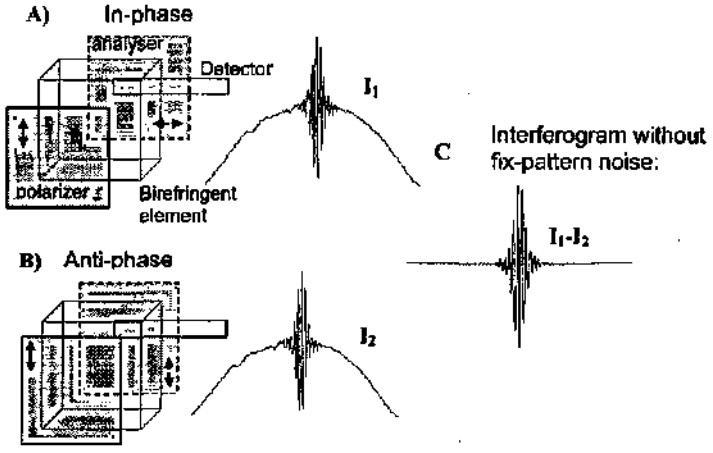

Fig.3.15: Background and fix-pattern noise suppression. (A) Interferogram with crossed polarizers (anti-phase). (B) Interferogram with parallel polarizers (in-phase). (C) Fix-pattern suppression by subtraction of interferogram I_1 with I_2.

When subtracting the in-phase and the anti-phase interferograms (I_1 and I_2), the fix-pattern (mean intensity) called P is suppressed and the signal S (or interference pattern) is doubled. We can write this as

$$I = I_1 - I_2 = (S + P) - (-S + P) = 2S\,. \tag{3.31}$$

Finally we end up with an interferogram where the fix-pattern noise has disappeared and the interference signal S is twice as high.
In order to avoid the mechanical rotation of the polarizer as in the method described by Hashimoto, we introduce a twisted nematic liquid crystal cell (TN cell) in the setup [28]. A properly designed cell rotates the entrance polarization by 90° when it is in the off-state (no electric field, V = 0) and does not affect the entrance polarization when it is in the on-state (V ≠ 0). The TN cell must be aligned so that the polarization axis of the polarizer is parallel or perpendicular to the director (that indicates the optical axis) at incidence. As shown in Fig. 3.16, by introducing a TN cell after the polarizer, we can switch the orientation of the linear polarization by 90° to obtain the two interferograms shown in Fig. 3.15 A and B.

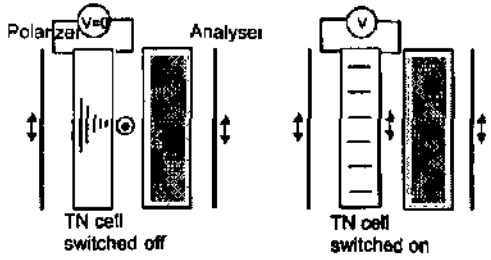

Fig. 3.16: Tracking of the polarization state (arrows) in a system where the TN cell is switched off (left hand) and where the TN cell is switched on (right hand).

In our set-up we did choose a TN cell with a thickness of 23 µm filled with BL006 ($\Delta n = 0.28$). It can be verified that the wave guiding (Maugin) condition [29]

$$\frac{\lambda}{2} << \Delta n \cdot d \,, \tag{3.32}$$

which is necessary for proper guidance of the polarization state and low dispersion in the twisted state, is fulfilled for visible wavelengths ($\Delta nd = 6.44$ µm).
Figure 3.17 shows that this correction procedure reduces significantly the distortions of the spectra. Figures. 3.17a and b show a simple interferogram (gray line) and the same corrected interferogram (black line) and their corresponding spectra. These measurements were obtained by making a reflection measurement of a white reference. Both measurements were phase corrected as described in the previous section. Note that the uncorrected interferogram is here multiplied by two in order to facilitate the comparison.

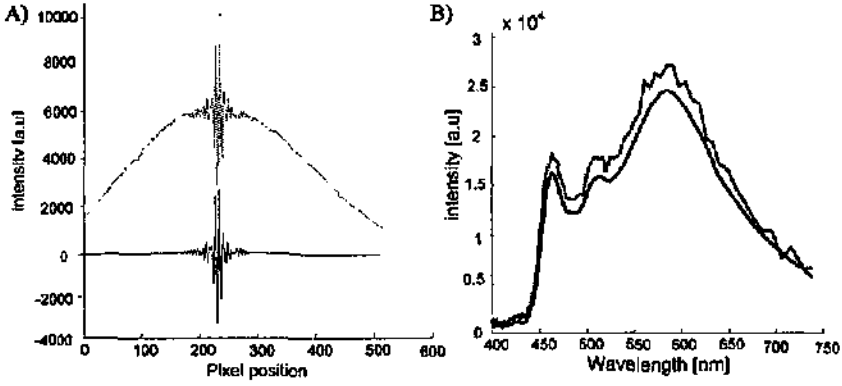

Fig. 3.17: Fix-Pattern and background substraction (A) Comparison of a corrected (black) and uncorrected (gray) white light interferogram and (B) their corresponding spectrums.

It is obvious that the black curve representing the corrected signal gives a smother spectrum than the uncorrected one. Also the tails of the corrected interferogram show less noise. So, this method seems to be very efficient for reducing the fix-pattern noise. However not all the defects can be completely corrected; for example some dust particles may completely obstruct the light on a certain pixel. In this case there is a loss of information and the true interferogram cannot be recovered with any method.

3.5.4 System non-linearity

As mentioned in section 3.3.1, a nonlinear response of the detector distorts the measured spectrum and has consequently to be taken into account.
In principle, the Wollaston transfer function should be perfectly linear. However, we preferred to measure directly the transfer characteristics of the whole system (Wollaston + detector) to avoid any uncertainty. To measure the non-linearity of our system, a constant and well-defined illumination is needed. For this purpose, we used an integration sphere (Labsphere US-120-SF) combined with a LED array (626 nm). A silicon photodiode, which is mounted in the sphere, is connected in close loop with the LEDs and stabilizes the output intensity. We removed the first polarizer in order to avoid interference patterns on the detector. The final set-up is illustrated schematically in Fig. 3.18.

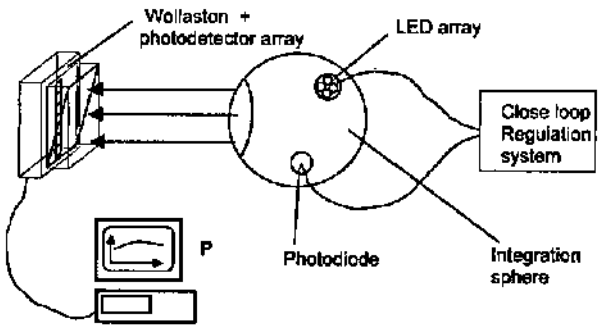

Fig.3.18: Non-linearity measurement setup. The system is illuminated by a homogenous and stabilized illumination system. The detector responses for different illumination intensities are recorded.

For different irradiance values the response of the photo-sensor (Hamamatsu C-MOS linear image sensor, S5463-512Q) was measured with help of the "SpectroSolutions" electronics and the acquisition program described in section 3.7.3.We took the average value over all 512 pixels. The results are reported in Fig. 3.19.

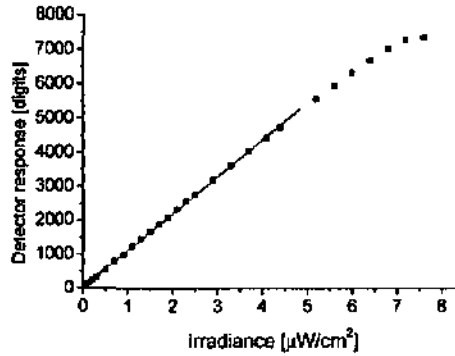

Fig. 3.19: Detector response (in digits) as a function of the incident irradiance. The point indicates the measurements and the curve the linear interpolation for the points between 0 and 5000 digits.

The graph shows that the detector reaches saturation at about 7000 digits. It also demonstrates a good linearity between 0 and 5000 digits. The measured points deviate by less than 30 digits from the linear interpolation. These deviations correspond to approximately to 1-2‰ of average signal. Compared to other error sources, such as distortions due to local defects in the LC (section 3.5.2), the non-linearity of the detector response can be neglected. However, these measurements show that the signal should not exceed 2/3 of the dynamic range of the detector.

3.6 Experimental performance of the spectrometer

In this section we will discuss the experimentally determined optical performance of the developed spectrometer. Other characteristics, such as temperature dependence, has been determined with the hand-held prototype presented in section 3.7. The presented results (for stray light and angle dependence measurements) were obtained by using the setup that is schematically described in Fig. 3.20. The light is produced by a high power xenon lamp or a HeNe laser, which is coupled into a light-guide. A spatially incoherent source is created by illuminating a diffusing plate. Before being analyzed by the spectrometer, the light is limited by an aperture. For the birefringent part of the spectrometer, we used configuration B of Fig. 3.9. The birefringent elements (except the TN cell made of ZLI-1132) were made of silicone LC. In order to perform the fix-pattern noise correction (section 3.5.3), we placed in front of the wedges a switchable 20μm thick TN cell filled with ZLI-1132 having its optical axis oriented at 45° (parallel to the optical axis of the wedges). The whole arregment is sandwiched by two sheet polarizers oriented at ±45°. For detecting the interferogram we placed a 512 pixels Hamamatsu detector array (section 3.7.3) at 1.5 mm behind the last polarizer at the plane of maximal contrast.

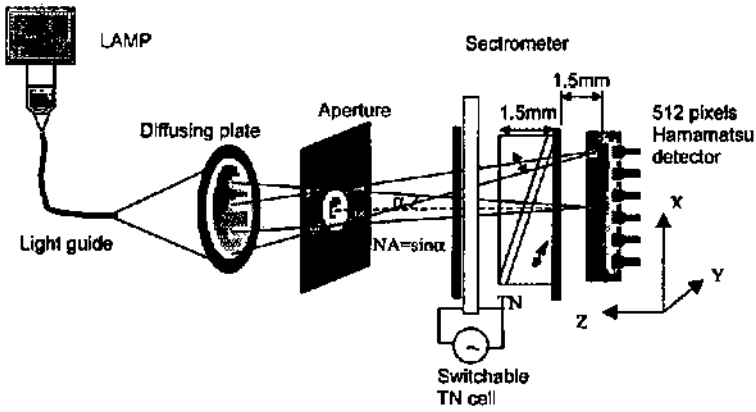

Fig. 3.20: Setup used to characterize the spectrometer. It consists mainly of a light source (xenon lamp or HeNe laser), which illuminates a diffusing plate (Lambertian emitter). The NA of the system is limited by an aperture.

3.6.1 Stray light suppression

We measured the stray light suppression (or noise level) of the spectrometer with two different light sources: a HeNe laser (633 nm) and a xenon lamp combined with a GG495 filter from Schott, which blocks (more than 40 dB) the wavelengths below 495 nm. The measuremnt condition were:

- Single shot measurement or two shots for the fix pattern noise correction.
- Integration time 160 ms.
- Numerical aperture NA = 0.35 corresponding to an angle of ± 20°.
- Phase correction has been performed.
- No "mathematical" apodization.
- Eventual non-linearities of the detector were not corrected.

The results for the HeNe laser are plotted in logarithmic representation in Fig. 3.21. The same graph shows also a comparison of the spectrum obtained with and without fix-pattern correction.

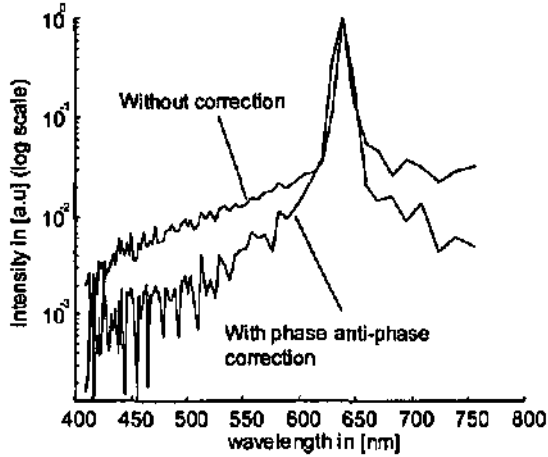

Fig. 3.21: Spectra obtained by illuminating the spectrometer with a HeNe laser. Stray light suppression is significantly increased by using the phase anti-phase correction.

Figure 3.22 shows the stray light suppression (in logarithmic representation) measured by filtering a xenon lamp with a GG495 (Schott glass) filter. The spectrum is normalized by the spectrum measured without the filter.

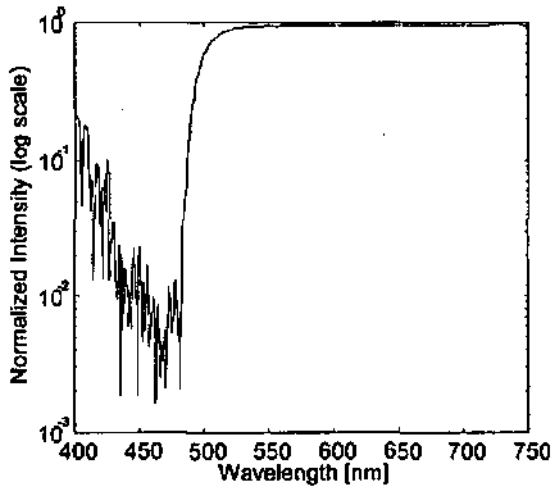

Fig. 3.22: Spectrum obtained by illuminating the spectrometer with a xenon lamp filtered by a GG495 filter.

The stray light suppression between 490 nm and 420 nm is better than 20 dB. Because of the large absorption losses, noise becomes important for wavelengths below 420 nm and we have a stray light suppression of only 10 dB.

3.6.2 Transmission

The total transmission of the system is influenced by the two polarizators and the prisms. Ideally, if we consider unpolarized incoming light, the first polarizer absorbs

50% of the light and the second polarizer absorbs again 50% of the remaining light, which results in a total transmission of 25% (supposing that all the other elements are perfectly transparent). But, as we already have seen in chapter 2, the birefringent elements also absorb about 30% of the light. So, we may expect a total transmission of about 20%. We measured the transmission of the complete system (prisms and polarizers) shown in Fig. 3.23 with a Perkin-Elmer spectrometer. Since we used an integration sphere, the forward-scattered light is also included in the measurements. The slightly higher obtained values around 500 nm and above 700 nm are due to lower selectivity at these wavelengths of the sheet polarizers. It has also to be taken into account that the entrance light was already slightly polarized. This explains that the measured values are a few percent higher than expected.

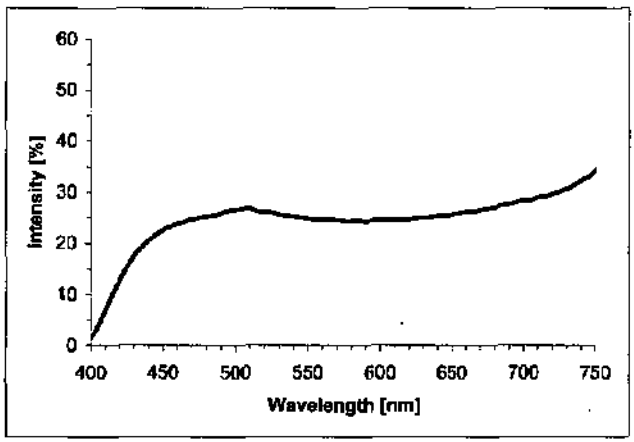

Fig. 3.23: Transmission curve of the spectrometer including the polarizers.

As we see, the transmission decreases drastically below 450 nm. This is not only due to the poor transmission of the LC elements (see chapter 2) but also due to the absorption of the polarizers below 420 nm in this spectral region. The cut-off wavelength is about 400 nm. Figure 3.24 shows the spectrum of a xenon lamp, which can be considered as a "cold white" source, measured with the set-up (NA = 0.35) of Fig. 3.20. Due to the above described absorption, the intensity starts to decrease significantly below 450 nm.

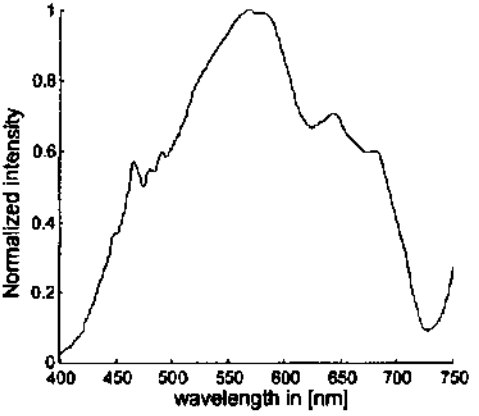

Fig. 3.24: Spectrum obtained by illuminating the spectrometer with a xenon lamp.

For colorimetry for instance, the high absorption losses can be compensated by using an adequate illumination, which has a higher intensity in the blue region.

3.6.3 Resolution

The theoretical resolution of the spectrometer is given by Eq. (3.10). By introducing $\lambda = 633\text{nm}$, $\Delta n = 0.19$ and $D = 200\mu\text{m}$ we obtain a theoretical resolution of $\Delta\lambda = 10\text{nm}$. We measured the resolution by fully illuminating the spectrometer with the setup described in Fig. 3.20. The result is shown in Fig. 3.25. It shows a FWHM of 11 nm, which is very close to the expected value.

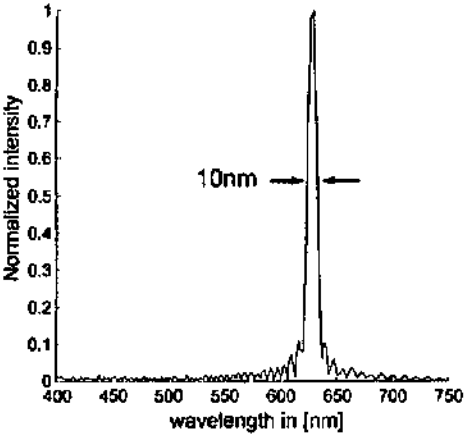

Fig. 3.25: Spectrum obtained by full aperture illumination with a HeNe laser. The measured FWHM is 10 nm.

3.7 Hand-held Prototype for reflection measurements

In this section we will present a hand-held FTS for reflection (and transmission) measurements. As schematically shown in Fig. 3.26, this prototype integrates an illumination module, spectrometer (polarizers and modified Wollaston prism), detector, read-out electronic with data acquisition and processing program. All these elements (except the read-out electronic) were integrated in a compact mechanical construction (measurement head), which is shown in Fig. 3.27.

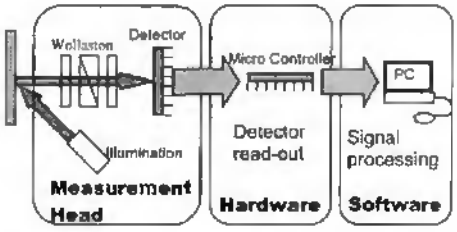

Fig. 3.26: Spectrometer system overview

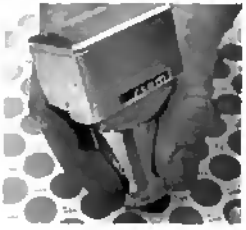

Fig. 3.27: hand-held FTS

Since the prototype is thought to be used mainly for color measurements, we tried to follow as well as possible the ISO recommendations [30].

3.7.1 Spectrometer

To get the optimal spectrometer for the targeted application, there are two important parameters to choose: the design and the LC material. Since we want a compact spectrometer with maximum throughput, the ideal design is given by configuration B (Tab. 3.3). It has a large field of view and the detector can directly be placed at the output of the system. For the LC material we have chosen ZLI-1132 because of its good transmission in the blue region and the reduced scattering (see chapter 2). The drawback of using this material is the low birefringence, which reduces the resolution of the spectrometer and the temperature dependence of the birefringence. Anyway, high resolutions was not the main goal. In a later version of this spectrometer, we used LC polymer materials.

We have built two wedge shaped cells with a 200 µm thick spacer. The glass substrates with side length of 25 mm have a thickness of 0.55 mm. They were coated with polymide layers providing a pretilt of about 6-7° (Nissan SE-610). A TN cell containing also ZLI-1132 was put in between the two wedge cells as shown in Fig. 3.4. A supplementary TN cell was placed in front of the prisms to enable the noise correction described in section 3.5.3. The whole system was sandwiched between two sheet polarizers orientated at ±45°. The detector was placed just behind the last polarizer and the distance from the last glass plate was adjusted to be exactly in the plane of maximal contrast.

The theoretical resolution that can be obtained with such a spectrometer is given by Eq. (3.10). Considering that the detector covers only 60% of the maximal path difference, we obtain a resolution of about 30 nm (FWHM) at 700 nm.

3.7.2 Illumination module

The illumination module is made of a concentric arrangement of eight LEDs; four white and four blue LED's (~440 nm). The blue LEDs were added to compensate the poor performances of the white LEDs in the spectral region below 450 nm. The probe is illuminated via a conical mirror that is inclined by 22.5° to the sample normal in order to obtain the 45° illumination requested for colorimetric measurements [31].
To get a qualitative idea of the illumination spectrum as seen by the spectrometer, we measured it with a commercial spectrometer (Spectrolino, Gretag-Macbeth). The results is shown in Fig. 3.28.

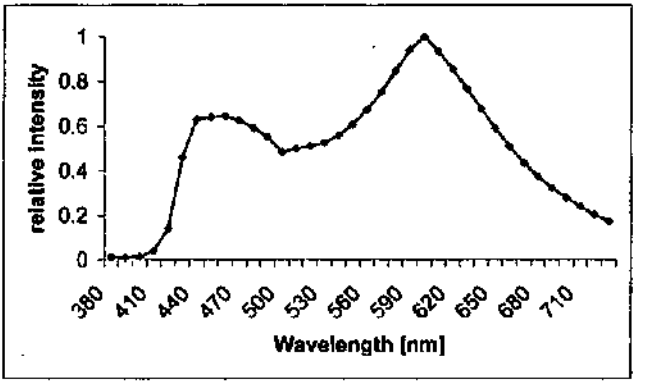

Fig. 3.28: Spectrum of the illumination module.

As seen from the graph above, the spectral region from 380 nm to 430 nm is badly covered by the LEDs. The illumination decreases also above 700 nm.
A more detailed description of this illumination module can be found in [32].

3.7.3 Detector and read-out electronic

For the measurement of the interferogram we used a 512 pixels C-MOS linear image sensor from Hamamatsu (model S5463-512Q). The pixels have a width of 19 µm, a height of 500 µm and the pitch is 25 µm. This detector is chosen mainly for its large pixels and its large saturation achieving a high S/N ratio.
During this work we used two read-out electronics:

1) Electronic provided by Forschungszentrum Karlsruhe with a 16 bits A/D converter (65536 digits) and an RS-232 communication interface. The measured offset was about 500 digits.
2) Electronics provided by Spectrosolutions with a 14 bits A/D converter and a USB communication interface. The measured offset was about 2000 digits.

Additive noise:
We measured the signal coming from the Spectrosolution Board when the detector is not illuminated. We measured a noise of about 3 digits (for an integration time of 80 ms). From the data received from the Hamamatsu supplier, we calculated that about 25000 electrons of the integrated charges are due to the dark current. The dark

current shot noise is thus $\sqrt{25000} = 500$ electrons, which is 10^5 smaller than the saturation charge of $2.5 \cdot 10^7$ electrons. This corresponds to a noise of less than 1 digit. So, the measured noise (of 3 digits) must be due to some other reasons.
Multiplicative noise:
The saturation charge is attained for about $2.5 \cdot 10^7$ photons per pixel. So, we have a shot noise of $\sqrt{2.5 \cdot 10^7} = 5000$. Considering a quantum efficiency near to one, this corresponds for a dynamic range the 10^4 digits to a maximum shot noise of about 2 digit.

3.7.4 Processing and acquisition program

We developed a software tool (called "Color") implemented with Delphi 4.0 to acquire and analyze data coming from the read-out electronics described in the previous section.
The software performs data acquisition via RS232 serial port and USB port, instant spectrum calculation, color coordinate computation, conversion and comparison, automatic calibration generation, and file handling. Several options can be edited to visualize the effects of changes in data processing, such as error correction, white light correction or apodization.
Figure 3.29 shows a screenshot of the main window. A detailed manual, program structure and algorithm description can be found in [33].

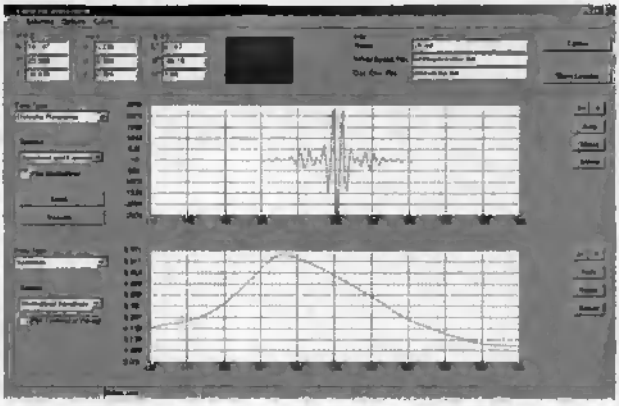

Fig. 3.29: Screenshot of the developed software

3.7.5 Color measurements

We made reflection measurements of uniform colored samples with our prototype and compared them with the spectra obtained with commercially available high performance spectrometer Spectrolino, Gretag-Macbeth). The results are shown in Fig. 3.30.

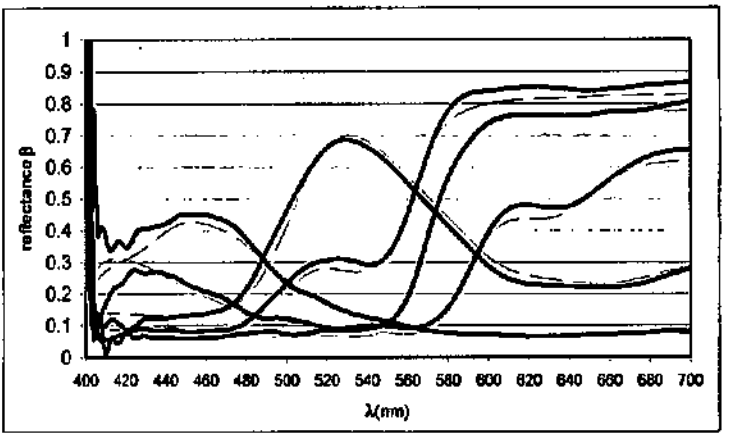

Fig. 3.30: Reflectance measured with the prototype (thick line) and compared with the Spectrolino measurements (thin line)

The difference between our prototype and the Spectrolino measurements reach 5% at some wavelengths. The color distances ΔE (defined in [34]) between them are situated between 1 and 3. These distances are relatively important since the human eye can distinguish distances at least down to 1 and in optimal conditions down to 0.2 [35]. The reasons for these important differences can be various (calibration errors, instrumental distortions, illumination fluctuations...) but the main problem is the large temperature dependence of the prototype, which will be discussed in the next section 3.7. Small changes of the temperature, for example due to the heat produced by the illumination module, shift the spectrum by a few nanometers. Such problems can be avoided by using polymer LCs, which have a much smaller temperature dependence than conventional LCs (section 2.7).
Another drawback of this prototype is the weak intensity of the illumination module in the spectral range below 440 nm. The consequence is clearly demonstrated by the measurements shown in Fig. 3.30.

3.8 Temperature dependence

For applications in uncontrolled environment it is important to have a device that is not sensitive to temperature variations. Unfortunately, the birefringence of LCs is known to be very much temperature dependent (see section 2.1.5) and so our spectrometer is also. From Eq. (3.21) and by considering A as constant, we find for the temperature dependence of the measured wavelength

$$\frac{d\lambda}{dT} = \frac{d\lambda}{d\Delta n}\frac{d\Delta n}{dT} = \frac{\lambda}{\Delta n}\frac{d\Delta n(\lambda,T)}{dT}. \tag{3.33}$$

Since we know that the birefringence is proportional to the order parameter Q, We can approximate [36] the birefringence by:

$$\Delta n = \Delta n_0 S = \Delta n_0 \left(1 - \alpha \frac{T}{T_{N-I}}\right)^{\beta}, \tag{3.34}$$

where T_{N-I} is the nematic-isotrope transition temperature, Δn_0 is the birefringence at $T = 0K$ ($S = 1$), α and β are material parameters. By differentiating Eq. (3.34), we find for the temperature dependence of the birefringence

$$\frac{d\Delta n}{dT} = \Delta n_0 \frac{-\alpha}{T_{N-I}} \beta \left(1 - \alpha \frac{T}{T_{N-I}}\right)^{\beta-1}. \tag{3.35}$$

By replacing Eq. (3.35) into Eq. (3.33), we obtain finally

$$\frac{d\lambda}{dT} = \frac{-\lambda}{\Delta n} \frac{\alpha \Delta n_0}{T_{N-I}} \beta \left(1 - \alpha \frac{T}{T_{N-I}}\right)^{\beta-1}. \tag{3.36}$$

According to [37] we have approximately $\beta = 0.22$ and $\alpha = 0.98$. For ZLI-1132 we have $T_{N-I} = 344$ K. By inserting $\Delta n = 0.14$ at $T = 290$ K into Eq. (3.36) we find $\Delta n_0 = 0.212$. With these values we get from Eq. (3.36) the wavelength drift $|d\lambda/dT|$ around $\lambda = 500$ nm shown in Fig. 3.31.

Fig.3.31: Theoretical temperature dependence of the spectrometer. The graph shows the absolute value of the wavelength drift per degree K that would be observed by the spectrometer (with ZLI-1132) around a certain temperature.

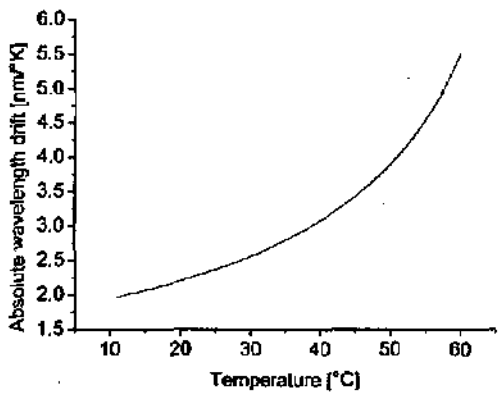

We investigated experimentally two prototypes: a first one made of conventional LC (ZLI-1132) and a second one made of photo-cross-linkable LC polymer (Wacker). To measure the temperature dependence, the FTS prototype was put into a temperature controlled test chamber (Vötsch VT4004). As described in Fig. 3.10, monochromatic light (spectral width of $\Delta\lambda \approx 5$nm) is produced by a monochromator and injected into a plastic wave-guide that is connected to the entrance of the spectrometer. We recorded the localization of the measured peak every 5°C. The results are shown in Fig. 3.32.

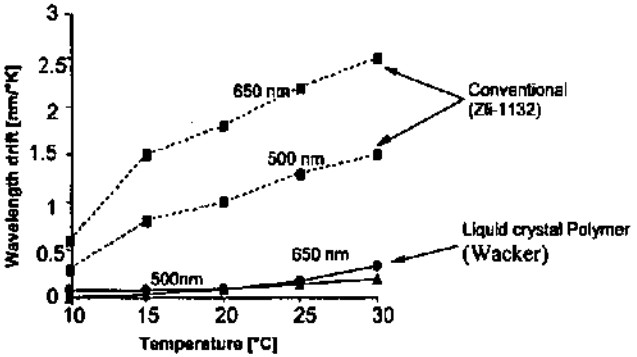

Fig. 3.32: Temperature dependence of a prototype with conventional LC prototype and with LC polymer. The curves indicate the peak drift rate with a measured monochromatic light source (500 nm and 650 nm) at different temperatures.

The wavelength drift rate (around 25°C for 500 nm) can be reduced from 1 nm/°K for conventional LCs to a more acceptable rate of 0.1nm/°K for LC polymers. If we compare these results (ZLI-1132 for 500 nm) with the graph of Fig. 3.31, we see that the theoretical values are about two times higher than the measured values.
Note that if we introduce the temperature dependence of birefringence ($d\Delta n/dT$) measured in section 2.3.3, 2.5.1, 2.5.2 in Eq. (3.33), we obtain similar results to the results of Fig. 3.32. An even better performance may be expected from the LC polymer RM-257 that is practically temperature independent. However a prototype with this material has not been fabricated yet.

3.9 Conclusion

We summarize the actual performance of the prototype hand held FTS spectrometer. The investigated spectrometer that has the configuration shown in Fig. 3.9 B and is made of polymerized LC-silicone (Wacker). We calibrated it as described in section 3.5.1. We performed measurements of pattern noise correction and the phase correction as described in section 3.5.3 and 3.5.2, respectively. The main characteristics of this spectrometer are listed in Tab. 3.4.

Size	25 x 25 x 6 mm^3 (without detector)
Resolution	11 nm (at 630 nm)
Field of view	> 35° (depending on OPD)
Stray light suppression	< 22 dB (for λ > 420 nm)
Average Transmission (VIS)	~15%
Cut-off wavelength	410 nm
Temperature dependence	0.1 nm/°K

Tab. 3.5: Overview of the performances of the investigated spectrometer.

Several characteristics can still be improved in the future:

- The size of the spectrometer can be reduced to the size of the detector.
- Stray light suppression can be enhanced by optimizing the fabrication process of the LC cells.
- Temperature dependence can be reduced by using higher cross-linked LC polymers or by performing post-curing processing steps (see section 2.5.1).

The other characteristics are more intrinsically dependent of the LC technology or of the spectrometer design and can (to the best of our knowledge) hardly be improved.

3.10 References

[1] O. Manzardo, P. Kipfer, andd H. P. Herzig, "Dispersive compact Fourier transform spectrometer fro the visible", in *Fourier Transfrom Spectroscopy: New Methodes and Applications*, pp.165-167, OSA Technical Digest Series, Optical Society of America, Washington, 1999.

[2] O. Manzardo, H. P. Herzig, C. R. Marxer and N. F. de Rooij, "miniaturized time-scanning Fourier transform spectrometer based on silicon technology", *Opt. Lett.* 24, pp. 1705-1707, 1999.

[3] S. D. Collins, R. L. Smith, C. González, K.P. Stewart, J. G. Hagopian, J. M. Sirota, "Fourier-transform optical microsystems", *Opt. Lett.*, 24 (12), 1999.

[4] J. Bell, *Introductory Fourier Transform Spectroscopy*. Academic, New York, 1972.

[5] J. Chamberlin, *The Principle of Interferometric Spectroscopy*. Wiley Interscience, Chichester, 1979.

[6] O. Manzardo, *Micro-Sized Fourier Spectrometers*, p.24. Thesis at university of Neuchâtel, January 2002.

[7] P. B. Felgett, *J. Phys. Radium*, 19, p.187, 1958.

[8] B. H. Billings, "Visual Fourier-Transform spectroscopy with single crystal plate," *Journal of the Optical Society of America* 65 (7), 817-824, 1975.

[9] M. J. Padgett, A. R. Harvey, A. J. Duncan, and W. Sibbett, "Single-Pulse Fourier-transform spectrometer having no moving parts," *Applied Optics* 33 (25), 6035-6040, 1994.

[10] M. J. Padgett and A. R. Harvey, "A static Fourier-transform spectrometer based on Wollaston prisms", *Rev. Sci. Instrum.* 66 (4), pp. 2807-2811, 1995.

[11] T. Inoue, A. Hirai, K. Itoh, and Y. Ichioka, "Compact Spectral Imaging System Using Liquid Crystal for Fast Measurement.," *Optical review* 1, 129-131, 1994.

[12] J. Courtial, B. A. Patterson, A. R. Harvey, W. Sibbett, and M. J. Padgett, "Design of a static Fourier-transform spectrometer with increase field of view," *Applied Optics* 35 (34), 6698-6702, 1996.

[13] B. A. Patterson, M. Antoni, J. Courtial, A. J. Duncan, W. Sibbett, and M. J. Padgett, "An ultra-compact static Fourier-transform spectrometer based on a single birefrigent component" *Optics Communications* 130, 1-6, 1996.

[14] F. J. Dunmore, and L. M. Hanssen, "Miniature Fourier Instrument for Radiation Thermometry," presented at the Fourier Transform Spectroscopy: 11th international Conference 1998 (unpublished).

[15] S. Prunet, B. Journet and G. Fortunato, "Exact calculation of the optical path difference and description of a new birefringent interferometer", *Opt. Eng.* 38 (6), pp. 983-990, 1999.

[16] D. Steers, C. Gerrard, B. Hirst, W. Sibbett and M. J. Padgett "Gasoline analysis and brand identification using static Fourier-transform ultraviolet spectrometer", *J. Opt. A: Pure Appl. Opt.* 1, pp. 680-684, 1999.

[17] D. Steers, W. Sibbett and M.J. Padgett, "Dual-purpose, compact spectrometer and fiber-coupled laser wavemeter based on a wollaston prism", *Applied Optics*, 37 (24), 1998.

[18] C. C. Montarou and T. K. Gaylord, "Analysis and design of modified Wollaston prisms" *Applied Optics* , 33 (31), 6604-6613, 1999.

[19] M. Stalder, P. Seitz, "Wollaston prism and use of it in a Fourier transform spectrometer", European Patent Application, EP 0 939 323 A1, 1998.
[20] G. Boer, T. Scharf and R. Dändliker, "Compact static Fourier transform spectrometer with a large field of view based on liquid-crystal technology", *Applied Optics*, **41** (7), p.1400, 2002.
[21] Breault Research Organization, "Wave optics", ASAP applicatons notes, Tuscon, 2001.
[22] J. Arnaud, "Representation of Gaussian beams by complex rays", *Applied Optics*, **24** (4), p. 538, 1985.
[23] R. Herloski, S. Marshall, and R. Antos, "Gaussian beam ray-equivalent modeling and optical design", *Applied Optics*, 22 (8), p. 1168, 1983.
[24] G. Boer and T. Scharf, "Polarization Ray Trace in Twisted Liquid Crystal Systems", *MCLC*, **375**, pp.301-311, 2002.
[25] J. R. Birch and F. J. J Clark, "Fifty categories of ordinate error in Fourier transform spectroscopy.", *Spectroscopy Europe*, *7*/4, p.p. 16-22, 1995.
[26] O. Manzardo, *Micro-Sized Fourier Spectrometers*, p.73. Thesis at university of Neuchâtel, January 2002.
[27] M. Hashimoto and S. Kawata "Multichannel Fourier-transform infrared spectrometer", *Applied Optics*, **31** (28), p.6096-6101, 1992.
[28] G.Boer, "Polarization interferometer with reduced noise", *European Patent Application*, EP 1 278 050 A1, 1998.
[29] P.J. Collings and M.Hird, *introduction to liquid crystals*, p.236. Taylor & Francis, 1997.
[30] ISO 7724 Paints and varnishes- Colorimetry, 1997
[31] DIN 5033 "Farbmessung", Messbedingungen für Körperfarben, July1983.
[32] G.Boer, R.Dangel, K.Cottier, T. Scharf, and P. Scitz, "Illumination module for a reflection spectrometer", *European Patent Application*, EP 1 278 049 A1, 2003.
[33] K.Cottier, G.Boer, *Color v.3.0, Software description*, CSEM document.
[34] ISO 7724-3, "paints and varnishes- colorimetry- part3: calculations of colour differences by CIELAB", International organization for standardization, 1997.
[35] K. Schläpfer, *Farbmetrik in der Reproduktionstechnik und im Mehrfarbendruck*, , p.68, UGRA, 1993.
[36] I-C. Khoo, S-T. Wu, *optics and nonlinear optics of liquid crystals*, p.208. World Scientific, Singapore, 1993.
[37] W. H. de Jeu, *Physical properties of liquid crystalline materials*, p.11. Gordon and Breach, science Publishers, New York, 1980.

Chapter 4

Other applications

In this chapter we will briefly present two applications based on polarisation interferometers that use liquid crystal birefringent elements. The first application is a common path interferometer based on a birefringent lens for optical surface measurements. The second application is a shearing interferometer based on two Wollaston prisms for phase object observation in differential interference contrast microscopy (DIC microscopy).

4.1 Double focus common-path interferometer

A double focus interferometer is a polarization interferometer that uses a birefringent lens as beam splitter. One beam (reference beam) is focused on a small spot of the surface under test and the second beam (testing beam) is expanded over the whole aperture and is affected by the aberrations of the system. The main advantage of these common-path interferometers is their insensitivity to mechanical vibration and thermal drift. The first double-focus interferometer for testing optical components had been devised by Dyson [1]. Since that time other similar interferometers have been built [2, 3, 4, 5]. One of the principal problems of these systems is the use of an expensive birefringent lens made of inorganic crystal such as calcite. To solve this problem, Nose et al. build an interferometer using a lens made of a conventional liquid crystal [6, 7]. In the present work we have realized such an interferometer and we did investigate the possibility to use the more robust polymer LCs instead of conventional LCs.

4.1.1 Principle of functioning

The principle of functioning of the interferometer is schematically depicted in Fig. 4.1. Monochromatic light produced by a HeNe laser (633nm) is polarized at 45° (by a sheet polarizer), collimated and expanded to a diameter of more than 1 cm (diameter of the LC cell). The so obtained quasi-plane wave I passes through a calibrated LC phase shifter and a beam-splitter before attaining the birefringent LC plano-convex lens. The polarization component perpendicular to the optical axis, which corresponds to the test wavefront T, will experience the ordinary index of the LC that is equal to the refractive index of the surrounding glass. So, it will not be affected until it reaches the test surface. The polarization component parallel to the optical axis, which

corresponds to the reference wavefront R, will experience the extraordinary index. So, it will be focused on a small spot of the test surface (when adequately positioned), so that the beam does not suffer from any appreciable distortion. When reflected from the test surface the two wavefronts travels back through the birefringent lens and the beam-splitter. Ideally, the reference beam should become planar again and the test wavefront should carry the information about the topology of the test surface. The two wavefronts pass finally through a second polarizer oriented at ±45° to permit them to interfere. The interference pattern is recorded with a 12 bits CCD camera (Dalsa CA-D1).

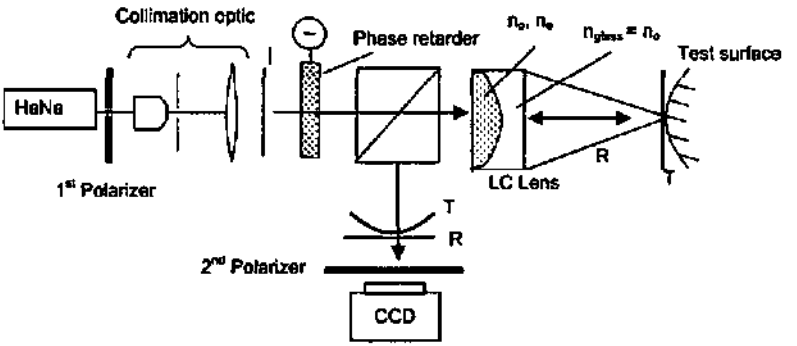

Fig. 4.1: Schematic of the double focus common-path interferometer.

The recorded interference patterns I_{out} are essentially given by Eq. (1.38). We can rewrite this equation in a form which is better adapted to our set-up

$$\begin{aligned} I_{out} &= (T+R)^2 = A_T^2 + A_R^2 + 2A_T A_R \cos(kW(x,y) - \phi) \\ &= I_0(x,y)\{1 + V(x,y)\cos(kW(x,y) - \phi)\} \end{aligned} \tag{4.1}$$

where $kW(x,y)$ is the phase shift produced by the profile of the test surface, $V(x,y)$ the visibility, $I_0(x,y)$ the mean intensity and ϕ a constant phase shift. So, I_{out} contains three unknown functions W, V and I_0. To solve Eq. (4.1), we need at least two more equations. We can obtain these equations by introducing a phase-shift between the two interfering waves with the LC phase retarder. If we use the phases $0, \pi/2, \pi, 3\pi/2$, and substitute these for ϕ in Eq. (4.1), we obtain the four interferograms

$$\begin{aligned} I_{out1} &= A_T^2 + A_R^2 + 2A_T A_R \cos(kW(x,y)), \\ I_{out2} &= A_T^2 + A_R^2 + 2A_T A_R \sin(kW(x,y)), \\ I_{out3} &= A_T^2 + A_R^2 - 2A_T A_R \cos(kW(x,y)), \\ I_{out4} &= A_T^2 + A_R^2 - 2A_T A_R \sin(kW(x,y)). \end{aligned} \tag{4.2}$$

From these equations we can obtain the well-known four-phase algorithm formula

$$kW(x,y) = arctan\left(\frac{I_{out2} - I_{out4}}{I_{out1} - I_{out3}}\right). \tag{4.3}$$

Because of the reflection, W corresponds to twice the deformation of the surface profile. There exist many others variations of this algorithm, having various advantages [8, 9].
When the tested surface varies more than one wavelength (corresponding to 2π phase shift), W will show discontinuities because of the discontinuity of the arctan function. In order to retrieve the real surface profile, we must apply a phase unwrapping method on W. To perform this, we used two different programs: one method is implemented in Matlab and described in [10] and a more sophisticated freeware program (FRAN) [11].

4.1.2 Liquid crystal lens

The LC lenses were realized as described in section 2.2. One of the main difficulties is to index matching between n_o of the LC and the n of the BK7 glass ($n_{BK7} = 1.5167$) of the substrate lens. We must also make sure that the birefringence of the material is large enough in order to get a reasonable focal length. There is a large range of LCs available and the index matching can be done with a certain accuracy. Of course, the LC should also have a large nematic range around room temperature and show good alignment even for thick cells. The table below proposes a collection of three nematic LCs with a birefringence larger than 0.13 and for which the ordinary index is relatively close to the one of the BK7 glass.

Material	n_e	n_o	mismatch
ZLI 1132	1.6280	1.4910	0.026
ZLI 1738	1.7051	1.5168	0.001
ZLI 1289	1.707	1.517	0.003

Tab. 4.1: Refractive indices of different LC materials compared to the refractive index of BK7 glass.

The ideal LC would be ZLI-1738, but we could only make lenses with a good optical quality (no domains and low scattering) with ZLI-1132. The focal length f of the extraordinary polarization component is given by

$$\frac{1}{f} = (n_e - n_{BK7})\frac{1}{r_l}, \tag{4.4}$$

Where r_l is the radius of curvature of the substrate lens and n_{glass} the refractive index of the glass. When introducing the values for ZLI-1132 and $r_l = 24{,}81$ mm into Eq.(4.4), we obtain a focal length of about 0.2 m. The lens has a maximal thickness of 0.62 mm and a diameter of 12 mm. To obtain a shorter focal length, LC with larger birefringence should be used (for $n_e = 1.8$ we would get $f = 0.1$ m). A smaller radius of curvature would also decrease the focal length, but the lens would become too thick for correct alignment of the LC.

Figure 4.2 shows the interference fringes obtained by placing birefringent lenses, one with a conventional LC and the other with a polymerized LC (LCP), between 45° oriented polarizers.

Fig. 4.2: Interference fringes produces by a birefringent lens placed in between polarizers at ±45°. On the left side a lens made of LC-Silicone (Wacker) and on the right side a lens made of standard LC (BL006, Merck).

The noisy and deformed fringes in left picture show clearly that the LCP lens has an insufficient quality for the present application. The poor quality is mainly due to stress birefringence and the presence of little agglomerates present in the LC material. The right pictures shows a regular and clear interference pattern which revcals good optical quality.
The small mismatch between the ordinary index of ZLI-1132 and the BK7 glass makes the T wavefront slightly divergent when illuminated with collimated light. As shown in Fig. 4.3, this can be compensated by introducing an additional converging lens between the test surface and the birefringent lens.

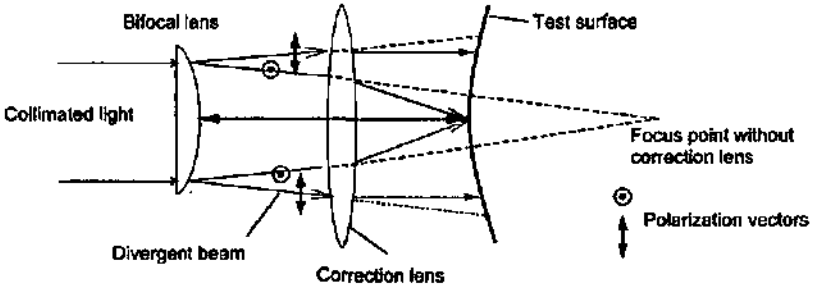

Fig. 4.3:Set-up withg an additional correction lens.

We finally have used an achromatic lens with a focal distance of 1.33 m and positioned it so that the divergence of the ordinary beam is compensated.

4.1.3 Astigmatism of the liquid crystal lens

The LC bifocal lens shows a strong astigmatism, i.e. the extraordinary wavefront (here the reference beam R of Fig. 4.1) that has traversed the LC lens is curved

differently along the x-axis than along the y-axis. As already been studied by Nose [7], this asymmetric effect is due to the alignment of the molecules. Figure 4.4 shows the alignment of the LC molecules that follow the curvature of the lens. In the y-direction, the molecules are all oriented parallel. In the x-direction however the orientation of the molecules changes making an angle θ with the normal to the incoming light. From Eq. (1.7) we know that the extraordinary index change with θ. So, the phase shift between the two polarization components will be different in point A and point B. This will produce an asymmetric phase shift pattern over the lens.

Fig. 4.4: Alignment of the LC molecules in the bifocal lens.

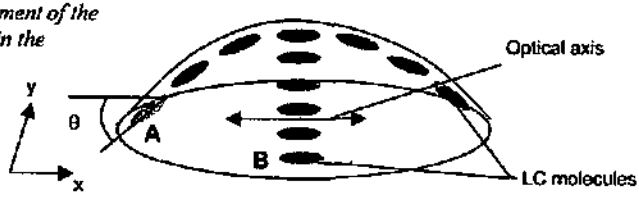

Note that for a lens made of inorganic crystal where the optical axis is oriented homogenously over the whole lens, we would not observe this asymmetry.

We have calculated the astygmatism produced by a plano-convexe LC lens as shown in Fig. 4.4. For this purpose we have calculate the optical path for every x,y coordinate by taking into account the angular distribution of the optical axis and the thickness variation.

Fig. 4.5: Transverse view of a plano-convexe LC lens with the glass substrate

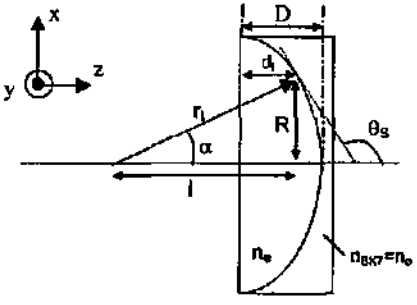

From Fig. 4.5 we can deduce the thickness variation

$$d_l = D-(r_l-l) = D-\left(r_l-\sqrt{r_l^2-R^2}\right), \tag{4.5}$$

of the LC lens, where D and r_l are the maximum thickness and the radius of curvature of the LC lens, respectively. R is the distance between the central axis and the point of

interest. If we consider the reference of the coordinate axes on the central axis, we can introduce $R=\sqrt{x^2+y^2}$ and get

$$d_l(x,y)=D-\left(r_l-\sqrt{r_l^2-x^2-y^2}\right), \tag{4.6}$$

The angular distrubution of the optical axis is given by the alignment of the molecules. Figure 4.6 shows the alignment variation of the molecules in the z direction for the arbitrary coordinates x, y. We divided the lens in infinitesimal cells (dxdydz) where the alignment is considered as being constant.

Fig. 4.6: Angular distribution of the LC alignment along the Z axis.

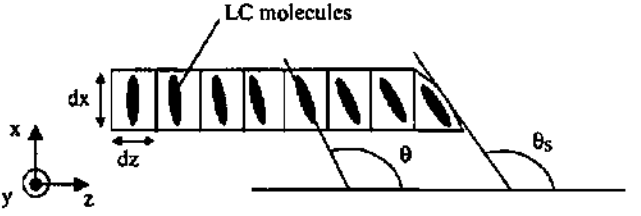

The inclination of the molecules (or optical axis) is given by the angle $\theta(z)$, which varies linearly in the direction of z from $\pi/2$ to θ_S. So,

$$\theta(x,y,z)=\frac{\pi}{2}+\frac{z}{d_l}\cdot\left(\theta_S(x,y)-\frac{\pi}{2}\right), \tag{4.7}$$

Supposing that the pretilt angle is zero, θ_S is equal to the angle made by the tangent to the surface (in the x-z plane) with the z axis. From Fig 4.5 we can deduce

$$\theta_S(x,y)=\arctan\left(\frac{y}{d_l(x,y)-D+r_l}\right)+\frac{\pi}{2}=\arctan\left(\frac{y}{r_l^2-x^2-y^2}\right)+\frac{\pi}{2}. \tag{4.8}$$

By using $\arctan(a/b)=\arcsin\left(a/\sqrt{a^2+b^2}\right)$, we get

$$\theta_S(x,y)=\arcsin\left(y/\sqrt{r_l^2-x^2}\right)+\pi/2. \tag{4.9}$$

The optical path of the extraordinary wave

$$L_{opt}=\int_0^{d_l(x,y)} n_e(\theta)dz+n_{glass}(D-d_l(x,y)). \tag{4.10}$$

is given by the contribution of the LC lens and the lens substrate. By inserting $n_e(\theta)$ from Eq. (1.7), Eq. (4.6) and Eq. (4.7) into Eq. (4.10) we finally get

$$L_{opt} = \int_0^{d_l(x,y)} \left(\frac{1}{n_o^2}\cos^2\left(\frac{\pi}{2}+\frac{z(\theta_s-\pi/2)}{d_l(x,y)}\right)+\frac{1}{n_e^2}\sin^2\left(\frac{\pi}{2}+\frac{z(\theta_s-\pi/2)}{d_l(x,x)}\right)\right)^{-\frac{1}{2}} dz + n_{glass}(D-d_l(x,y)) \quad (4.11)$$

where $d_l(x,y)$ is given by Eq. (4.6) and θ_s by Eq. (4.8). We could determine the focus points of the extraordinary wave by introducing $r_l = 24.81$ mm, $n_o = 1.491$, $n_e = 1.628$, D = 0.62mm, $n_{glass} = n_{BK7}$ in Eq. (4.10) and by solving the integral numerically. We found for the x axis (parallel to the rubbing direction) the focal line at $f_x = 225{,}0$ mm and for the y axis $f_y = 223{,}5$ mm. So, we have an astigmatic difference of $f_x - f_y = 1.5$ mm.

With the help of the set-up of Fig. 4.1 we could determined the astigmatism of the LC lens experimentally. We used as test surface a planar mirror positioned perpendicularly to the propagation direction of the test beam. If the optical system had no aberration and if the mirror was in the focus point of the reference beam than we should obtain a perfectly uniform interference pattern. Instead of this, we obtained the interference pattern shown in Fig. 4.7. The interference patterns of Fig. 4.7b and c where obtained by positioning the test surface at 1 mm and 2 mm, respectively, from the position corresponding to the interference pattern of Fig. 4.7a.

(a) (b) (c)

Fig. 4.7: Interference patterns obtained with a flat mirror positioned at 0 mm (a), at 1 mm (b) and at 2 mm (c).

Interference pattern (a) corresponds to the situation where the extraordinary wave (or reference beam) is perfectly focused along the x-axis but not along the y-axis. Interference pattern (c) corresponds to the inverse situation. Interference pattern (b) corresponds to a configuration where the mirror is placed in between the two focal lines and the intensity varies in both directions. From these measurements, we can deduce that the focal lines corresponding to the x and the y axis are separated by 2 mm (distance between interference pattern (a) and (b)), which is in good agreement with the theoretical value of 1.5 mm obtained by Eq. (4.11).

4.1.4 Electro-optic phase retarder

In order to perform the phase shift needed for the four phases algorithm, we used a 6 µm thick switchable planar nematic LC cell. The phase retardation produced by the

cell varies with the applied voltage. Figure 4.8 shows the principle of the phase retarder. The applied voltage produces an electric field, which tends to align the LC molecules perpendicular to the surface. For 45° polarized light, the phase shift between the two polarization components depends on the tilt angle θ of the optical axis (see Eq. (1.7)).
It will be zero for $\theta = 90°$ and Δnd for $\theta = 0°$. So, the phase shift will vary with the applied voltage.

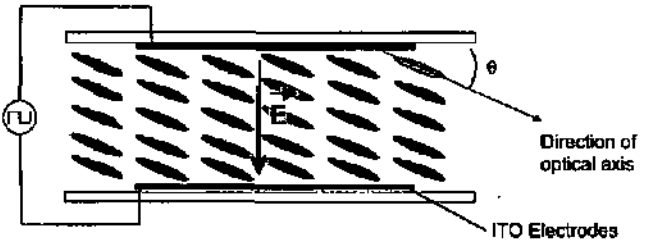

Fig. 4.8: Schematic of an electro-optical phase retarder based on a LC cell. The strength of the applied electric field imposes the tilt of the optical axis and so the phase retardation.

The dependence between of phase retardation and the applied voltage has been determined experimentally. The phase retardation was measured by placing the LC cell in a polarization microscope equipped with a calibrated Leitz 5λ compensator. The results are shown in Fig. 4.9.

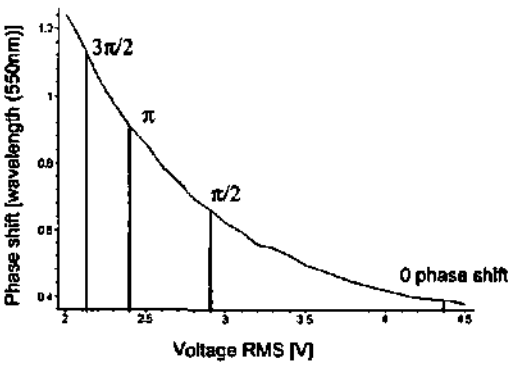

Fig. 4.9: Calibration curve of the phase retardation of the LC cell as a function of the applied voltage.

4.1.5 Experimental results

With the set-up of Fig. 4.1, we measured different reflective test surfaces. Figure 4.10 shows the surface profile obtained for the flat mirror over a surface of about 16 mm^2 (250 x 300 pixels and 1 pixel = 15 μm x 15 μm).

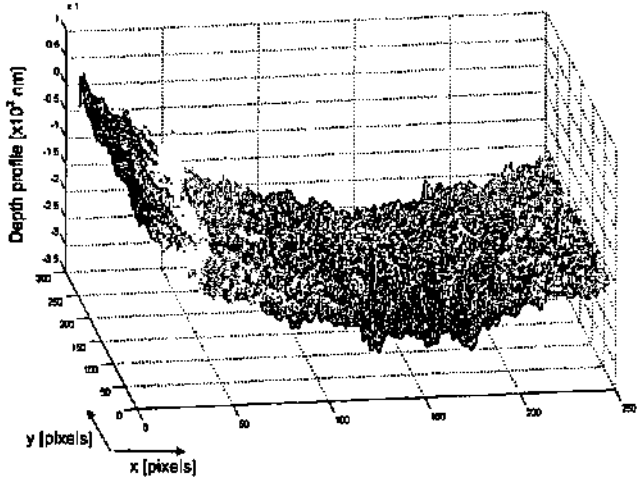

Fig. 4.10: Measured surface profile of a flat mirror. The covered area is about 4mmx4mm.

The measured curvature in the x direction comes from the uncorrected astigmatism of the LC double focus lens, as discussed in the previous section. Since we cannot distinguish between the phase shift due to the surface and the phase shift due to the lens, the additional retardation caused by the asymmetry of the lens on the reference beam is directly visible in the measurement of the test surface. Of course, this measurement artefact can be recorded and subtracted for the following measurements.
From the local irregularities (less than 50 nm fluctuations) present on the measured surface (if we suppose the real surface to be perfectly flat), we can conclude that the measurement precision for the present interferometer is not better than λ/10.

4.1.6 Conclusion

We have shown that with the presented interferometer we can make measurements with a precision of only λ/10. Actually, this precision is relatively modest compare to other high-end common-path interferometers (mostly dedicated to special surfaces) which have precisions up to λ/1000. The present version of the interferometer shows also other some limitations: it cannot be miniaturized (smaller than 10 cm) because of the limited thickness (thus curvature) and birefringence of the LC used for bifocal lenses. It also gives noisy measurements due to the poor quality of the optical

elements (polarizers and LC lens) which have been used in the present setup. Better results are expected with optical elements of higher quality as for instance prisms made of calcite and Glan-Thomson polarizers. However, this would make the device more expensive. Another important limitation of such interferometers is that the tested surfaces should not present large gradients of depth variations. If this not the case, the measured interference pattern will show frequencies that the CCD camera cannot resolve and aliasing effects will occur.
We also tried to make thick lenses made of LCP, but material shown too many defects to obtain a similarly good alignment as for the conventional LC lenses.
We have calculated and measure the astigmatism produced by the asymmetric alignment of the LC molecules. The calculations and the measurements are in good agreement.

4.2 Polarization interference microscope

The system that we present here is a polarization interferometer for phase object observation in microscopy (Differential Interference Contrast microscopy DIC). DIC is a widely used method for observation of colorless transparent objects such as cultured cells for example. These object show no clear contrast when observed with a conventional microscope. However, a DIC microscope is a relatively expensive equipment because it comprise precise birefringent prisms mostly made of inorganic crystals, such as quartz or calcite. To overcome this drawback, we present here a DIC microscope that is made of more affordable LC (polymer) prisms.

4.2.1 Principle of DIC microscopy

In DIC microscopy two lateral sheared images are created. One image is related to the ordinary polarization component and the other image to the extraordinary polarization of the light. We can principally distinguish two types of shearing interferometers: The total doubling interferometer, where the shear is greater than the linear dimension of the phase object, and the differential interferometer, where the shear is much smaller than the object dimension. The first interferometer type is not very practical since for large phase objects the lateral shear that can be obtainable with the interferometer may not be sufficient for total doubling. So, we choose here to consider a differential interferometer with a lateral shear is roughly equal to the resolving limit of the microscope. When these two slightly shifted images are superposed to interfere, the interferogram reveals the gradient of the optical thickness of the observed object. The most widely used DIC is the Smith interferometer with two modified Wollaston prisms for the polarization splitting. Figure 4.11 illustrates the principle of the apparatus. The light passes first a through a polarizer that polarizes the light at 45°. Then it passes through the first modified Wollaston prism (or Nomarski prism) N1 to produce a lateral share between the two polarization components E and O indicated by the dashed lines. It is placed so that the front focal plane of the condenser coincides with the plane of the fringes of the prism. The two rays traverse the phase object at slightly different points. The light is then collected by the objective and the rays are recombined with a second Nomarski prism N2. N2 is placed (as N1) so that the rear focal plane (dashed line) of the objective coincides with the plane of the fringes. Finally, the light passes the second polarizer to enable the two polarization components to interfere.

The Nomarski prisms can in principle be replaced by conventional Wollaston prisms, as it is the case in the Smith-type DIC microscope. But since the back focal length of the objective is generally small, the Wollaston prism, that has his plane of apparent splitting inside the system (see section 1.3.5), must be placed very close to the objective. This is for practical reasons not always possible.

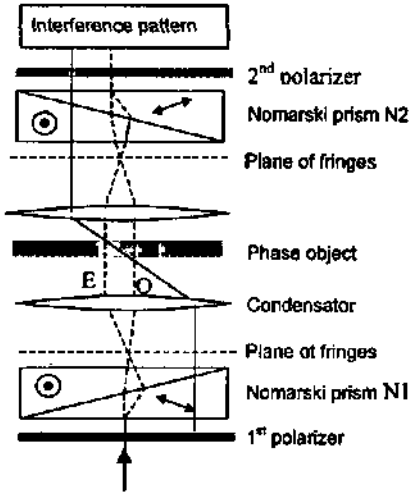

Fig. 4.11: Schematic overview of the Smith interferometer.

One has to be aware that off-axis rays (dotted line) will have different phase shifts than the on-axis rays because, they pass through N1 at different positions. N2 compensate the phase shift produced by N1 if the following condition

$$\alpha_1 \cdot f_1 = \alpha_2 \cdot f_2 \qquad (4.12)$$

is fulfilled [12], where α_1 and α_2 are the splitting angles of N1 and N2 respectively, f_1 is front focal distance of the condensator and f_2 the rear focal distance of the objective. If this condition is fulfilled, the prisms are said to be conjugated.

A similar set-up can also be used for reflection DIC. In this case, the setup corresponds roughly to the upper half of Fig. 4.11; the same Nomarski prism is used for the splitting and the recombination of the two rays

Note that the DIC system has to be used preferably with strain free objectives in order to avoid any additional birefringent phase shift. Also plastic substrates are not recommended for the same reason.

4.2.2 The Françon-Yamamoto configuration

For our purposes, we need a design that can be implemented with the developed LC technology and that can be easily installed in a conventional polarization microscope. The main problem of the Smith interferometer shown in Fig. 4.11 is the necessity of a tilted optical axis in the first wedge of the Nomarski prism. Only small tilts can be obtained with LC polymer technology (maximum 7°) and the prisms have to be

placed very accurately. Moreover, the back focal plane of the objective is not always accessible. To avoid these difficulties, Françon and Yamamoto [13] have devised a system that is based on two conventional Wollaston prisms and which do not need to be positioned at a specific place. The schematic setup of the system is shown in Fig. 4.12. As for the Smith interferometer, the two Wollaston prisms must be conjugated in order to compensate the phase shift that they produce for off axis rays. The conjugation condition (Eq.(4.12)) can be expressed as

$$\nu_{W1} \cdot M_{cond} = \nu_{W2} \cdot M_{obj}, \tag{4.13}$$

where ν_{Wi} are the frequencies of the fringes produced by the Wollaston prisms on its own, M_{cond} and M_{obj} are the magnification of the fringes produced by the condenser and the objective, respectively. These magnification terms depend of course on the position of the Wollaston prisms. If this condition is fulfilled and the prisms are oriented so that their birefringence is compensated, we obtain a uniform illumination (without object sample).

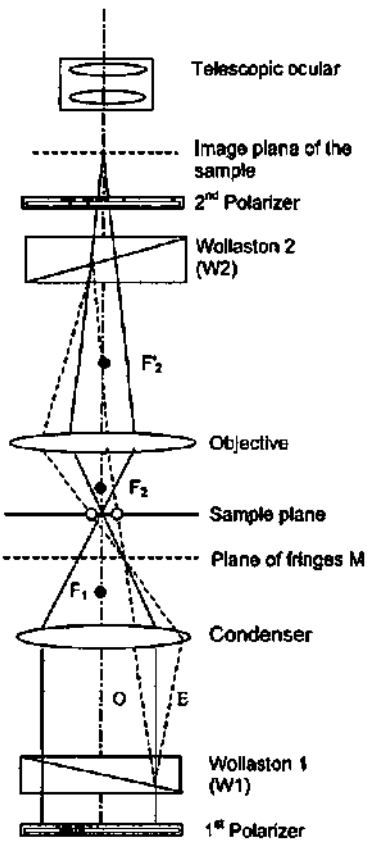

Fig. 4.12:Schematic setup of the Françon-Yamamoto interferometer. The dashed rays show the paths followed by the ordinary (O) and extraordinary (E) rays. The continuous lines represent the light paths without considering the polarization splitting.

The dashed lines O and E represent the ordinary and extraordinary rays created by the splitting for an off-axis incoming ray at the Wollaston prism W1. They intersect in the plane of fringe localization. Then, they pass through the sample at two slightly separated points indicated by the white dots. After passing the objective, the two rays are set parallel by the Wollaston prism W2. Finally, the 2nd polarizer makes the two rays to interfere. The main difference of this system compared with the Smith interferometer is that the fringes are localized near the front focal plane of the objective and not in the back focal plane. This configuration has several advantages:

- W1 and W2 are not required to be placed at a specific positions, as in the case of Fig. 4.11. However, the objective and the condenser have to be adjusted so that the fringes belonging to the two systems are both imaged in M.
- The optical axis of W1 and W2 do not need particular tilt angle, which is particularly advantageous when using LC technology.
- Since the birefringence induced by W2 is compensated by W1 (if W1 and W2 are conjugated), the whole aperture can be used (as for the Smith interferometer).

4.2.3 Experimental results

We realized the Françon-Yamamoto configuration shown in the previous section, with the LC technology described in chapter 2.
We have fabricated a first Wollaston prism pair having thicknesses of 125 µm and 36 µm, respectively. We did insert the prisms in a Leica DMRX polarization microscope. We adjusted the positions of W1 (125 µm), W2 (36 µm), the objective (20x, NA = 0.4) and the condensator to fulfill the condition of Eq.(4.13). Experimentally, this condition is satisfied when a uniform illumination is observed in the object plane. We could not obtain a perfect compensation over the whole aperture because of the deformation of the Wollaston prisms. However, we finally succeed to end up with the configuration described in Fig. 4.12.
The phase objects (samples) were fabricated by immersing transparent microstructures in a fluid with a similar refractive index. These transparent samples can hardly be observed with a microscope, which is not equipped with DIC.
Figure 4.13a shows a plastic grating with a period of about 10 µm that is immersed in a close index matching fluid. Fig. 4.13b shows that turning the same grating by 90° makes the interference pattern disappear. This can be understood if we consider that only optical path gradients in the plane of splitting can be observed with this interferometer.

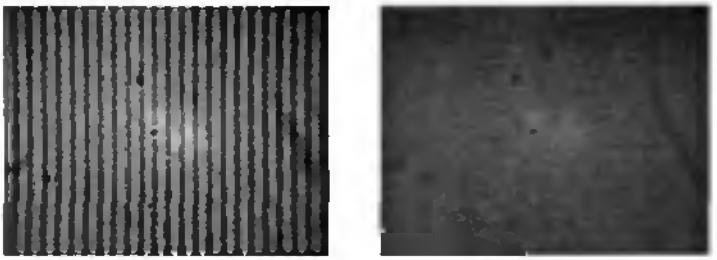

(a) (b)

Fig. 4.13: (a) 10μm grating immersed in index matching fluid observed with the Françon-Yomamato interferometer. (b) Same grating turned by 90°, the grating is now parallel to the splitting plane of the wollaston prisms and the interference pattern disappears

Figure 4.14a shows an array of micro-lenses (diameter of about 0.1 mm) immersed in an close index matching fluid observed with the interferometer. The picture renders a three dimensional impression of the structures and also reveals the presence of small defects. Figure 4.14b shows the same sample when the second polarizer is removed, which is equivalent to "switching off" the interferometer.

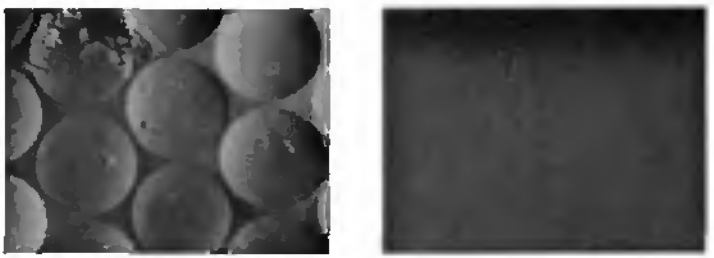

(a) (b)

Fig. 4.14: (a) Array of micro-lenses immersed with an index matching fluid observed with the liquid crystal DIC apparatus. (b) The array cannot be observed when the DIC apparatus is removed.

We have fabricated a more robust second pair of Wollaston prisms made this time of LC polymer (RM-257). The prisms have thicknesses of 50 μm and 125 μm, repectively. As previously described for the first pair, we adjusted the optical elements of the microscope to get the desired configuration. Similar results as shown in Figures 4.13 and 4.14 were obtained. Figure 4.15a shows a picture that has been obtained with the polymer variant. It represents interference pattern obtained by looking at the surface of a fluid disturbed by a dust particle. The variation of the fringe spacing indicates that the surface is strongly bend in the neighborhood of the particle. Figure 4.15b shows the same particle when the DIC interferometer is "switched off" by removing the second polarizer.

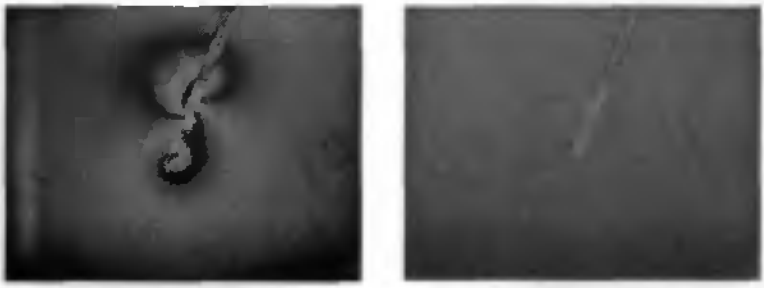

(a) (b)

Fig. 4.15: (a) Interference pattern that shows the topology of a fluidic surface deformed by a dust particle. (b) The same surface observed without second polarizer (interferometer is disabled).

4.2.4 Conclusion

We have demonstrated here that it is possible to replace conventional inorganic birefringent elements by LC elements to perform good quality DIC measurements. Moreover, this application does in principle not need very thick elements compared to the FTS-spectrometer or the double focus interferometer describe in section 4.1. So, optical elements without too many defects and scattering losses can be achieved. The Françon-Yamamoto configuration is well suited for the LC technology, because it does not need birefringent elements with highly tilted optical axis. Also, it presents the advantage that it can be installed in any polarization microscope having adjustable condensator and sample position.

4.3 References

[1] J. Dayson, "Common-path interferometer for testing purposes", *Journal of OSA*, 47, pp. 386-390, 1957.

[2] M.J. Down, M.H McGiven and H.J Ferguson, "optical systems for measuring the profiles of super-smooth surfaces", *Precision Engineering*, 7, pp.211-215, 1985.

[3] H. Kikuta and K. Iwata, "Phase-shifting common-path interferometers using double focus lenses for surface profiling", Proc. SPIE, 1720, p.133, 1992.

[4] K. Iwata and N. Nishikawa, "Profile measurement with a phase shifting common-path polarization interferometer", Proc. SPIE, 1162, pp.389-384, 1989.

[5] H.Kikuta, T.Tanabe and K.Iwata, "Double focus interferometer and the influence of their sample setting errors", *Optical review*, 1, pp.266-269, 1994.

[6] T. Nose, S. Masuada and S. Sato, "Application of a Liquid Crystal Lens to a Double Focusing Common Path Interferometer", Proc. SPIE, 3143, p.165, 1997.

[7] T. Nose, M. Honma, and S. Sato, "Influence of the Spherical Substrate in the Liquid Crystal Lens on the Optical Properties and Molecular Orientation State", Proc. SPIE, 4418, P.120, 2001.

[8] Schwider, O.Falkenstorfer and H.Schreiber, New compensating four-phase algorithm for phase-shift interferometry, *Optical Engineering*, 32, pp.1883-1885, 1993.

[9] A.Asundi and K.Yung, Phase-shifting and logical moiré, *J.Opt.Soc.Am.A*, 8, No.10, October 1991,1591-1601.

[10] J. Novák, "Method for 2-D phase unwrapping in matlab", unpublished.

[11] Freeware program "Automatic Fringe Analysis (FRAN)", university of Warwick, Optical Engineering laboratory.

[12] M. Françon and S.Mallick, *Polarization Intreferometers*, p.57, Wiley, New-York 1971.

[13] M. Françon and T. Yamamoto, "Un nouveau et très simple dispositif interférentiel applicable au microscope", *Opt. Acta*, 9, pp.395-408, 1962.

Chapter 5

Conclusion

Passif birefringent optical elements made of LC technology offers many advantages compared to inorganic crystal:

- It permits to introduce twisted optical axis or hybrid alignments such as the planar-homeotropic alignment (Inorganic crystals are essentially limited to planar alignments).
- By using gratings or photo-sensible alignment layers (chapter 2), small domains with different orientation of the optical axis can be obtained.
- By using adequate substrates or molding technologies a wide variety of shapes, such as lenses (chapter 4) or even micro-structures, can be fabricated.
- Fabrication of LC elements is relatively inexpensive.

In chapter 2, we have investigated different type of LC materials such as nematic, smectic or polymer LCs. We found that the latter is particularly well suited for industrial application because of its robustness and its low temperature dependence. We have also shown that the LC polymers are compatible with several alignment methods, such as the alignment with rubbed polymide, photo-polymerized layers, and that components with good optical quality can be obtained. By using adequate molecules, good alignment with reasonable magnetic fields may be obtained, which opens new perspectives for making thicker components. This wide range of alignment technologies, which permit to play freely with optical axis, offers new design possibilities.

Design of complex birefringent systems is still not a very common task. One major difficulty is to simulate optical system containing elements with twisted structures. We have shown that it is possible to simulate such systems by methods that have been implemented in a commercially available polarization ray-trace program. These methods have been applied to the polarization interferometer treated in chapter 3. The simulated angular dependence and the interferograms were in good agreement with the experimental results for incidence angles up to 35°.

With the help of the developed technology and design methods, we realized a low-resolution hand held Fourier transform spectrometer. We found a novel compact design having an acceptance angle of at least ±35° (for zero OPD) and a resolution of 10 nm (at 633 nm). By using LC polymer instead of conventional LCs, we achieved to reduce the temperature dependence by at least a factor of 10 to less than 0.1 nm/K. We also have increased significantly the SNR (about a factor of 5) by making phase/anti-phase measurements by switching the entrance polarization state with a twisted nematic cell. The main disadvantage of the spectrometer is the weak transmission for wavelengths below 420 nm.

In chapter 4, we have presented two other applications, which are also polarization interferometers. The first application is a double focus common path interferometer, which is used for surface measurements. We have shown that the measurements were distorted by the inherent astigmatism of the birefringent lens. We only obtained a measurement precision of $\lambda/10$, which is very low compared with classical versions of this kind of instruments. The second application is a shearing interferometer for differential interference contrast microscopy. We installed it in a conventional polarization microscope. We obtained representations of the observed phase objects of good quality, which indicates that the expensive calcite or quartz elements used for such devices can throughout be replaced by LC polymer elements.
In general, interferometry requires precise optics. In this thesis, we have shown that LC (especially LC polymer) birefringent optical elements can be used for such applications. However, corrections such as the phase or background corrections for the spectrometer or the astigmatism correction for the LC lens are necessary. Ideally, due to the absorption, LC polymer elements should be used for application in the VIS and NIR. Also, the elements should not exceed a few hundreds micrometers thickness because of the scattering losses and the alignment difficulties. In technologies such as micro-optics or integrated optics where the devices are small, these conditions are fulfilled. So, LC polymers can advantageously be used in combination with these technologies. Moreover, other interesting functions such as Bragg reflectors made of cholesteric polymer LCs may also be integrated. Since the field of LC polymers is relatively new, progress is expected and materials with better or new properties will enlarge the range of possibilities. By playing with all these elements, one should be able to design in the future compact systems, which have the polarization state of light as a new degree of freedom.

Acknowledgements

This thesis work took place from October 1999 to June 2003 jointly at the Centre Suisse d'Electronique et de Microtechnique in Zürich and the Institute of Microtechnology at the University of Neuchâtel. I thank all my colleagues from Neuchâtel and Zürich for the good time I had with them. I wish to thank particularly:

- René Dändliker for being an excellent thesis director.
- Peter Seitz for hiring me and for the confidence he showed me.
- Dick Broer and Joachim Grupp for accepting to be co-examiners of this thesis.
- Toralf Scharf for being an excellent and engaged supervisor during my entire thesis.
- Roger Dangel for introducing me to the world of interferometry and liquid crystals during the first year of my thesis.
- Patrick Ruffieux for his valuable collaboration in building LC-spectrometers.
- Carsten Winnewisser for supervising my work at the CSEM during the last year.
- Kaspar Cottier, Arm Cronie, Michael Bianci and Pierre-Yves Baroni for their precious collaboration in different projects related to my thesis.
- Joachim Grupp again for his support and valuable advice during the thesis and for allowing me to use the facilities of the ASULAB laboratories.
- Jean-Michel Künzi for helping me to repair the magnet and the deposition chamber.
- The staff of the high magnetic field laboratory at the university Nijmegen. Especially Giorgia Tordini and Igor Shklyarevskiy who helped me run the installation during the long nights of measurement.
- Irène Philipoussis, Christian Zschokke, Susanne Westenhöfer and Ernst Meier for the countless gratings, polyimide substrates, holders etc. that they have made for me.
- Hans-Peter Herzig, Omar Manzardo and Christian Bohley for the interesting discussions and their advice.
- Martin Salt for correcting my English.
- Guido Niederer, Christian Bohley and Michael Kiy for sharing their office with me.
- The Albert Köchlin foundation, the Commission for technology and innovation and the CSEM for their financial support.

• Toralf, Patrick, Christian, Carsten, Omar, Guido, Martin, Olivier, Christophe, Thomas, Roger, Michael, Andreas, Sylvain, Yves, Marcel, Manuel, Antonello, Ville, Iwan, Felix, Piero, Emiliano for the good moments we had together outside working hours.

J'aimerais aussi remercier tous mes potes et en particulier « La Lieuban » pour avoir partagé avec moi les nombreux moments de détentes et de divertissements indispensables à l'équilibre physique et psychique d'un thésard. Un grand merci également à mes parents qui m'ont supportés moralement et financièrement pendant mes études.
Finalement, j'aimerais remercier du fond de mon cœur ma petite Jane adorée sans qui je n'aurais probablement jamais eu le courage de commencer cette thèse.

Annex 1

Compact static Fourier transform spectrometer with a large field of view based on liquid-crystal technology

Gerben Boer, Toralf Scharf, and René Dändliker

We present designs of static Fourier transform spectrometers that are based on a Wollaston prism with a large field of view. Besides the usual advantages of static Fourier spectrometers (large resolving power, large wave-number range, high throughput), these designs also present the advantage of using relatively cheap liquid-crystal technology. The use of twisted liquid-crystal structures gives a large field of view, which in turn gives the ability to collect more light from a divergent light source. Measurements are compared with simulations. Different simulation principles are used. We found new configurations by using twisted structures that show a large field of view. © 2002 Optical Society of America

OCIS codes: 930.0230, 120.6200, 230.5440, 260.3160, 300.6300.

1. Introduction

A Fourier transform spectrometer (FTS) operates by splitting an incoming beam into two parts, applying a differential phase shift, and then recombining the beams. This phase shift is varied either temporally, for instance by translating a mirror in a Michelson-type interferometer, or spatially, like in a tilted mirror Michelson-type interferometer. The spectrum can be found by applying a Fourier transform on the measured intensity pattern. The main advantages of the FTS are the large optical throughput (Jacquinot advantage[1]), the multiplexing (Fellgett advantage[2]), and the wide spectral coverage. Moreover, if the phase shifts are varied spatially, then there are no moving parts anymore, and the whole interferogram can be acquired on a detector array.[3]

The FTS designs, which we present, are polarization interferometers[4] and use modified Wollaston prisms. The incoming linear polarized light is split into two orthogonal polarized components that undergo different optical paths. The resulting phase shift varies spatially. The polarization components are recombined at the output of the prism by a polarizer and transformed into an intensity pattern. This type of FTS does not present the usual disadvantages, such as alignment difficulties and vibration sensitivity. Several designs based on a Wollaston prism have already been proposed.[5–7] These designs use conventional birefringent materials. As a result of the relatively low birefringence Δn of crystal materials such as quartz ($\Delta n = 0.01$), the systems are often bulky. In this paper we describe new designs that use liquid-crystal (LC) technology,[8] which offers the possibility of applying LC cell fabrication processes. The birefringence of LC materials can be higher than that of calcite ($\Delta n > 0.17$), and the technology opens new design perspectives with a twisted optical axis (twisted nematic cells). We present several designs having a large field of view.

2. Design Principles

In principle, every birefringent system that induces a spatially varying phase shift can serve as a polarization interferometer.[9] The shape of the interference fringes depends on the geometry of the birefringent elements. One can use birefringent prisms or lenses to build up such interferometers.

Using LC technology with twisted structures of the nematic liquid crystal (i.e., rotation of the optical axis), one can manufacture new unusual designs of birefringent prisms. Here we want to limit our attention to birefringent prisms that have a 0° or 90° twist. Because of increasing complexity, we study

G. Boer (gbo@csem.ch) is with the Centre Suisse d'Electronique et Microtechnique SA Zürich, Badenerstrasse 569, 8048 Zürich, Switzerland. T. Scharf and R. Dändliker are with the Institute of Microtechnology Neuchâtel, University of Neuchâtel, Rue A.-L. Breguet 2, 2000 Neuchâtel, Switzerland.

Received 20 July 2001; revised manuscript received 15 November 2001.

0003-6935/02/071400-08$15.00/0

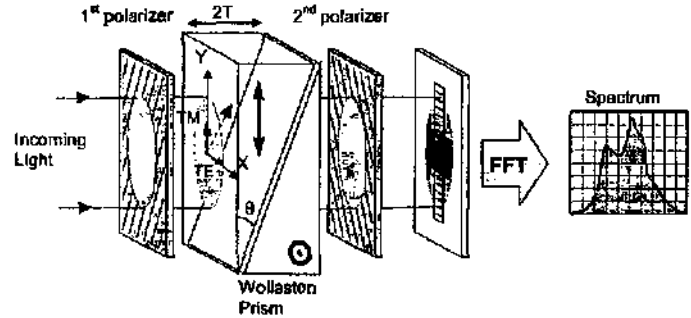

Fig. 1. Principle of a fast Fourier transform (FFT) spectrometer based on a Wollaston prism.

only those systems that have a maximum of three birefringent elements. There are many possible combinations of twisted and planar LC cells. Beside the normal Wollaston configuration, a twisted–twisted Wollaston prism, a planar–planar configuration with a twisted nematic cell in between, a planar–twisted Wollaston prism, and a planar-twisted configuration with a twisted cell in between are also possible. We discuss in detail the results for the first three possibilities. The general idea is to change the direction of polarization with respect to the wedge angle by rotating it with birefringent elements. These elements must be nondispersive. Therefore twisted LC layers are used, which can rotate a linear polarization without changing the state of polarization.

However, this perfect rotation of the polarization is only achieved if the so-called Mauguin condition[10] is fulfilled. This condition states that the waveguiding or adiabatic regime for a 90° twisted cell takes place if the birefringence times the cell thickness is large compared with the wavelength; that is, $\Delta n\, d/\lambda \ll 1$. If this condition is not fulfilled then the polarization components do not follow the twisted optical axis without changing their state of polarization, and this introduces contrast reduction and interference pattern distortions. For the thick twisted LC structures that we used in our experiments, the Mauguin condition is always fulfilled, except at very thin regions of the wedge cell where the thickness of the cell becomes smaller than 10 μm. The phase shift for each component of a certain polarization is approximately the same as for a planar structure and is given by the product of the thickness of the layer and the ordinary or extraordinary refractive index,[10] respectively.

To start with, the principle of the polarized FTS is explained by using the conventional Wollaston prism. Figure 1 schematically shows the principle of a static polarization FTS. The first birefringent element of the Wollaston prism has its optical axis along the y direction. The incoming light is linearly polarized at ±45° by the first polarizer and can be decomposed into two orthogonal polarized components: a TM component parallel to the x axis and a TE component parallel to the y axis. In the first prism, the TM polarization is parallel and the TE polarization is perpendicular to the optical axis, respectively. Therefore, TE polarization sees an ordinary refractive index of n_o and TM polarization sees an extraordinary index of n_e. In the second prism, the optical axis is rotated by 90° with respect to the first prism.

Consequently, the TE component now experiences n_e and TM experiences n_o. Because of the geometry of the Wollaston prism, which is composed of two wedges, a linearly varying phase shift along the y direction is introduced between the two components. For normal incidence the phase shift δ is given by

$$\delta = (2\pi/\lambda)2y(n_e - n_o)\tan\theta, \qquad (1)$$

where θ is the angle of the wedges and y is the position along the y axis. A second polarizer at ±45° is placed at the output of the Wollaston prism to recombine the two orthogonal polarization components and to produce an interference intensity pattern in the detector plane. Note that in the center ($y = 0$), where the thickness of the wedges is equal, the phase shift δ becomes zero. The observed interferogram for monochromatic light at normal incidence has the form[11]

$$I = I_0[\cos^2\chi - \sin 2\phi \sin 2(\phi - \chi)\sin^2(\delta/2)], \qquad (2)$$

where φ is the angle of the first polarizer with respect to the x axis, χ is the angle between the two polarizers, I_0 is the intensity of the incoming light, and δ is the spatial varying phase shift given by Eq. (1). In our case, for parallel polarizers $\chi = 0°$ and with a polarizer angle of $\phi = 45°$, the detected intensity becomes

$$I = I_0[1 - \sin^2(\delta/2)] = I_0[\cos^2(\delta/2)]. \qquad (3)$$

In this idealized case for monochromatic light and normal incidence, the intensity modulation is strictly periodic in the y direction and looks like a cosine-squared interferogram. For polychromatic light, one has a superposition of such interferograms with

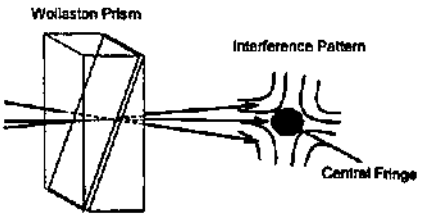

Fig. 2. Central fringe of the interference pattern gives the acceptance angle (or field of view).

different spatial frequencies. A Fourier transform of the obtained spatial intensity distribution provides with adequate calibration the spectral power density of the incident light, and hence the spectrum. There are several alignment requirements to fulfill: the parallelism of the polarizers (the angle χ), the position of the polarizers with respect to the optical axes of the prisms (angle ϕ), and the orientation of the optical axis of the prisms itself. If the alignment of the optical components is not perfect, then the intensity is changed according to Eq. (2). If we assume a small alignment error of an angle $\Delta\chi$ between the two polarizers, then, for parallel polarizers under 45° with respect to the optical axis, Eq. (2) becomes

$$I = I_0[\cos^2(\Delta\chi) - \sin[(\pi/2) + 2\Delta\chi]\sin^2(\delta/2)]. \quad (4)$$

For small $\Delta\chi$, light intensity I does not change much because $\cos 2(\Delta\chi)$ and $\sin(\pi/2 + 2\Delta\chi) = \cos(2\Delta\chi)$ are near the extreme points. It can be shown that intensity I is also insensitive to small variations of ϕ. Therefore, the alignment of the optical components is not critical and the contrast reduction caused by such misalignments is small.

The resolution $\Delta\nu$ (in wave numbers) of a FTS is given by $\Delta\nu = |1/\Delta L|$, where $\Delta L = 2\Delta nT$ is the maximum optical path difference across the used aperture. With $\Delta\nu = -\Delta\lambda/\lambda^2$ one finds

$$\Delta\lambda = \lambda^2/\Delta L = \lambda^2/2T\Delta n, \quad (5)$$

where $2T$ is the total thickness of the Wollaston prism and Δn is the birefringence.

The path difference between the two polarization components changes with the angle of incidence of the incoming light. As schematically shown in Fig. 2, different rays, which are focused in the same point of the cell, traverse the Wollaston prism at different angles. Because of the angular dependence of the system, the two polarizations in these rays undergo different phase shifts. If the Wollaston prism is placed between crossed polarizers, an interference pattern is produced in the far field as shown in Fig. 2. The size of the central fringe gives a good indication of the angular dependence. Generally, we want to have a small angular dependence because rays arriving at the same point with different phase shifts reduce the interference contrast. The acceptance angle (field of view) corresponds to the range of input angles for which the reduction of the contrast is acceptable. In general, the field of view can be defined as the maximum angle[7] for which the path difference of the two polarization components for different rays does not vary by more than $\lambda/2$. For practical purposes, one uses much smaller angles to have a sufficient contrast of the interferogram. The acceptance angle depends on the design, and for that purpose wide-angle double Wollaston prisms have already been developed.[5–7]

LC technology offers a variety of new designs, but there are limitations too. The scattering and absorption losses might be much larger for thick LC cells than for conventional crystal Wollaston prisms. For a Wollaston prism made of a nematic mixture (such as BL006 from Merck) with a thickness of 200 μm with $\Delta n = 0.28$, the scattering losses are approximately 15% and absorption losses can be approximately 35% for certain wavelengths. With adequate polarizers, such a spectrometer can be used in the wavelength range from 400 nm to 2000 nm. For practical applications one has to be aware that the birefringence of the LC is temperature dependent and has a relatively large dispersion.[12] As a result of the manufacturing process, a pretilt angle of the optical axis with respect to the substrate surface is always present. This inclination of the optical axis shifts the center of the interferogram and influences the localization of the plane of maximal contrast.

3. Optical Design Simulations

The optical design of a static FTS based on polarization of light can be simulated in different ways. A calculation of phase differences for polarized light is possible with ray tracing, including polarization effects of anisotropic materials. In this concept, refraction is taken into account by splitting rays at each surface and propagating the polarization components separately. Such simulations can be performed with commercially available programs. We used the nonsequential ray-trace program known as ASAP.[13] This simulation program has the ability to simulate anisotropic materials, that is, crystals, which are uniaxial. At the interface of the crystal, rays are split into an ordinary ray and an extraordinary ray with respect to the orientation of the local optical axis. At the detector plane the rays are coherently added. We consider our LC cells as ideal uniaxial crystal wedges without scattering or geometrical defects. Polarizers are also considered as ideal and are modeled by ASAP by using the Jones calculus. Materials with a twisted optical axis (e.g., twisted nematic cells) are more difficult to simulate. As shown in Fig. 3, we model the twisted nematic LC configuration by dividing the wedge cell in a set of slices with increasing rotation of the optical axis. This means that in the direction of light propagation the optical axis of each slice is rotated by a constant amount with respect to the previous one. Unfortunately, we had to limit the calculation to 14 slices (7 per wedge),

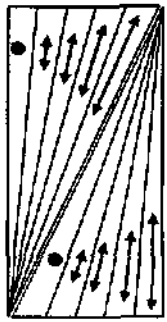

Fig. 3. Schematic representation of the slice model used to simulate twisted nematic wedge cells in the ASAP program. The 90° twisted optical axis (represented by the arrows) is divided in slices with discrete rotation angles.

because the splitting doubles the number of rays at each interface and consequently the computing time becomes too important.

A different approach neglects the splitting of rays at the surfaces and calculates only the phase shift between the ordinary and extraordinary polarization components. Conventional matrix methods for polarizations optics such as a Jones matrix or the Berreman matrix method[10] are usually applied in this case. We used a commercial program[14] (LCD Master from Shinteth) that was developed for the optimization of LC display optics. This program can only handle planar geometries, and therefore our wedge geometry cannot be exactly modeled. However, considering the small wedge angle of less than 1°, we can assume that we have a locally planar configuration. When calculating the angular dependence of the transmitted light intensity between polarizers, the program focuses the light exactly in the center of the system, which does not always coincide with the plane of maximal contrast. Fresnel reflection losses at the interfaces were taken into account.

We will see that both simulation methods, that is beam splitting and Jonas matrices, give similar results. The simulations are also in good agreement with the experimental observations. The Jonas matrix method with LCD Master has the advantage of short computation times, and the system configuration can be easily defined in the program. However, this method is limited to angular dependence studies and allows only planar configurations. In contrast, when twisted configurations are encountered, the beam splitting method with ASAP is delicate to implement and the computation time is important. However, ASAP permits us to implement birefringent elements of any geometry and to add any other optical component in the system.

4. Experiment

To fabricate the LC cells, we used squared 25 mm × 25 mm glass substrates with a thickness of 0.5 mm. The glass substrates were cleaned in an ultrasonic bath and coated with Dupont-Hitachi PI 2545 polyimide by spin coating. The polyimide was then polymerized and mechanically rubbed parallel to the desired orientation of the LC director. The pretilt angle for the polyimide PI 2545 is approximately 3°. Plastic spacer foils with a thickness of 200 μm were used and placed on one side between the substrates to obtain a wedge-shaped cell. The orientation of the rubbing direction allows for the construction of planar and twisted cells. Twisted cells with a 90° twist were manufactured by assembling the glass substrates with perpendicular rubbing directions. A chiral dopant (Merck CB15) was added to the LC for the twisted cells in order to avoid domains with different rotating directions. The substrates were then glued together and filled through the open sides with highly birefringent nematic LC (Merck BL006, Δn = 0.28). After relaxation of the LC texture, the cells were completely sealed. Two wedge-shaped cells were finally brought together to form a Wollaston prism.

To study the angular dependence experimentally, we used the conventional conoscopic method.[15,16] We observed the back focal plane of the microscope objective. The observations were made with a polarizing microscope (Leica DMRX). Interference filters were used for different wavelengths. A condenser with a numerical aperture of N.A. = 0.65 and a 40× magnification microscope objective with N.A. = 0.6 and a long working distance allows us to observe an angle of approximately ±35°. The pictures were taken with a digital camera (Nikon Coolpix 950).

5. Results and Discussion

We concentrate our discussion on three different designs. The first is the classical design, which has already been studied in several publications.[5,17–19] The other two designs use twisted LC structures to increase the field of view. We have used the same LC parameters with a birefringence of $\Delta n = 0.28$ (n_o = 1.53 and n_e = 1.81) and the same wedge dimensions (wedge angle $\theta = 0.7$ and total thickness $2T$ = 0.2 mm) for all the designs. Consequently, they also have approximately the same resolution of $\Delta\lambda = 7$ nm at 633 nm as given by Eq. (5). Because we use a spatially incoherent source for the conoscopic observations, the plane of maximal contrast is localized.[11,20] For the designs with twisted LC structures, we obtain the maximum fringe contrast by focusing the microscope objective near the interface between the two wedges (also for large optical path differences, or OPDs). So, the plane of maximal contrast is localized inside the system.

The first design, presented in Fig. 4(a), is a classical Wollaston prism. It consists of two similar wedges made out of a birefringent material and joined by their hypotenuses. The optical axes are mutually perpendicular at the interface of the two wedges. A

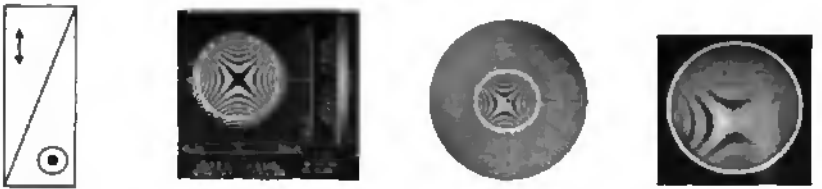

Fig. 4. (a) Schematic of the design with a standard Wollaston prism consisting of two wedges with orthogonal optical axes. The field of view is simulated by (b) ASAP and (c) LCD Master. (d) Conoscopic observation. The circle has a radius of 35°.

theoretical approximation of the field of view[4] is given by the maximal incidence angle i through

$$i^2 = \frac{\lambda}{T}\frac{n_o^2 n_e}{n_e^2 - n_o^2}, \tag{6}$$

where $2T$ is the total thickness of the Wollaston prism. With our set of parameters ($n_o = 1.53$, $n_e = 1.81$, and total thickness $2T = 0.2$ mm) we obtain approximately $i = \pm 10°$ at a wavelength λ of 633 nm.

Figures 4(b), 4(c), and 4(d) show the interference pattern in the far field. The white circle added to the figures represents the field of view within 35°. We notice here that the central fringe of simulations and the conoscopic measurement covers an angular range of approximately ±10°, which corresponds to the predicted theoretical value.

The second design, presented in Fig. 5(a), consists of two wedges with twisted optical axes. This means that the optical axes are rotated by 90° in the two wedges when traversing the cell independently of the cell thickness. The two polarizers are oriented at ±45° respective to the optical axis of the entrance and the output. One has to distinguish two different cases: rotation of the optical axis in the same or in the opposite sense. The conoscopic measurements and simulations of the design with the same sense of twist are presented in Figs. 5(b), 5(c), and 5(d). The measurement shows no fringes and we can conclude that the field of view is larger than ±35°. The LCD Master simulations show a field of view up to ±60°. A qualitative explanation of this large field of view can be found by looking at the phase shifts that undergo the two polarization components as shown in Fig. 6. Here we consider an arbitrary ray going through the center of the system and we compare the phase shift induced by the first and second wedges. When going through the first wedge, the orientation of the two polarization components follows the orientation of the twisted optical axis (indicated by the arrows). Therefore, TE and TM components will experience the ordinary n_o and the extraordinary n_e refractive indices, respectively.

Because the Mauguin limit is fulfilled, the phase shift between the two components at the output of the first wedge will be approximately the same as in the classical design but the direction of the polarizations is rotated by 90°. At the interface we have an identical situation (because the wedges are identical) as at the entrance of the first wedge, but now the TE and TM components are interchanged. So, TE and TM polarization will undergo exactly the opposite path differences as in the first wedge. We finally end up with a zero path difference between the two polarization components. The same arguments hold for all the other possible paths intersecting at this point. Thus for any incidence angle the phase shift induced in the first prism is perfectly compensated in the second one. Therefore at least for the center point of the system (OPD = 0) this design is perfectly angle independent.

The system presented in Fig. 7(a) is very similar to the previous one, except that the sense of rotation of the optical axes of the two wedges is opposite. The conoscopic measurement and the simulations pre-

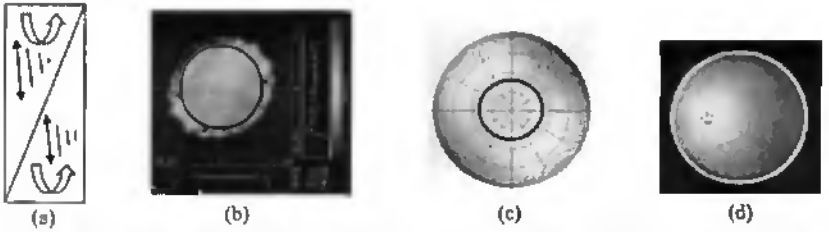

Fig. 5. (a) Schematic of the design with two LC wedges twisted in the same sense. The field of view is simulated by (b) ASAP and (c) LCD Master. (d) Conoscopic observation. The circle has a radius of 35°.

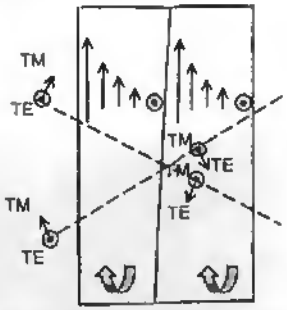

Fig. 6. Schematic view of the evolution of the two polarization components (TE and TM) of an arbitrary path going through two wedges with equal twist sense.

sented in Figs. 7(b), 7(c), and 7(d) show a field of view of only ±10°. This result appears quite surprising, because of the similarity to the system with equal twist sense. We can get some qualitative understanding about the difference of this result if we look at the phase shift between the two polarization components TE and TM of an arbitrary ray going through the center of the system. In the first wedge with positive twist sense, the TE and TM components are rotated by +90° and undergo a certain phase shift. In the second wedge with negative twist, the TE and TM components are rotated by −90°. Now the phase shift between the TE and TM components is not exactly opposite to the phase shift induced in the first wedge, because of the opposite twist. In other words, the phase shift induced in the first wedge is not perfectly compensated by the second wedge as a result of the asymmetry of the optical axis directors between the first and second wedges. This may explain the small field of view compared with that of the previous design with equal twist. Because of the complexity of the twisted structures, which must be modeled in three dimensions, we did not find at this time any other convincing arguments to explain the obtained results.

Note also that for the same polarizer orientations, the cross in the interference pattern shown in Fig. 7(d) is rotated by 45° compared with the one shown in Fig. 4(d).

The fourth design, presented in Fig. 8(a), consists of two identical wedges with a parallel optical axis and a 20-μm-thick twisted nematic cell placed in between them. The twisted nematic cell rotates the output polarizations of the first wedge by 90°. Therefore, at the entrance of the second wedge, we have the same situation as at the entrance of the first wedge, but the TE and TM components are swapped. When going through the first wedge, TE and TM polarizations will experience the ordinary n_o and the extraordinary n_e refractive indices, respectively. The twisted nematic cell rotates the direction of the polarizations by 90°. At the interface the TE and the TM polarizations are interchanged and undergo

Fig. 7. (a) Schematic of the design with two LC wedges of opposite twist sense. The field of view is simulated by (b) ASAP and (c) LCD Master. (d) Conoscopic observation. The circle has a radius of 35°.

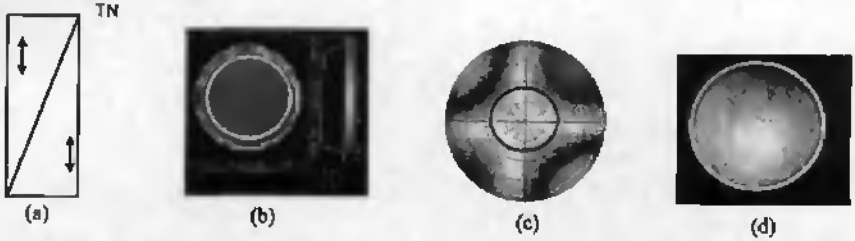

Fig. 8. (a) Schematic of the design with two wedges with parallel optical axes and a twisted nematic cell in between. The field of view is simulated by (b) ASAP and (c) LCD Master. (d) Conoscopic observation. The circle has a radius of 35°.

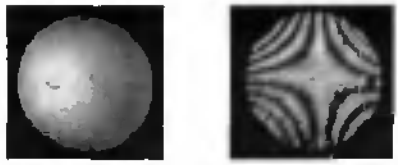

(a) (b)

Fig. 9. Conoscopic observation of the field of view at different OPDs for the design with twisted structures (Fig. 5): (a) zero OPD; (b) 2/3 of the maximum OPD.

exactly the opposite path differences in the second wedge. A very small path difference between the two polarization components is found because of the angular dependence of the twisted nematic cell. This is confirmed by the simulations and the conoscopic observation presented in Figs. 8(b), 8(c), and 8(d), which show a field of view larger than ±35°. Compared with the half-wave-plate configuration[4] suggested by Normanski, the twisted nematic cell has the advantage of low dispersion. Therefore, a white-light interferometer can be designed. Compared with the other configurations, this design has a supplementary twisted nematic cell. This is, of course, a disadvantage because this introduces additional losses and makes the system more complicated. However, the twisted nematic cell can be made relatively thin (approximately 20 μm) compared with the rest of the system so that losses are negligible.

Until now, only the angular dependences for observation points in the center of the system (OPD = 0) have been analyzed, but in general the angular dependence changes with the position in the plane of maximal contrast. For the classical design in which the angular dependence is constant, this is not the case. To be able to determine the angular dependence for every OPD, we must know the exact shape

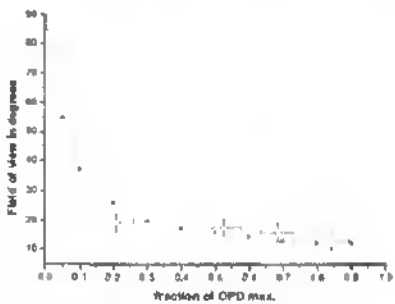

Fig. 10. Graph representing the OPD dependence of the field of view for the configuration with equal twist sense (Fig. 5): circles represent the measured values and the curve represents the calculated values.

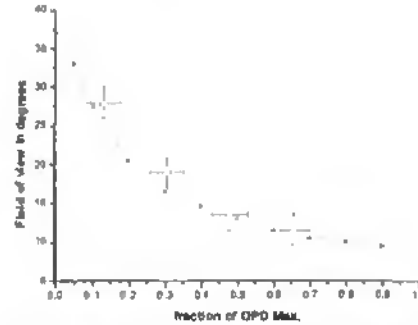

Fig. 11. Graph representing the OPD dependence of the field of view for the three-cell configuration (Fig. 8). The circles represent the measured values and the curve represents the calculated values.

and position of the plane of maximal contrast. Because of the twisted structures, the calculations to find this plane are relatively complex. For the two most promising designs, the equal twist of Fig. 5 and the three-cell configuration of Fig. 8, we determined the field of view as the function of the OPD. The results are presented in Figs. 9, 10, and 11. We measured the field of view for different OPDs by focusing the microscope objective at different places within the plane of maximal contrast. Figure 9 shows the interference pattern obtained for the configuration with equal twist sense, for a point situated at 2/3 of the maximum OPD and at OPD = 0. One observes a strongly reduced field of view for increasing OPDs. Because the wedge angle is small, we can calculate the points with a nonzero OPD with LCD Master by defining two flat cells with different thickness. The graphs shown in Figs. 10 and 11 present the calculated and the measured OPD dependence of the field of view for the equal twist sense and the three-cell configuration, respectively. For both cases the field of view decreases for increasing OPD and reaches the value for the classical Wollaston prism for the highest OPD. These results clearly indicate that both designs lose their good angular dependence with increasing OPD. However, compared with the OPD independent field of view of ± 10° of the classical Wollaston prism, the designs still offer globally a substantial increase of the field of view.

6. Summary

We have shown several possible modifications of Wollaston prisms that are based on LC technology. We computed the measured and the simulated fields of view for different designs and configurations with planar and twisted LC structures. We showed that, with the help of twisted nematic cells, it is possible to have a symmetrical system with a large field of view for OPD = 0. We also observed that the field of view decreases for a larger OPD.

References

1. R. J. Bell, *Introductory Fourier Transform Spectroscopy* (Academic, New York, 1972).
2. J. Chamberlin, *The Principle of Interferometric Spectroscopy* (Wiley Interscience, Chichester, UK, 1979).
3. O. Manzardo, P. Kipfer, and H. P. Herzig, "Dispersive compact Fourier transform spectrometer for the visible," presented at the Fourier Transform Spectroscopy: New Methods and Applications Conference, Santa Barbara, Calif., 22–24 June 1999.
4. M. Françon and S. Mallick, *Polarization Interferometers* (Wiley Interscience, New York, 1971).
5. M. J. Padgett, A. R. Harvey, A. J. Duncan, and W. Sibbett, "Single-pulse Fourier-transform spectrometer having no moving parts," Appl. Opt. **33**, 6035–6040 (1994).
6. B. A. Patterson, M. Antoni, J. Courtial, A. J. Duncan, W. Sibbett, and M. J. Padgett, "An ultra-compact static Fourier-transform spectrometer based on a single birefrigent component," Opt. Commun. **130**, 1–6 (1996).
7. J. Courtial, B. A. Patterson, A. R. Harvey, W. Sibbett, and M. J. Padgett, "Design of a static Fourier-transform spectrometer with increased field of view," Appl. Opt. **35**, 6698–6702 (1996).
8. T. Inoue, A. Hirai, K. Itoh, and Y. Ichioka, "Compact spectral imaging system using liquid crystal for fast measurement," Opt. Rev. **1**, 129–131 (1994).
9. B. H. Billings, "Visual Fourier-transform spectroscopy with single crystal plate," J. Opt. Soc. Am. **65**, 817–824 (1975).
10. P. Yeh and C. Gu, *Optics of Liquid Crystal Displays* (Wiley Interscience, New York, 1999).
11. M. Born, and E. Wolf, *Principles of Optics*, 6th ed. (Cambridge U. Press, New York, 1980).
12. I. C. Khoo and S. T. Wu, *Optics and Nonlinear Optics of Liquid Crystals* (World Scientific, Singapore, 1993).
13. Advanced Stray Light Analysis Program, B. R. Organization, Tucson, Ariz., 1999.
14. LCD Master, Shintech, Yamaguchi, Japan (1997).
15. F. Rinne and M. Berek, *Anleitung zur allgemeinen und Polarisationsmikroskopie der Festkörper im Durchlicht* (Schweizerbart'sche Verlagsbuchhandlung, Stuttgart, 1973).
16. A. F. Hallimond, *The Polarizing Microscope* (Vickers Instruments, York, UK, 1970).
17. A. R. Harvey, M. Begbie, and M. J. Padjett, "Stationary Fourier transform spectrometer for use as teaching tool," Am. J. Phys. **62**, 1033–1036 (1994).
18. J. Courtial, B. A. Patterson, W. Hirst, A. R. Harvey, A. J. Duncan, W. Sibbett, and M. J. Padgett, "Static Fourier-transform ultraviolet spectrometer for gas detection," Appl. Opt. **36**, 2813–2817 (1997).
19. F. J. Dunmore and L. M. Hanssen, "Miniature Fourier instrument for radiation thermometry," presented at the Fourier Transform Spectroscopy: 11th International Conference, Athens, Ga., 10–15 August 1997.
20. C. C. Montarou and T. K. Gaylord, "Analysis and design of modified Wollaston prisms," Appl. Opt. **38**, 6604–6613 (1999).

Annex 2

Mol. Cryst. Liq. Cryst., Vol. 375, pp. 301-311

1058-725X/02 $12.00 + .00

Polarization Ray Tracing in Twisted Liquid Crystal Systems

GERBEN BOER[a] and TORALF SCHARF[b]

[a]*CSEM Badenerstrasse 569 CH-8048 Zürich, Switzerland and*
[b]*IMT Breguet 2 CH-2000 Neuchâtel, Switzerland*

In this paper it will he presented different ray trace models that are able to simulate uniaxial birefringent optical elements with twisted structure. There exist already methods to calculate the optical behavior of birefringent elements (including angular dependence) such as the Jones matrix method [2]. But those methods are not based on ray tracing and cannot be linked together with other optical components such as lenses for example. The aim of this work is to enable ray trace simulations of optical systems containing complex birefringent elements and extended sources. The developed models are applied on problems that are related to twist liquid crystal Wollaston prism.

Keywords ray-trace; polarization; simulation; twist nematic; birefringence; interferometry.

INTRODUCTION

To model systems incorporating birefringent elements, a ray trace program must take into consideration the polarization of light. So, two polarization components should be propagated through the system according the different refractive indices of the birefringent media they will encounter. The simulation of birefringent components with

uniform orientation is relatively simple but it becomes complex for twisted structures. The calculations of the optical transmission of twisted nematic cells are usually done with Jones matrix methods or a 4x4 matrix method (Berreman). These methods calculate accurately the angle-dependent phase retardation of two polarization components for planar systems but they don't give the spatial or directional separation between rays caused for instance by refraction at interfaces between anisotropic and isotropic materials. In our case of polarization interferometry with extended sources, the localization of the plane of interference is important. One finds this plane of localization of interference fringes as the point of intersection of beams that were split before. Since we need to perform ray-tracing simulations, a conventional matrix method is not suitable for our purpose. To overcome these problems, we developed new methods based on polarization ray tracing that can simulate twisted structures and take the direction of beams into account. We choose as a basis for our work the ray-trace program ASAP (Advanced Systems Analysis Program) form BRO [3]. This commercial available program is able to simulate accurately polarization properties of anisotropic uniaxial crystals as well as other conventional optical elements. We will present two different models for twisted elements. The first one is based on multiple ray-splitting. In the second one, the twisted cell is modeled in a similar way as in the Jones matrix calculus by using combinations of retarder plates and polarization rotators.

RAY TRACE IN UNIAXIAL MEDIA

In this chapter, we will discuss the possibility to simulate simple uniaxial birefringent component by splitting an incoming ray into an ordinary and extraordinary ray.

Each ray is characterized by the usual trace information such as ray direction, optical phase shift, flux and a polarization vector. When such a ray encounters uniaxial media, it splits into an ordinary and extraordinary ray. Snell's law gives the direction of these new rays. The reflection and transmission coefficients are calculated with the Fresnel formulae [4]. If one examines the case of a boundary between an isotropic material (index n) and an anisotropic material (index n_o and n_e), which is illustrated in Figure 1, the refraction angle ϕ_o for the ordinary ray is given by:

$$n \sin\phi = n_o \sin\phi_o \qquad (1).$$

the refraction angle ϕ_e for the extraordinary ray is given by:

$$n \sin\phi = n_e(\phi_e) \sin\phi_e \qquad (2)$$

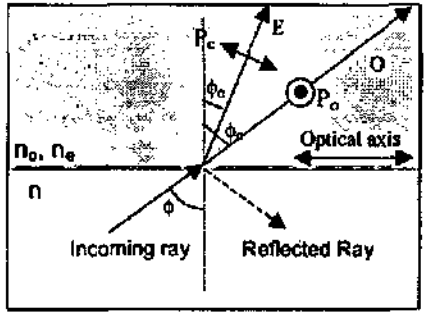

FIGURE. 1 Splitting at an isotropic anisotropic interface of an incoming ray into an ordinary (O) and extraordinary (E) ray.

The refractive index $n_e(\phi)$ depends on the angle of incidence ϕ and the orientation of the optical axis. The polarization vectors (P_o, P_e) attached to the ordinary and extraordinary rays are set perpendicular to the propagation direction. When passing through the crystal medium the ordinary ray will experience the refraction index n_o and the extraordinary ray will experience n_e. The two rays carry also their own optical path length and amplitude. The reflected part is not considered here and eventual multiple reflections are neglected.

ASAP uses this model for simulating simple uniaxial plates. In ASAP, each ray represents a Gaussian beam with a certain waist and divergence. An arbitrary field can be created by a judicious superposition of such Gaussian beams [7]. Those beams are then propagated by geometrical ray-trace methods [8]. Phase, amplitude and polarization state are changed accordingly to the birefringent components encountered by the rays. At the output (or at the detector), the different Gaussian beams can be added coherently (electric

amplitudes addition) or incoherently (square modulus of the electric field addition) with respect to each other.

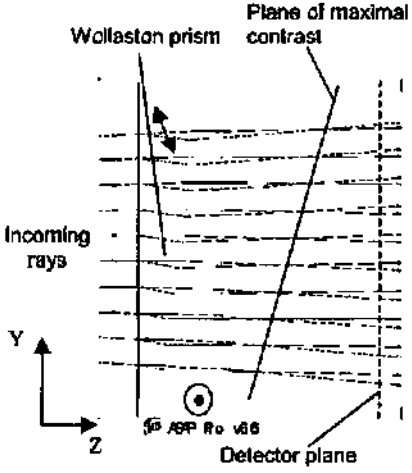

FIGURE 2 Ray tracing of a divergent source trough a Wollaston prism with tilted optical axis.

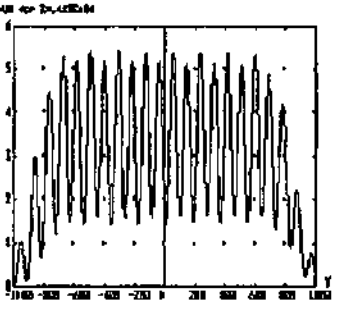

FIGURE 3 Interference pattern in the defocalised plane

Application to the Wollaston Prism

To show the performance of such ray trace method, we applied it to a polarization interferometer based on a Wollaston prism. As shown in Figure 2, a Wollaston prism consists of two wedges made of a birefringent material and joined by their hypotenuse. The optical axes are mutually perpendicular at the interface of the two wedges. If the Wollaston prism is placed between two linear polarizers at 45°, it becomes a polarization interferometer [5]. At the input of the Wollaston prism, the polarized light can be decomposed into two polarization components TE and TM. The TE component is parallel to the ordinary axis with index n_o and the TM component is parallel to the extraordinary axis with index n_e. In the second prism, the situation is inverted: TE and TM experience n_e and n_o respectively. By summing

the phase shift produced by each prism, the total phase difference δ between the two components at the output of the Wollaston becomes:

$$\delta = \frac{2\pi}{\lambda} 2y(n_e - n_o)\tan\theta, \qquad (3)$$

where y is the vertical coordinate, λ the wavelength and θ the wedge angle. The light passes then through a second polarizer, which transforms this phase shift into an interference pattern (output interferogram). The Fourier-Transform of this interference pattern gives the spectrum of incident light [5].

One interesting property of interferometry is the localization of the plane of interference if extended sources are used. Actually, when an interferometer is illuminated by a spatially incoherent source, the interference fringes are localized in space [4]. Depending on the interferometer configuration, the localization of the fringes (or plane of maximal contrast) may be difficult to find.

To calculate the position of the plane of maximal contrast of the above-described interferometer, we need to simulate the directional changes of the rays. The interferometer was simulated with a spatial incoherent source by defining a set of point sources. Figure 2 gives a schematic overview: the incoming rays are split at the first interface due to the tilted optical axis and traverse the system. Behind the Wollaston prism, at the intersection point of the ordinary and extraordinary ray, one finds the locus of the plane of maximal contrast. Figure 3 shows the obtained interferogram for a detector plane that is defocalized as indicated in Figure 2. Because the detector plane is not the plane of maximal contrast, the contrast of the interferogram is only about 70%.

TWISTED STRUCTURES

In this previous chapter we have shown the possibilities to simulate optical systems containing simple uniaxial plates. Twisted structures are also interesting because of their numerous applications in liquid crystal devices. Angle dependence is one of the major problems when simulating such structures. Models that can calculate the transmission of light through birefringent media are the Jones Matrix or the Berreman method [2]. We will show here two different methods that have been implemented in ASAP to simulate twisted nematic (TN) cells.

Multiple Ray Splitting Method

In this first method, we divided the TN cell into N thin plates with linear increasing azimuthal angle of the optical axis. Each plate can be considered as a homogenous uniaxial media and it can be modeled as in the previous chapter. So, at the interface of each plate, all the rays are split into an ordinary and extraordinary ray and than propagated further. Finally, we end-up with considerable number of rays equal to 2^N rays because each incoming ray is split at each interface.

We applied this model to a system similar to the Wollaston prisms placed in between 45° polarizers. The birefringent homogenous prisms are replaced by wedge shaped twisted nematic cells as shown in Figure 4. For normal incidence, this configuration has the same optical properties as the classical Wollaston prism but the angular dependence is different.

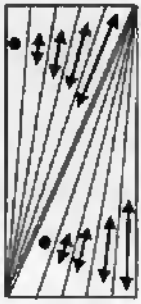

FIGURE 4 Wollaston prism made of two twisted nematic wedge cells.

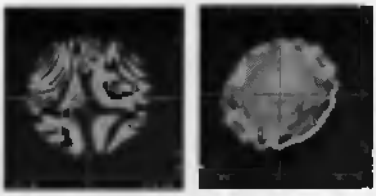

FIGURE 5 Interference pattern showing the field of view for (a) opposite twist sense configuration (b) equal twist configuration.

The angular dependence can be studied by focusing light (or rays) with high incidence angles into a point of interest. Since the number of rays needed to approximate accurately a converging wave front is proportional to the covered angle, we limit the incidence angles to the range of ±35°. The light is focused exactly in the center of the Wollaston prism (birefringence $\Delta n = 0.28$, wedge angle $\theta = 0.6°$ and thickness = 0.2 mm). We compare the field of view between two different configurations: the first configuration has two twisted nematic cells of opposite twist sense and the second configuration has

two twisted nematic cells with equal twist sense. The cells are divided into 7 slices each. Figure 5 (a) and (b) show the interference pattern in the far field for the configuration with opposite twist sense and equal twist sense respectively. In the angular range of $\pm 35°$ the simulations are in accordance with experimental results given elsewhere [1]. Unfortunately, this method is suffering from the high computational times. As already mentioned above, the successive splitting produces a very high number of rays. Consequently, we have to limit the number of slices. Of course, this affects the quality of the simulation because the model becomes more precise with increasing number of slices. By using Fresnel formulas, losses due to simple reflections are taken into account but multiple reflections are not. So, this method is not suited to simulate twisted cells with high incidence angles where multiple reflections become important.

One splitting Ray Method

In a second approach, we model the cell as a set of polarization rotators and retarder plates. As shown in Figure 6, the cell is divided into N thin uniaxial crystal plates where each of them is followed by a polarization rotator. The azimuth angle of the optical axis of each plate is rotated by a constant amount with respect to the optical axis of the previous plate. The polarization rotators ($R(\phi/N)$) rotates the polarization vector attached to each ray by the same amount.

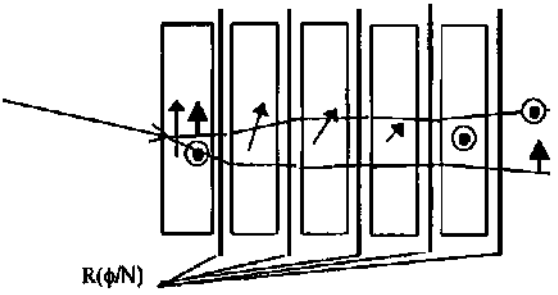

FIGURE 6 Ray tracing of an ordinary and extraordinary ray through a twisted nematic cell modeled with the one split algorithm.

At the first interface, the incoming rays are split into an ordinary and extraordinary ray. At the output of the first crystal plate the polarization vectors are rotated by ϕ/N with rotation matrices. At the entrance of the second plate, all rays are refracted. The polarization vector of the ordinary and extraordinary ray is projected parallel and perpendicular to the optical axis of the second plate. The same process is repeated for the following plates. Reflected light is not traced further, which causes problems for high angle of incidence. This algorithm doesn't takes multiple reflections into account but Fresnel [4] losses are considered. This ray trace algorithm is comparable to Jones matrix calculations because it divides the system into a set of retardation and rotation matrices [6]. However Jones matrix calculation does not takes the change of direction of the ordinary and extraordinary rays due to refraction into account.

In our model, the incoming rays are only split once at the first isotropic anisotropic interface. So, the number of rays at the output is reasonable and more complex simulations can be performed. In order to compare this new method with the previous one, we simulated the same configuration as shown in Figure 4. The system was illuminated with high angles of incidence up to ± 62°. Figures 7 (a) and (b) show the simulated field of view for configurations with opposite and equal twist sense respectively. Thanks to the reduced number of rays, the new method allows us to cover a much wider angular range (± 62°) than the simulations shown in Figure 5 (a) and (b). More accurate results for high incidence angles may be obtained with increasing number of layers per thickness.

For small angles of the liquid crystal wedge it is possible to regard the system as planar and one can simulate the angle dependence. Berreman matrix calculations with 100 layers are shown in Figure 7(c) and (d), which show a very large field of view for the configuration with equal twist sense. If one compares Figure 7 (a) and (b) with (c) and (d), the limitations of our model to small apertures becomes evident.

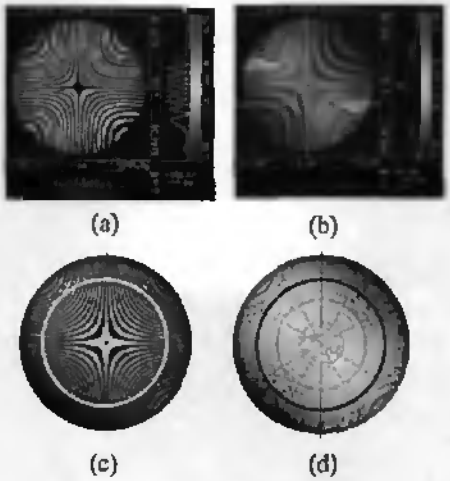

FIGURE. 7 Interference pattern showing the field of view: (a) opposite twist sense configuration, (b) equal twist sense configuration with 10 layers per cell, (c) Berreman calculation (100 layers) for the opposite twist,(d) Berreman calculation for the equal sense configuration. The white and black circles delimit the incidence angle within 60°.

In that what follows, we apply this method to find the plane of maximal contrast for the twisted configuration as we did before for the classical Wollaston prism (Figures 2 and 3). In this configuration, the plane of maximal contrast is located inside the Wollaston prism. For this reason, we used an additional lens in order to image the plane of maximal contrast on a detector plane. Figure 8(a) shows the ray tracing through the system. The extended source is simulated with the help of multiple monochromatic point sources (tree in Figure 8(a)), which are mutually incoherent.

The twisted cells that constitute the Wollaston prism are modeled as described in Figure 6. An ideal lens without aberrations images the interference pattern on the detector with a magnification of –1. We limit here the incidence angle to ± 4.5° so that internal reflections can be neglected. Figure 8(b) shows the obtained interferogram at the detector plane.

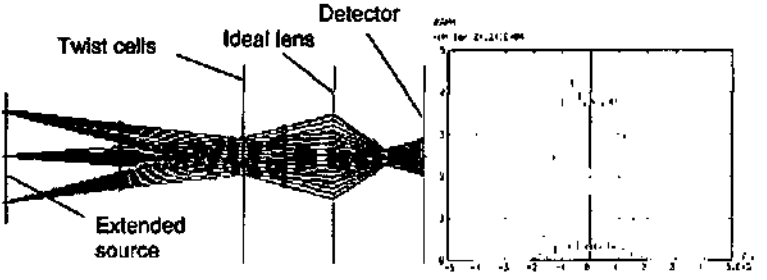

FIGURE 8 (a) Ray tracing with ASAP through a complete optical system. (b) Simulated interferogram at the detector plane.

CONCLUSION

We presented several methods able to simulate systems containing birefringent uniaxial materials and in particular twisted structures. Those methods are implemented in an optical ray trace program (ASAP), which enables us to simulate birefringent elements of almost any shape in combination with other optical elements, like lenses, mirrors or complete illumination systems. However, these methods are only suited for problems involving relatively thick twisted elements with small twist angles and limited incidence angles. The exact limitations of the presented methods have not yet been found.

REFERENCE

[1] G. Boer, T.Scharf, R.Dändliker, , submitted to Applied Optics.
[2] P. Yeh, and C. Gu, Optics of Liquid Crystal Displays (Wiley Interscience, New York, 1999).

[3] Breault Research Organization, "Polarization", (ASAP application notes, Tuscon, 1999)
[4] M. Born, and E. Wolf, Principles of Optics, sixth ed. (Cambridge university press,1980).
[5] M. J. Padgett, A. R. Harvey, A. J. Duncan, and W. Sibbett, Applied Optics 33 (25), 6035-6040 (1994).
[6] B. E. A.Saleh, M. C. Teich, Fundamentals of Photonics, (John Wiley, 1991). p.229.
[7] Breault Research Organization, "Wave optics", (ASAP application notes, Tuscon, 2001).
[8] J.Arnaud, Applied Optics 24 (4), 538-543 (1985).